Lehrstuhl für Kommunikationstechnik
Hochschule Harz (FH)

No. 10, 2011

U.H.P. Fischer-Hirchert (Hrsg.)

ITG INFORMATIONSTECHNISCHE
GESELLSCHAFT IM VDE

IX. ITG-Workshop

Fachgruppe 5.3.2

Photonische Komponenten und Mikrosysteme

ITG
Photonische Komponenten
und Mikrosysteme

11. Mai 2011

Universität Erlangen-Nürnberg
Lehrstuhl FAPS
Forum im Park
Nordostpark 89,
90411 Nürnberg, Germany

VDE

Cuvillier Verlag Göttingen

ITG INFORMATIONSTECHNISCHE GESELLSCHAFT IM VDE

IX. ITG-Workshop

Fachgruppe 5.3.2

Photonische Komponenten und Mikrosysteme

ITG
Photonische Komponenten
und Mikrosysteme

11. Mai 2011

Universität Erlangen-Nürnberg
Lehrstuhl FAPS
Forum im Park
Nordostpark 89,
90411 Nürnberg, Germany

VDE

Bibliografische Information der Deutschen Nationalbibliothek
Die Deutsche Nationalbibliothek verzeichnet diese Publikation in der
Deutschen Nationalbibliografie; detaillierte bibliografische Daten
sind im Internet über http://dnb.d-nb.de abrufbar.
1. Aufl. - Göttingen : Cuvillier, 2011

978-3-86955-733-5

Nonnenstieg 8, 37075 Göttingen
Telefon: 0551-54724-0
Telefax: 0551-54724-21
www.cuvillier.de

1. Auflage, 2011
Gedruckt auf säurefreiem Papier

978-3-86955-733-5

Einladung zum ITG-Workshop "Silicon Photonics" in Nürnberg

Die Informationstechnische Gesellschaft im VDE, vertreten durch die ITG-Fachgruppe 5.3.2 „Photonische Komponenten und Mikrosysteme“ und die Hochschule Harz in Wernigerode, werden am **11. Mai 2011 von 10:00 bis 17:00** einen Workshop ausrichten, zu dem wir interessierte Experten aus Wissenschaft und Industrie herzlich einladen. International angesehene key note speaker werden über zukünftige Trends und Entwicklungen im Bereich der photonischen Komponenten und Aufbautechnik für Silicon Photonics berichten.

Themen:

- Silicon Photonics
- Photonic Lightwave Circuits
- zukünftige Applikationen der Silicon Photonics (Prozessoren, Speicher, etc)
- Aktive nanokristalline Strukturen auf Si-Basis
- Integration von integrierten Wellenleitern mit aktiver Optoelektronik
- Entwicklung spezieller industrieller Herstellungsverfahren für Photonische ICs
- Faser-Chip-Kopplung nanostrukturierter Bauteile
- Modultechnologien: Optimierung des kompletten Modulaufbaus (Langzeitstabilität, Kosten, Integration elektrische und optische Schnittstellen)

Hintergrund

Die optische Nachrichtentechnik ist die Basis moderner Kommunikationssysteme, welche zu einem der wichtigsten Grundpfeiler der modernen Gesellschaft geworden sind. Schlüsselkomponenten sind neben der Faser sowohl die optischen wie auch die optoelektronischen Komponenten, d.h. die photonischen Komponenten. Photonische Komponenten sind Schlüsselelemente optischer Technologien und die Basis neuer Produkte. Für unterschiedlichste Anwendungen ist eine Vielzahl photonischer Komponenten verschiedenster optischer und optoelektronischer Funktionalität erforderlich. Das technologische Niveau einer Vielzahl von Produkten wird von ihnen erheblich mitbestimmt und ist sogar von ihnen abhängig. Von wenigen Globalplayern abgesehen, wird der Markt optischer Komponenten durch hochspezialisierte KMUs bestimmt. Die Herstellung optischer, faseroptischer und optoelektronischer Komponenten und Bauelemente sichert den Fortschritt von wissenschaftlichen Instituten und der photonischen Industrie.

Die Maximierung der Integrationsdichte in zukünftigen Systemkomponenten durch monolithische und hybride Integrationstechniken ist ein wichtiger Aspekt, der bei der Entwicklung neuer Techniken für die Photonische Aufbau und Verbindungstechnik dieser Komponenten zu berücksichtigen ist. Die ITG-Fachgruppe "Photonische Komponenten und Mikrosysteme" widmet sich der Diskussion dieser und weiterer Problemstellungen im Fokus des Bereichs der optischen Nachrichtentechnik.

Themen und Zielstellung

Im Kontext der rasanten Entwicklung photonischer Technologien sind die Aktivitäten der Fachgruppe auf die Anwendungsbereiche Telekommunikation, Datacom und Automotive ausgerichtet.

Ziel der Fachgruppe ist es, eine nationale Plattform zur Diskussion oben genannter Themen zu bilden und darüber hinaus den Know-How-Aufbau und den Wissenstransfer durch Austausch und Auswertung von Erfahrungen und Informationen aktiv zu begleiten. Dazu gehören die Durchführung und Förderung nationaler und internationaler Diskussionsforen, Durchführung und Förderung nationaler und internationaler Tagungen, Erarbeitung von Richtlinien und Empfehlungen und auch die Initiierung von und Mitarbeit bei nationalen und internationalen Forschungs- und Entwicklungsprojekten im Bereich photonischer Komponenten und Mikrosysteme.

Organisation und lokale Ausrichtung :

Friedrich-Alexander-Universität
Erlangen-Nürnberg

Lehrstuhl für Fertigungsautomatisierung
und Produktionssystematik (FAPS)
Friedrich-Alexander-Universität Erlangen-Nürnberg
Prof. Dr.-Ing. Jörg Franke
Nordostpark 91, 90411 Nürnberg

Ansprechpartner:
Dipl.-Ing. Daniel Craiovan
Fon: +49 911 5805816
Fax: +49 911 5805830
daniel.craiovan@faps.uni-erlangen.de

Mitglieder der Fachgruppe 5.3.2:

Prof. Dr. Manfred Berroth, Universität Stuttgart

Dipl.-Ing. Daniel Craiovan, Universität Erlangen

Prof. Dr. Ulrich Fischer-Hirchert,
Harz University of Applied Sciences, Wernigerode

Dipl.-Ing. M. Franke, Siemens AG, Berlin

Dr. Norbert Grote, Fraunhofer HHI Berlin

Dipl.-Ing. Lutz Melchior OptriCon GmbH, Berlin

Richard Pitwon
XyrATEX Ltd., Havant, United Kingdom

Dr. Marc Schneider, FZ Karlsruhe, Karlsruhe

Dr. Henning Schröder, Fraunhofer-Institut IZM, Berlin

Dr. Klaus Schulz, Sodaja Consulting, Berlin

Dr. Krzysztof Nieweglowski, TU Dresden

Dipl.-Phys. Andreas Umbach, u2t Photonics GmbH Berlin

Tagungsprogramm IX. Workshop
„Silicon Photonics“
Nürnberg

Mittwoch, 11. Mai 2011

Ab 09:00 Registrierung

09:50 Begrüßung durch Leiter des FAPS der Universität Erlangen-Nürnberg
Prof. Franke und den Chairman der ITG Gruppe 5.3.2 Prof. Fischer-Hirchert

Session 1: "Integrated Photonic Devices/Components"

Chairman: Andreas Umbach

10:00 Invited Talk*: „Silicon Photonic Devices for Advanced Modulation Formats“*
Manfred Berroth, W. Vogel, W. Sfar Zaoui, T. Föhn, S. Klinger
Universität Stuttgart

10:40 *"Nonlinear Optical Property Measurement in Integrated Photonic Devices“*
Erik Benkler, Anatoly Sherman, and Harald R. Telle, PTB Braunschweig

11:05 „Design and Simulation of Optical Interfaces for Photonic Integrated System-in-Package“
Gili de Villasante, O.a; Wang, Z.a; Suna, A.b; Tcheg, P.a; Wang, B.b; Lutzmann. S.a; Baumann, C.a; Kesmis, Y.a; Sakalas, M. a; Dondjio, B.b; Ngo, H.-D. a; and Tekin, T., TU Berlin

11:30 – 12:00 Kaffeepause (Foyer)

12:00 *"Optical Coupling of SOI Waveguides and INP based Photodetectors“*
Ludwig Mörl, Wolfgang Passenberg, Margit Ferstl, Detlef Schmidt
Timo Aalto, Mikko Harjanne, Markku Kapulainen, Sami Ylinen
Dries Van Thourhout, Peter De Heyn, Fraunhofer HHI Berlin

12:25 *" Silicon photonic micro-cavities, Raman-amplifiers, and ultra-small electro-optic modulators „*
Stefan Meister; Al-Saadi, Aws; Franke, A., Bülent; Mahdi, Shaimaa; Kupijai, Sebastian; Woggon, Ulrike; Zimmermann, Lars; Hui, Tian; Richter, H., Harald; Stolarek, David and Eichler, J., Hans; TU Berlin

12:50 *„Reconfigurable Spectral Phase Encoder in a Silicon Photonics Platform”*
Jamshidi Kambiz; Meister, Stefan; Al-Saadi, Aws; and Schneider, Thomas, Deutsche Telekom Hochschule Leipzig

13:15 – 14:15 Mittagspause

Session 2: " Fabrication of Si-Photonics "

Chairman: Daniel Craiovan

14:15 Invited Talk*: „Foundry-Prozesse für die Siliziumphotonik“*
Lars Zimmermann, TU Berlin

14:50 *„CMOS-Compatible Fabrication of Integrated Silicon Photonic Systems“*
M. Karl.; Wahlbrink, T.; Bolten, J.; Prinzen, A.; Manecke, C.; Kleinjans, H.; Porschatis, C.; Lerch, H.; Waldow, M.; Merget, F.; Baus, M.; Kurz, H.
AMO GmbH, Aachen

15:15 *„Tunable Finite Impulse Response Filter for Dispersion Compensation using Multi-Arm MZIs in SOI Technology“*
S. Schwarz, A. Rahim, J. Bruns, C. G. Schäffer, and K. Petermann,
Helmut Schmidt Universität Hamburg

15:40- 16:00 Kaffeepause (Foyer)

16:00 *„Integration of novel lattice-matched Ga(NAsP) laser material on (001) Si for optoelectronic and photonic applications”*
Bernardette Kunert, Kerstin Volz, Wolfgang Stolz, NAsP III/V GmbH Marburg

16:25 *„Silicon photonic components for a novel interferometric biosensor array concept“*
P. Muellner; Bruck, R.; Hainberger, R.; Karl M.; Baus, M.; and Wahlbrink, T,
Austrian Institute of Technology GmbH, Vienna, Austria

16:50 „*Integrated Bragg Gratings on SOI RibWaveguides for Dispersion Compensation*
Ivano Giuntoni; Gajda, Andrzej; Krause, Michael; Stolarek, David; Steingrüber, Ralf; Bruns, Jürgen; Zimmermann, Lars; Brinkmeyer, Ernst; Tillack, Bernd and Petermann, Klaus , TU Berlin

17:15 Abschlussworte und Ende des Workshops
Andreas Umbach Chairman ITG Fachgruppe 5.3.2

anschließend Möglichkeit zur Laborbesichtigung

Inhaltsverzeichnis

Invited Talk: *„Silicon Photonic Devices for Advanced Modulation Formats“*

Manfred Berroth, W. Vogel, W. Sfar Zaoui, T. Föhn, S. Klinger
Universität Stuttgart

Nonlinear Optical Property Measurement in Integrated Photonic Devices

Erik Benkler, Anatoly Sherman, and Harald R. Telle

Abstract — We discuss and demonstrate a novel technique for the measurement of nonlinear optical parameters related to the complex third-order susceptibility $\chi^{(3)}$, such as nonlinear refractive index, two-photon absorption coefficient, and nonlinear figure of merit. The method is ideally suited for the spatially resolved measurement of such properties along a waveguide path ("photonic bus") inside integrated photonic devices.

Index Terms — integrated photonic devices, measurement techniques, nonlinear optics

1. *INTRODUCTION*

NONLINEAR effects provide the foundation for the implementation of any direct opto-optical function in integrated photonic devices [1]. Several functional building blocks like all-optical switches or modulators based on nonlinear interactions between two or more independent optical fields can be integrated into a photonic chip. These units are interconnected by waveguides, either intra-chip or inter-chip, and even over very long distances via optical fibers. Hence, on the one hand, nonlinear effects are desired in the functional units. On the other hand they are usually unwanted in the waveguides used for interconnection. As an example channel crosstalk due to four wave mixing is an unwanted effect for WDM transmission.

Novel nonlinearity measurement techniques are required for the characterization of integrated photonic devices, with the following demands: First, the technique must be applicable to waveguides which transmit a single transverse mode. This excludes standard techniques like z-scan [2] relying on transversal effects. Second, it should provide spatial resolution better than a few ten µm along the photonic bus. Third, the method must be highly sensitive in view of the short interaction lengths required for the spatial resolution mentioned above. Here, we discuss a novel technique which fulfills these requirements.

This paper is organized as follows: First, the basic technique employed for the nonlinearity measurement is described where emphasis is put on referencing the nonlinear parameters of the waveguide under test to well-known optical properties of a bulk sample. Its outstanding sensitivity is demonstrated using a sample with extremely small nonlinearity. Then, the method is extended to complex quantities, i. e. to the simultaneous measurement of the real and imaginary components of the third-order susceptibility $\chi^{(3)}$, yielding a direct measurement of the nonlinear figure of merit which plays an important role for all opto-optical functions. Finally, an outlook is given how a modification of the method can provide the required spatial resolution along the photonic bus.

2. *MEASUREMENT PRINCIPLE*

For the measurement of $\chi^{(3)}$ nonlinearities in integrated photonic devices a $\chi^{(3)}$ effect compatible with their waveguide geometry must be used. For this reason, we employ collinear nearly degenerate four wave mixing, which was sometimes termed three wave mixing in the literature [3]. In a special case of this process, mixing fields E_{m1} and E_{m2} at new frequencies $\nu_{\mathrm{m1}} = 2\nu_1 - \nu_2$ and $\nu_{\mathrm{m2}} = 2\nu_2 - \nu_1$ are generated from two excitation fields E_1 and E_2 with optical frequencies ν_1 and ν_2 (see inset of Fig. 1) The mixing fields carry the information on both the real and imaginary parts of $\chi^{(3)}$:

$$E_{\mathrm{m1}} \propto \chi^{(3)} E_1^* E_1 E_2 \tag{1}$$

The mixing field can be heterodyne detected, which has two major benefits:

1. It enables, in principle, shot noise limited detection sensitivity due to heterodyne gain
2. The mixing field is detected, i.e. its phase and its amplitude, ultimately allowing the measurement of both real and imaginary part of $\chi^{(3)}$.

Fig. 1 schematically shows the experimental setup. A modelocked Er-fiber laser with central wavelength of λ = 1580 nm, a pulse length of τ = 100 fs, a repetition rate f_{rep} = 56 MHz, and average power of 10 mW is used as light source.

Manuscript received March 31, 2011. This work was supported in part by the German Research Foundation DFG within the framework of Collaborative Research Center SFB407.

E. Benkler (e-mail: Erik.Benkler@ptb.de) and H.R. Telle are with the Physikalisch-Technische Bundesanstalt (PTB), Bundesallee 100, D-38116 Braunschweig. A. Sherman is with the aleo solar AG, Osterstrasse 15, D-26122 Oldenburg.

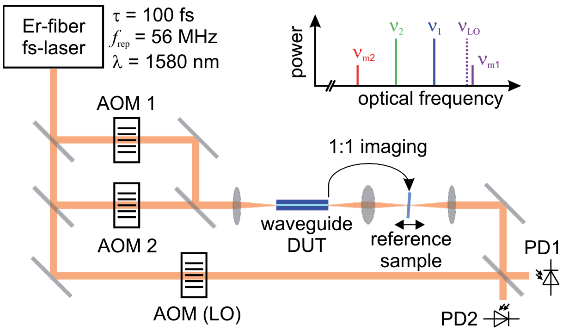

Figure 1: Experimental setup. See text for details. The inset shows a stick frequency diagram for illustration of the heterodyne detection of nearly degenerate four wave mixing signals.

The modelocked laser generates an optical frequency comb, i.e. its spectrum consists of sharp equidistant lines. In the strict sense this fact should be taken into account in the explanation of the four wave mixing process. However, it turns out that this does not lead to substantially different results than just considering cw fields instead, as long as the pulse peak power remains approximately constant during propagation inside the device under test (negligible losses and dispersion effects). Hence for simplicity, the discussion throughout this paper is restricted to one comb tooth.

The laser output is split up into three arms and the optical frequencies in each arm are shifted by means of acousto-optical modulators (AOMs).

In the first two arms, the four-wave mixing excitation fields E_1 and E_2 are generated and subsequently overlapped in space and time at a beam combiner. The excitation fields are thus co-propagating and can hence be coupled into the waveguiding device under test (DUT). In the DUT, the fields E_{m1} and E_{m2} are generated by collinear nearly degenerate four wave mixing. In principle, the detection of one of these fields would be enough to gain the desired information on the third-order susceptibility.

However, the mixing field critically depends on the peak power and other excitation pulse parameters which might even fluctuate during a measurement. For this reason, we introduced a novel method which is based on referencing the mixing field to the mixing field generated by the same excitation pulses and under equal experimental circumstances in an additional reference sample [4]. For this purpose, the output facet of the waveguide DUT is imaged 1:1 to an imaging plane by means of two parabolic mirrors (shown as a single lens in Fig. 1). A thin bulk reference sample with well known optical properties is introduced in the vicinity of the beam waist at the imaging plane. The overall mixing field thus consists of the sum of the mixing fields generated in the waveguide DUT and in the reference sample. Due to the 1:1 imaging, the mode field diameter (MFD) at the beam waist is identical with the MFD in the waveguide. Hence, if the reference sample is located in the beam waist, the two complex valued contributions to the detected mixing product add-up, whereas contributions from the reference sample can be neglected if the reference is far from the beam waist since the MFD is much larger than at the output facet of the DUT. The reference sample can be continuously moved into and out of the beam waist, with a minimum of disturbances, e.g. due to beam geometry changes. Using this principle, the nonlinear parameters of the DUT can be referenced to the parameters of the well-characterized reference sample, in particular without any knowledge of the exact pulse parameters or mode field diameters.

One of the generated mixing fields is then heterodyne detected. For this purpose, the mixing field is spatio-temporally superimposed with an auxiliary “local oscillator” field E_{LO} generated by frequency shifting the optical frequency in the third arm to ν_{LO} (see stick diagram in the inset of Fig. 1). The resulting beat photocurrent at the frequency $\nu_{\mathrm{beat}} = \nu_{\mathrm{m1}} - \nu_{\mathrm{LO}}$ is then detected with photodiode PD1:

$$i_{\mathrm{beat}} \propto E_{\mathrm{m1}} E_{LO}^{*} + \mathrm{c.c.} \qquad (2)$$

Detecting both quadratures, or in other words both amplitude and phase, of the beat photocurrent allows the determination of both the real and the imaginary part of the third-order susceptibility $\chi^{(3)}$. The two quadratures are detected with a two-phase lock-in amplifier. For the lock-in detection an electrical reference signal at the beat frequency ν_{beat} is required. Its amplitude should be constant and its phase must have a strict relation to the phases of the excitation and LO fields. Ideally, it should be independent of any length fluctuations of either arm of the nested Mach-Zehnder interferometers. This can be achieved by detecting the two beat-notes $E_1 E_2$ and $E_{\mathrm{LO}} E_1$ with the help of PD2. The corresponding RF beat frequencies are $\nu_{\mathrm{b1}} = \nu_1 - \nu_2$ and $\nu_{\mathrm{b2}} = \nu_{\mathrm{LO}} - \nu_1$. These RF beat signals are individually phase-tracked by two separate phase locked loops (PLLs). Subsequently, the PLL output signals are mixed using a double-balanced mixer, yielding the desired reference signal at $\nu_{\mathrm{ref}} = \nu_{\mathrm{b1}} - \nu_{\mathrm{b2}} = \nu_{\mathrm{beat}}$. This scheme common-mode rejects perturbations due to arm length fluctuations in the interferometers to a high degree without the need for any active stabilization.

3. *DEMONSTRATION OF SENSITIVITY*

In this section, we use a sample with purely real $\chi^{(3)}$, i.e. negligible two-photon absorption for a demonstration of the extreme sensitivity of the described heterodyne detection technique. A purely real $\chi^{(3)}$ is well approximated in fused silica based DUTs. In this case, the amplitude of the beat photocurrent is proportional to Re($\chi^{(3)}$). As a waveguide DUT, we use a 2.1 cm short piece of NKT photonics HC-1550-01 hollow-core photonic crystal fiber (HC-PCF). In HC-PCFs the huge majority of light is confined to the hollow, air-filled core based on the photonic bandgap resulting from the photonic crystal cladding structure around the core. Owing to the very small light - fused silica overlap, these fibers have an effective nonlinearity which is about 3 orders of magnitude smaller than in standard solid core fibers. To appreciate the high sensitivity of the method, it is demonstrative that usual fiber nonlinearity measurements require kilometers long fibers instead of the few cm of HC-PCF investigated here. As a reference sample a 25 µm thin fused silica plate is employed. Its thickness is much smaller than the confocal parameter (180 µm) of the beam.

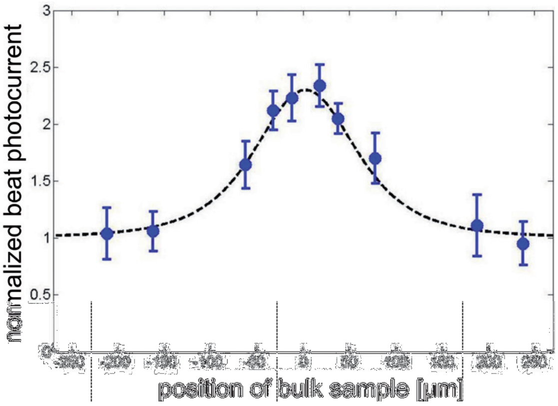

Figure 2: Beat photocurrent amplitude $\left|i_{\text{beat}}\right|$ as the reference sample is moved through the imaging plane, normalized to the beat photocurrent resulting from the HC-PCF alone. Blue circles: Experiment, dashed line: Calculation with a Gaussian beam.

Fig. 2 shows the result of a measurement in which the reference sample was shifted through the beam waist at the imaging plane. Please notice that although a sample is scanned through a focused beam, the method relies on a completely different principle than the z-scan technique. The dashed theoretical curve is computed for the 25 µm thin fused silica assuming a Gaussian beam with a confocal parameter of 180 µm, corresponding to the 13 µm MFD of the HC-PCF. From the normalized value at maximum (reference in focus), the value for the effective nonlinear refractive index of the HC-PCF is derived to be $n_2^{\text{HC-PCF}} = (5.7 \pm 3.2) \times 10^{-4} n_2^{\text{fused silica}}$, taking into account the (measured) attenuation of the excitation fields between the DUT and reference sample. In absolute terms, the cross-phase-modulation amplitude in the HC-PCF was about 10^{-5} rad.

This experiment demonstrates the potential of the technique for nonlinearity measurements in short waveguide DUT, such as integrated photonic devices.

4. COMPLEX $\chi^{(3)}$ MEASUREMENT

As described in section 2, the technique provides information on both real and imaginary part of $\chi^{(3)}$. The real part as measured with our technique is related to the nonlinear refractive index (using SI units):

$$n_2 = \frac{3}{2\varepsilon_0 n_0^2 c} \operatorname{Re}\left\{\chi^{(3)}\right\}, \tag{3}$$

and the imaginary part is related to the two-photon absorption coefficient:

$$\beta = \frac{3\pi}{\varepsilon_0 n_0^2 c\lambda} \operatorname{Im}\left\{\chi^{(3)}\right\}. \tag{4}$$

For opto-optical functions like all-optical switches, it is beneficial to have a large nonlinear refractive index and small linear and nonlinear absorption. For this reason, a nonlinear figure of merit can be defined as [5]

$$NFOM = \frac{n_2}{\lambda\beta} = \frac{\operatorname{Re}\left\{\chi^{(3)}\right\}}{2\pi \operatorname{Im}\left\{\chi^{(3)}\right\}}. \tag{5}$$

A value of $NFOM > 1$ is widely used as criterion for the suitability of a material for all-optical switching devices. Our technique directly measures the complex value of $\chi^{(3)}$. Hence, the $NFOM$ is also directly determined with real and imaginary part of $\chi^{(3)}$ measured coequally. Usually, this is not the case, since different measurement or analysis techniques are used for the nonlinear refractive index and for the two-photon absorption coefficient.

For a demonstration, we measured the complex value of $\chi^{(3)}$ of a crystalline <100> oriented silicon plate with a thickness of 41.5 µm. In this experiment, the roles of the waveguide and bulk sample have been exchanged, i.e., a standard single mode fiber (SMF28) with a length of 13.5 mm was used as waveguide sample acting as reference, and the bulk silicon plate as DUT was scanned through the imaging plane. We measured both quadratures of the beat photocurrent with a lock-in amplifier as described in section 2, for two cases:

1. The Si bulk sample is positioned far out of focus, i.e. the detected signal consists of the contribution from the SMF28 fiber alone.
2. The Si bulk sample is positioned in the imaging plane, i.e. the detected signal consists of the contributions from both samples.

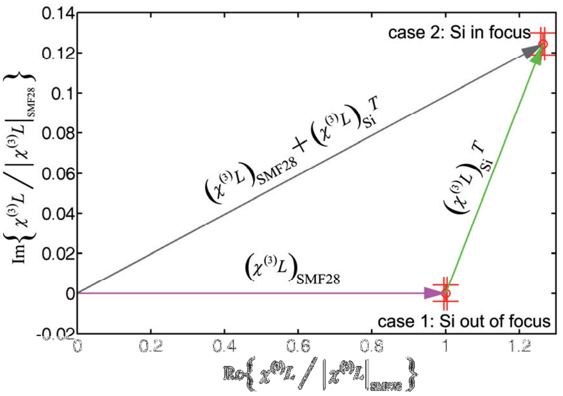

Figure 3: Normalized complex measurement data plotted in the complex plane. Magenta vector: Case 1 (Si plate out of focus, purely real contribution from SMF28 only), gray vector: Case 2 (Si plate in focus, contributions from both samples), green vector: Contribution of the Si plate. T is the transmission through the 1:1 imaging system.

For the analysis, we plot the measured quadratures as vectorial components into a Cartesian coordinate system. Since the SMF28 fiber has negligible two-photon absorption at telecom wavelengths, we can rotate this coordinate system such that the measurement point for case 1 (bulk sample out of focus) is on the abscissa. It can be shown [6] that the abscissa then describes the real part, and the ordinate describes the imaginary part of $\chi^{(3)}L$, where L is the sample length. We normalize the data to $\left|\chi^{(3)}L\right|_{\mathrm{SMF28}}$ as shown in Fig. 3.

From this plot, the $NFOM_{\mathrm{Si}}$ of silicon can be directly derived, even without knowledge of the Si plate thickness: It is simply given by the abscissa divided by the ordinate of the green vector in Fig. 3, divided by 2π. We find $NFOM_{\mathrm{Si}} = 0.34$, which is in good accordance with literature values. Given the lengths of the samples, we determine a nonlinear refractive index of $n_2^{\mathrm{Si}} = 3.4\times10^{-18}\ \mathrm{m^2/W}$ and a two-photon absorption coefficient of $\beta_{\mathrm{Si}} = 6.1\times10^{-12}\ \mathrm{m/W}$.

5. *Outlook: Spatially Resolved Technique*

With the described technique of co-propagating excitation pulses, the four wave mixing signal is generated continuously at all positions along the waveguide. In chapter 3 we demonstrated the high sensitivity of the technique, which allows to measure third-order nonlinearities of fused silica samples as short as a few micrometers. This means that the sensitivity of the method is compatible with a spatial resolution of a few micrometers along the propagation direction. However, to achieve such a resolution, the method must be modified.

The basic idea is to send two excitation pulses with frequencies ν_1 and ν_2 through a DUT's waveguide path from opposite directions as illustrated in Fig. 4.

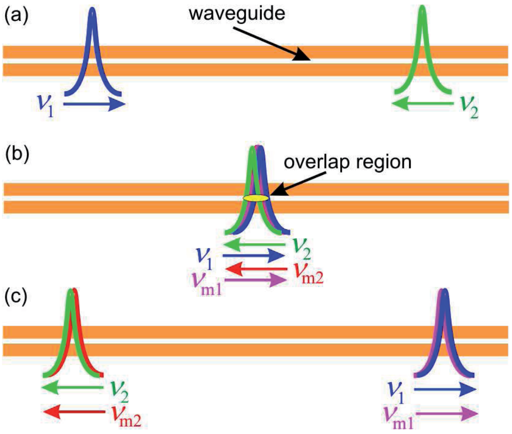

Figure 3: Basic principle of the spatially resolved technique. Excitation pulses (see stick diagram in the inset of Fig. 1 for the involved frequencies) are sent into a waveguide path from opposite ends. (a) Situation before the pulses encounter each other: No nonlinear interaction. (b) Whilst the counter-propagating excitation pulses overlap, counter-propagating four wave mixing pulses are generated. The overlap region is defined by the length of the pulses. (c) After the nonlinear interaction, the four wave mixing pulses can be heterodyne detected. See text for more details.

The pulses travel through the waveguide, and before they encounter each other, they cannot interact (Fig. 4(a)). However, at a position along the waveguide path, which is well-defined and controllable by the relative timing of their entrance into the device and by their group velocities, the excitation pulses overlap (Fig. 4(b)). The length of the overlap region is defined by the length of the pulses. For 100 fs short pulses, this length is of the order of a few ten micrometers. Whilst the pulses overlap, they interact through a four wave mixing process. As a result, counter-propagating mixing pulses are generated. After the overlap (Fig. 4(c)), they co-propagate with one of the excitation fields, respectively, and can thus be heterodyne detected as described in the previous sections. This approach is limited by several factors: In presence of chromatic dispersion, the pulses are stretched before the interaction as they travel through the waveguide. This limits the spatial resolution. Furthermore, the referencing to a bulk sample method relies on the assumption that the MFD in the waveguide device is constant along the path. This fact can, however, be exploited as well: If the MFD changes along the waveguide, as e.g. in an integrated photonic circuit, or at a splice between fibers with different core diameters, this position can be measured with high spatial resolution.

As mentioned before, the sensitivity of the measurement technique is high enough to measure four wave mixing fields generated in interaction regions as short as a few micrometers, i.e. shorter than the overlap region of 100 fs short pulses. Another benefit of the approach to couple the excitation fields in from two sides is that in this way, a certain waveguide path can be addressed amongst a manifold in integrated photonic circuits.

6. CONCLUSION

A sensitive method for the measurement of the complex-valued third-order susceptibility $\chi^{(3)}$ has been demonstrated. It was shown that the nonlinear properties of a sample with waveguide geometry can be referenced to the well-known optical properties of a bulk reference sample. Due to the extreme sensitivity resulting mainly from the employed heterodyne detection scheme, the method is applicable to integrated photonic and other short devices. Furthermore, a method based on the principle of counter-propagating excitation fields has been discussed in the outlook, which has a promising potential for nonlinear property measurements with spatial resolution along waveguide paths in integrated devices.

REFERENCES

[1] J. Leuthold, C. Koos, and W. Freude, “Nonlinear Silicon Photonics,” Nature Photonics 4, 535 (2010).

[2] M. Sheik-Bahae, A.A. Said, and E.W. Van Stryland “High-sensitivity, single-beam n_2 measurements”, Opt. Lett. 14, 955 (1989).

[3] K.O. Hill, D.C. Johnson, B.S. Kawasaki, and R.I. MacDonald, “cw three wave mixing in single mode optical fibers,” J. Appl. Phys. 49, 5098 (1978).

[4] A. Sherman, E. Benkler, and H.R. Telle, "Small third-order optical-nonlinearity detection free of laser parameters," Opt. Lett. 34, 49-51 (2009).

[5] H.C. Nguyen, K. Finsterbusch, D.J. Moss and B.J. Eggleton, “Dispersion in nonlinear figure of merit of As_2Se_3 chalcogenide fibre,” Electron. Lett. 42, 571 – 572 (2006).

[6] A. Sherman, E. Benkler, and H.R. Telle, “A sensitive method for measurements of complex third-order susceptibilities in waveguides,” Appl. Phys. B 98, 653-657 (2010).

Design and Simulation of Optical Interfaces for Photonic Integrated System-in-Package

Gili de Villasante, O.[a]; Wang, Z.[a]; Suna, A.[b]; Tcheg, P.[a]; Wang, B.[b]; Lutzmann. S.[a]; Baumann, C.[a]; Kesmis, Y.[a]; Sakalas, M. [a]; Dondjio, B.[b]; Ngo, H.-D. [a]; and Tekin, T. [a]

Abstract—*Optical interfaces for the integration of the System-in-Package technology in a Silicon Photonics platform are presented. Nano optical waveguides are used to avoid the problems that electrical interconnects have. The direct butt coupling between these optical waveguides and commercial single mode fibers present high mode mismatch losses. To solve this issue two alternative coupling methods are studied: lateral (in-plane) coupling by means of an inverted taper and vertical (out-of-plane) coupling with a grating coupler. These structures are designed and simulated with the BPM and FDTD methods in order to study their performance characteristics. They show significantly better coupling than direct butt coupling to fiber.*

Index Terms—*Grating coupler, inverted taper, optical interface, photonics, PICSiP, silicon photonics, system integration*

1. INTRODUCTION

Technological frontiers between semiconductor technology, packaging, and system design tend to disappear towards a common vision of the future microelectronic systems. The design of chips, packages, and systems will have to be developed in a joint way in order to enhance the performance of future systems [1].

CMOS scaling has enabled the continuous performance enhancement within semiconductor industry in the last four decades. The improvements in order to achieve better performance, less power consumption, smaller footprint and reduced cost could be not ensured alone by reducing the geometries, since the semiconductor technology is approaching its physical limitations. “More than Moore” will be required in order to allow tighter integration of system level components at the package level [2].

Today’s integrated chips have to meet many requirements, and these cannot always be met with conventional packaging and interconnect technologies. There are that cannot be improved with conventional technology [3].

System-in-Package (SiP) technology is perhaps the most important technology to address these limitations. However, the overall performance, cost, size, and functionality of a SiP will be limited by the interconnects [3].

Electrical interconnects have limitations dealing with power consumption, interconnect area, and signal integrity at interconnect lengths as short as the board, module, and chip level as well. Technological changes will have to be introduced at the physical layer that allow further performance improvements in the future.

Optical interconnects arise in this situation as the optimal solution to overcome the limitations of electrical interconnects. Industry roadmaps are currently dealing with the integration of optical interconnects and optical functions into the board, package and chip-level electrical systems [4].

The combination of both the SiP technology and the optical interconnects form the so called Photonics Interconnection Layer for Converged Microsystems using System-in-Package Technology (PICSiP), which will be further discussed in this article. In order to integrate this new photonic layer in the SiP, the connection with the rest of the devices in the system has to be built. This is achieved by means of some coupling techniques. These can be basically in-plane or out-of-plane coupling structures.

2. PICSiP

The market demand for increased performance, smaller size, lower power and lower cost cannot be satisfied with conventional packaging and interconnect technologies. There are limitations in interconnect density, thermal management, bandwidth and signal integrity that cannot be solved with the existing technological solutions. System-in-Package technology is probably the most important technology to address these limitations [3].

SiP has evolved as an alternative to System-on-Chip (SoC) [5] for integration because this technology provides advantages over SoC in many market segments. SiP is not a substitute for high level, single chip, silicon integration but should be viewed as complementary to SoC. For some very high volume applications SoC will be

---

Manuscript received March 31, 2011. This work has been partly supported by the European FP7 research program PLATON, (Contract Nr: 249135). [a]Technische Universitaet Berlin, Research Center of Microperipheric Technologies, TIB 4/2-1, Gustav-Meyer-Allee 25, 13355 Berlin, Germany; [b]Fraunhofer Institute for Reliability and Microintegration (Fraunhofer IZM), Gustav-Meyer-Allee 25, 13355 Berlin, Germany.

T. C. Author is with the Research Center of Microperipheric Technologies of Technische Universitaet Berlin, Germany, Tel. +49 30 314 72537; Fax +49 30 314 72835 (e-mail: oriolgili@mailbox.tu-berlin.de).

the preferred approach. Some complex SiP products can contain SoC components [3].
The main goal of SiP is to integrate many different components (e.g. passives, MEMS or optical components) into a single package. A long term vision for SiP is the optimized heterogeneous integration of wireless, optical, fluidic and biological sensing interfaces. This goal requires new materials and control of their interactions in the submicron scale.
The improvements over SoC that SiP provides are, among others, more integration flexibility, faster time to market, lower Research and Development costs and lower product cost than SoC for many applications.
The objectives of using SiPs are therefore to provide alternate and cheaper solution for SOC, as SOC sometimes take longer to fabricate and reach the market, to provide higher levels of integration and better electrical performance, and to reduce overall assembly size and weight and achieve cost effectiveness [7].

The main advantages that SiP provides include:

- More functionality per package – each SIP may carry more modular functions,
- More capacity and higher efficiency,
- Easier board design and layout, quicker turn around and time to market,
- Higher manufacturing yield, lower cost and faster throughput,
- Better electrical performance could be achieved in most cases,
- Modular design and more interchangeable parts [4].

However, power consumption imposes the most serious limitation to the integration density that can be achieved. This issue will limit the packing density, size, cost, and performance of SiP [3].
These limitations can be addressed with optical interconnects.

Development of a high bandwidth photonic platform based on well established SiP technology will enable next generation optical computing architecture.

The PICSiP aims to provide a generic platform for further development independent from the application rather than addressing product related applications The main challenge remains the coupling of light in and out of nanophotonic circuits or photonics integrated circuits (PICs) by means of optical fibers or optical waveguides.

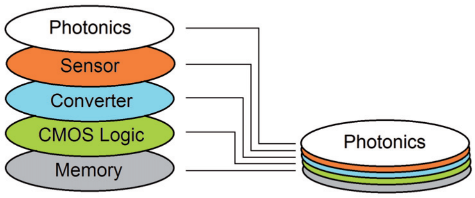

Fig.1: 3D System integration with photonics layer
(after [6])

3. OPTICAL INTERFACES TO PICSiP

The optical interconnects that are the base of this integrated photonic layer consist of optical nano waveguides built on silicon-on-insulator (SOI) wafers. The following section presents the proposed structure and the problems that arise in its coupling to fibers.

3.1 Silicon nano waveguide

The nano strip waveguide cross section is shown in Figure 2.

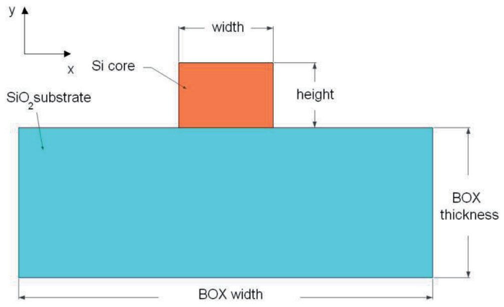

Fig.2: Strip nano waveguide cross section

The structure consists of a silicon waveguide core on top of a SiO_2 layer, called buried oxide (BOX) layer, on a silicon substrate (not represented in Fig.2). The following values for the effective indexes are taken: $n_{Si} = 3.48$, $n_{SiO2} = 1.46$, $n_{air} = 1$. The performance of such waveguides will be studied for both polarisations at a wavelength of $\lambda = 1.55$ µm. The coupling losses to fiber and the single mode region will be studied for core widths in the range 100 nm to 600 nm. The cross section is simulated with the Film Mode Matching (FMM) method. The mode distributions for every width for TE polarisation are shown in Figure 3. Similar results were obtained for TM polarisation.

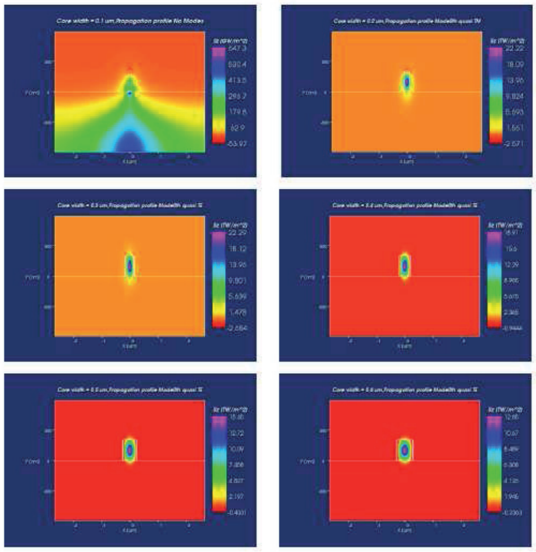

Fig.3 Mode distribution for TE polarisation

A width of the silicon waveguide core of 400 nm provides a single mode behaviour and good mode confinement characteristics for both polarisations.

3.2 Coupling to fiber

Efficient coupling between standard single mode fibers (SMF) and single mode waveguides is a key challenge for silicon nano waveguides. Integrated circuits need an interface to the outside world, and that is what the coupling devices attempt to provide.

The silicon waveguide is extremely small, with a core cross sectional area of approximately 0.1 µm², which correspond to core heights and widths around 0.4 µm. By comparison an optical fiber has a core with a cross sectional area of around 250 µm² (with a radius of 8-10 µm), three orders of magnitude larger, which makes coupling inefficient. Figure 4 shows the dimension differences between a SMF and a silicon single mode waveguide.

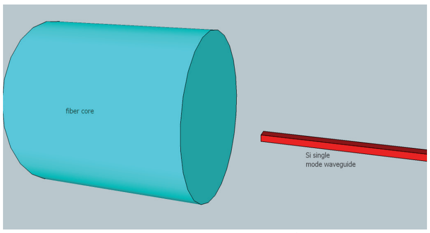

Fig. 4: Dimension mismatch between SMF and nano strip waveguides

The coupling losses for the direct butt coupling of a nano strip waveguide to a SMF have been calculated. Since the materials are considered ideal and no facet reflection is taken into account, the coupling losses are caused only by mode mismatch. The mode mismatch losses are found by means of an overlap integral between the propagated mode and a fiber Gaussian field with MFD = 5 µm for the core widths in the range from 100 nm to 600 nm. The results are presented in Figure 5.

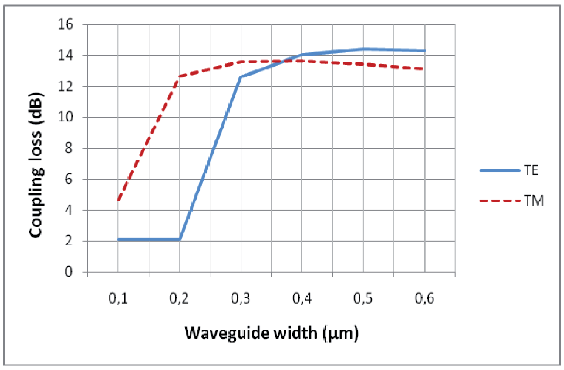

Fig.5: Coupling losses for TM and TE polarisation.

The widths in which there is propagation in the waveguide core (from 300 nm for TE polarisation and from 200 nm for TM polarisation) exhibit mode mismatch losses of around 13-14 dB. The mode distribution for the smaller widths is not concentrated in the waveguide core, and for this reason the calculated losses are lower.

These high coupling losses make necessary to find a solution to better couple both elements.

There are some approaches to the solution of this problem which have better performance as the simple butt coupling between the fiber and the waveguide, due to the elevated coupling losses that this method presents. There are two basic fiber to waveguide coupling schemes: lateral (in-plane) couplers and vertical (out-of-plane) couplers.

4. LATERAL COUPLING WITH INVERTED TAPER

Tapers that attempt to improve the coupling efficiency by reducing the mode dimensions of the field coming out of a SMF to fit them into the waveguide dimensions have been suggested. However, to avoid excessive coupling to radiation modes in the taper, the required typical taper length must be of the order of millimeters. In addition, these tapers suffer from strong back reflections at the facet of the coupler [8].

Inverted tapers, from the waveguide dimensions to the dimensions of a small tip, have been proposed for coupling laser diodes to optical fibers. These structures rely on the evanescent field at the tip to increase the mode size of the waveguide to that of the fiber [8].

Figure 6 shows an inverse taper and the alignment to the fiber. These kind of structures offer a robust coupling to fiber [9].

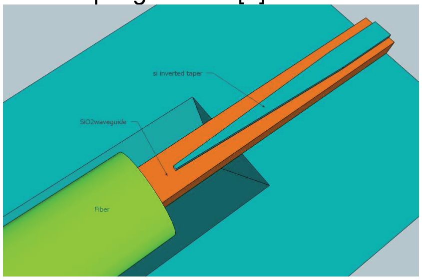

Fig.6: Inverted taper with V-groove alignment

The proposed inverted taper structure is shown in Figure 5. The layer structure is the same as for the nano waveguide. The input light is coupled to the BOX layer, under the narrow side of the taper, also called tip. The silicon core forms a taper to adapt the mode from the dimensions of this tip to the dimensions of the waveguide.

The following parameters have to be optimised:

- Width of SiO_2 waveguide,
- Inverted taper tip width,
- Inverted taper length.

These parameters will be studied for both polarisations as well, in order to obtain a polarisation insensitive structure. In addition, the spectral response and the alignment tolerances of the structure are discussed.

4.1 SiO_2 Waveguide design

The tip of the inverted taper can be directly attached to the optical fiber. However, in this condition, very exact control on the chip facets position is required and the coupling structure is polarisation sensitive. It is possible to couple the fiber directly to the BOX layer. The substrate of the SOI wafer is then removed. The objective is to find the optimal SiO_2 waveguide width to achieve the lowest coupling losses between the proposed structure and the single mode fiber.

The simulations are performed by means of the Beam Propagation Method (BPM), at a wavelength of 1.55 µm.

The mode mismatch losses between the fundamental mode in the SiO_2 layer and a Gaussian fiber field is represented for different MFD in Figure 7.

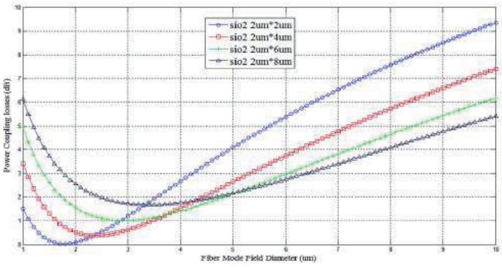

Fig.7: Coupling losses between the SiO_2 waveguide and the optical fiber as a function of the MFD for different waveguide widths.

The result is valid for both TE and TM polarisations. The coupling losses for a 6 µm wide SiO_2 waveguide and the single mode lensed fiber with MFD = 5 µm are around 2.2 dB. If the SiO_2 waveguide gets wider the estimated coupling losses do not significantly change. That means the structure is robust to fabrication errors.

4.2 Tip width design

The mode mismatch loss is calculated between the modes in the SiO_2 waveguide with and without the Si waveguide on top, for different core widths. Figure 8 shows these losses for both polarisations.

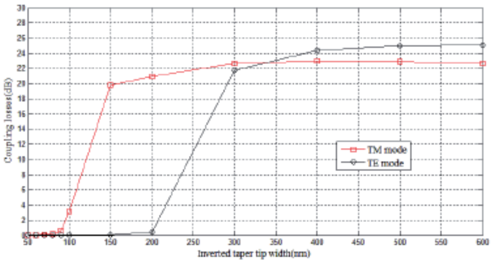

Fig. 8: Coupling losses between the SiO_2 waveguide with and without the inverted taper on top for different Si core widths.

For core widths under 70 nm, almost negligible coupling losses for both TE and TM polarisation are achieved. On the other hand, coupling losses are higher and do not significantly change as the inverted core width is wider than 300 nm. This occurs because the mode is mainly confined in the Si core and there is almost no overlap with the mode in the SiO_2 waveguide. The calculated losses between these two extreme values exhibit a highly polarisation sensitive behaviour.

According to these results, an inverted taper tip width lower than 70 nm is desirable to achieve a polarisation insensitive coupling structure.

4.3 Inverted taper length design

The power at the output waveguide has been measured for different taper length. Figure 9 shows the obtained results.

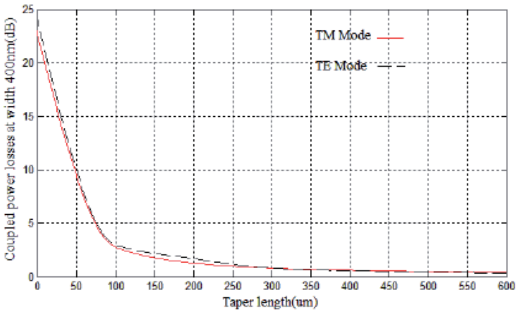

Fig.9: Coupling losses as a function of the taper length for TE and TM polarisation.

The coupling losses decrease as the inverted taper gets longer. The reason is that when the Si taper length gets longer, the change in width along the length is more progressive, and the mode profile changes slower too, so the mode mismatch loss is lower. Furthermore, it is interesting to notice that this improvement is similar for both TE and TM polarisations. The coupling losses for a length equal to zero is equivalent to the case of direct coupling to the fiber. The inverted taper length has to be chosen taking into account the tradeoff between minimum coupling losses and short lengths for both polarisations. For this length value, 0.31 dB coupling losses are achieved for TE polarisation while 0.39 dB coupling losses are achieved for TM polarisation.

4.4 Spectral analysis

The spectral response of the inverted taper structure is obtained for the wavelengths in the range from 1300 nm to 1590 nm. Figure 10 shows the obtained plot.

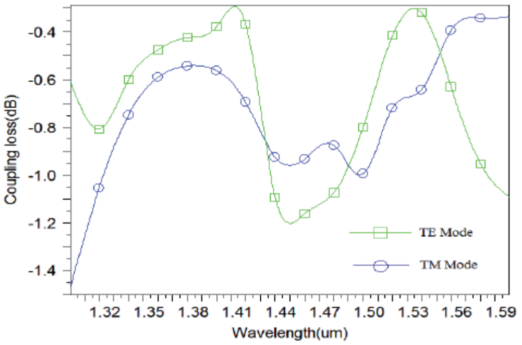

Fig.10: Spectral response for both polarisations

The losses for both polarisations at the wavelength of interest (1.55 µm) are quite similar. That means the structure is polarisation insensitive.

4.5 Alignment tolerance analysis

The robustness of the structure to misalignments is found by changing the position with respect to its centre where the light coming from the fiber is launched in the SiO_2 waveguide in the horizontal (x) and vertical (y) direction. Figure 11 shows the obtained results.

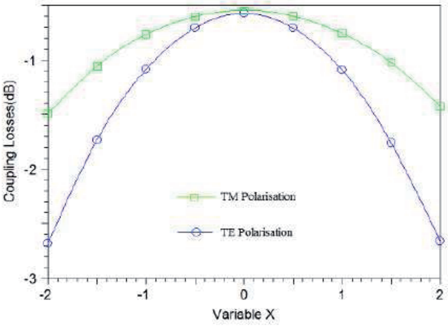

Fig.11: (a) Alignment tolerances in the x direction

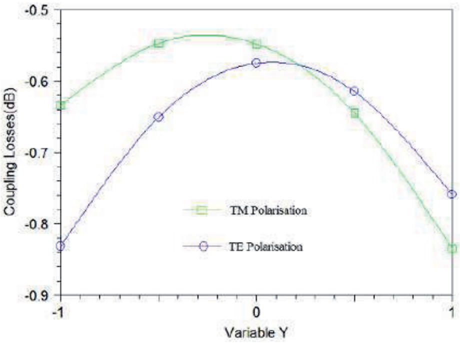

Fig.11: (b) Alignment tolerance in the y direction

The optimal coupling position in the horizontal direction is x = 0 for both polarisations. In the vertical direction the optimal position is different for every polarisation. For misalignments smaller than 0.5 µm in both directions, the effect of misalignment is negligible. Furthermore, in this case the misalignment tolerances for TM polarisation are better.

5. VERTICAL COUPLING WITH GRATING COUPLER

Another solution is to use grating couplers followed by a taper to adjust the lateral size of the incident beam to the sub-micrometer waveguide width.

These structures take advantage of the Bragg diffraction phenomenon to couple the light coming from a fiber. As shown in Figure 12, the grating coupler structure is composed of a corrugated silicon waveguide on top of a SiO_2 cladding or BOX. It is composed of grooves that are etched to the waveguide to a certain depth [11].

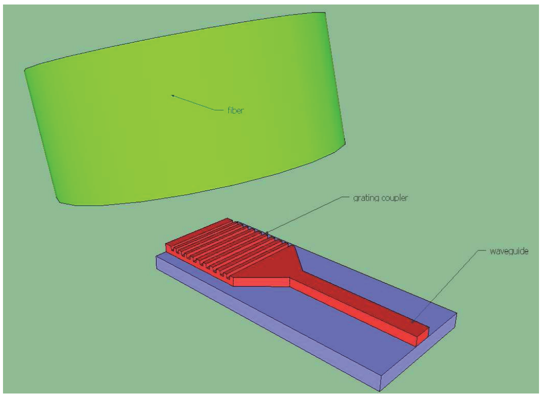

Fig.12: Grating coupler to fiber

The number of periods is chosen to make sure that the corrugated surface is properly illuminated by the fiber. The width of the grating is also chosen in the same way. A taper is placed at the output of the grating to reduce the mode dimensions from to the width of the strip nano waveguide, which is around 0.4 µm. Figure 13 shows the cross section of the grating.

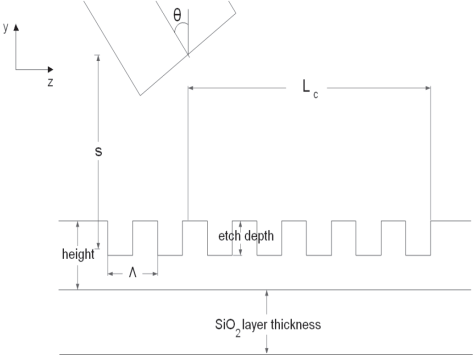

Fig.13: Grating coupler cross section

The performance of the structure will be studied for a variation in the following parameters:

- Etching depth (ed): depth with which the guiding silicon layer is etched, i.e. the depth of the grating grooves
- Grating period (Λ): its theoretical value is obtained from [9]:

$$\Lambda_{theor} = \frac{\lambda_0}{n_{eff} - n_{top} \sin\theta}$$

With n_{eff} the effective index of the guided mode, and n_{top} the refractive index of the background.

The alignment tolerances for the following parameters will be discussed:

- θ: incidence angle of the launched field.
- Coupling length in the y direction (s): vertical distance between the fiber core centre and the waveguide centre.
- Coupling length in the z direction (L_c) : it can be demonstrated that the length in the z direction between the fiber core centre and the beginning of the grating that provides maximal power at the output (expressed as $L_{c,\,opt}$) is equal to [9]:

$$L_{c,\,opt} = \frac{w_0}{1.37\cos\theta}$$

With w_0 half the width (MFD) of the Gaussian incident beam, and θ the incidence angle.

Additionally, the spectral response of the structure will be found.

The light coming from the fiber is approximated by a Gaussian field of MFD = 10 µm. We take TE polarisation into account, with λ = 1.55 µm. The coupling angle, or angle of incidence, is fixed to

8º, to break the symmetry of the structure. The field is launched at an horizontal distance to the end of the grating equal to 3.68 µm, and the vertical distance to the centre of the waveguide (s) is equal to 1 µm.

The Gaussian field is launched at this point, and then the power that reaches the output of the grating is measured, in order to obtain the efficiency. The whole structure is simulated with the Finite-Difference Time-Domain (FDTD) algorithm. A grating coupler for TE polarisation is designed in this section. With these parameters $n_{eff} = 3.00606$ and the period $\Lambda_{theor} = 0.54$ µm are obtained [9].

5.1 Grating period design

A vary run on the period is performed around the theoretical optimal value in order to find the coupling variation with the period. A maximal of 18% efficiency is found for 0.54 µm as well, with efficiencies over -3 dB of this maxima for period increments of ± 10 nm. The obtained results are shown in Figure 14.

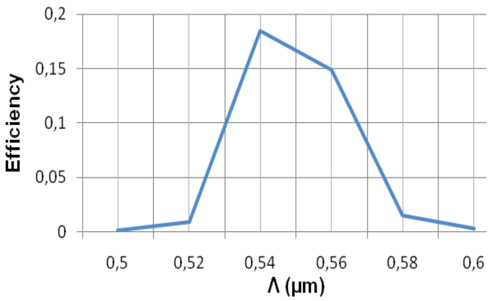

Figure 14: Grating period vary

5.2 Etch depth design

Once the period is found, the etch depth of the grooves of the grating is varied in order to see if the efficiency is improved. This etch is varied from 50 nm to 200 nm. The result plot is shown in Figure 15.

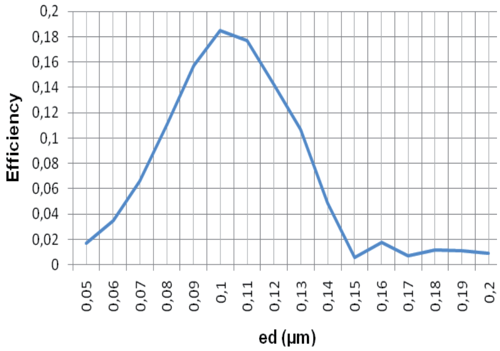

Fig. 15: Grating etching depth vary

If the grating is too shallow (the etch depth is too small) little light is coupled, and if the grating is too deep (the etch depth is too big) the same happens, because reflection increases, due to the fact that the incident beam does not see the silicon layer. So there is an optimal etching depth. The increments in etching depth that reduce the efficiency by less than 1 dB and 3 dB with respect of the optimal value are, respectively, ± 10 nm and ± 20 nm.

5.3 Spectral response and propagation profile

In order to find the spectral response for both polarisations of the simulated structure, the wavelength is varied in the range 1.5-1.6 µm. The resulting plot is shown in Figure 16.

The losses at the central frequency of 1.55 µm are around 7 dB. The 1 dB bandwidth is found to be 40 nm. The 3 dB bandwidth is about 60 nm. The response in the C-Band (1535 – 1570 nm), which is of much interest in most telecommunication applications, presents constant losses of under 1 dB respect to the peak value. The TE–TM extinction ratio is found to be 20 dB in the central wavelength.

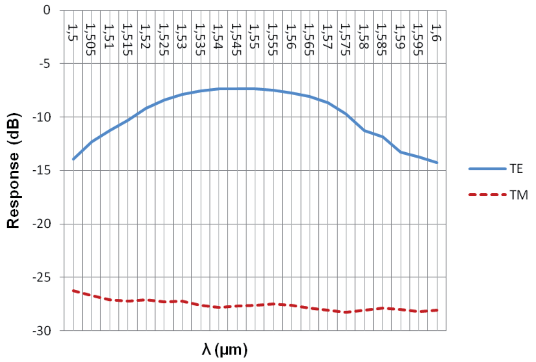

Fig. 16: Grating coupler spectral response

Figure 17 shows the propagation profile of the structure. A Gaussian field is launched to the grating. Some light is diffracted and couples to the waveguide, while some other goes through the structure and to the substrate. There is some reflection as well.

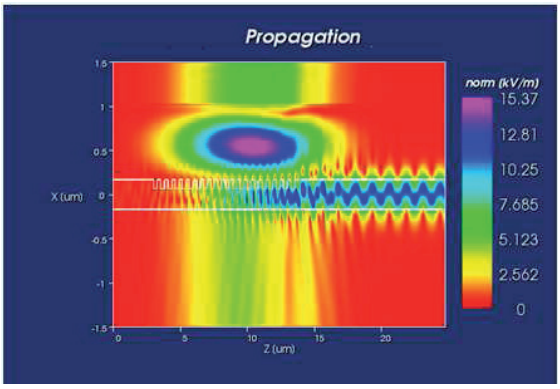

Fig.17: Grating coupler propagation profile

5.4 Alignment tolerance analysis

The launch parameters, which are the angle of incidence and the horizontal and vertical coupling lengths, are varied in order to see how these variations would affect the coupling of the structure in case of misalignments.

Firstly, the angle of incidence of the launched field is varied in order to find the alignment tolerances of the structure, that is, to what extent the output efficiency will decrease when the incidence angle is not the optimal one. This angle has been varied from 4º to 12º in steps of one degree. The resulting plot is shown in Figure 18.

These results show that the grating coupler is quite robust to misalignments of the fiber. The design optimal angle was 8º. Slightly better efficiencies are achieved for 6º and 7º. The increment of the angle of incidence that reduces the efficiency by 3 dB with respect of the design angle is ±3º.

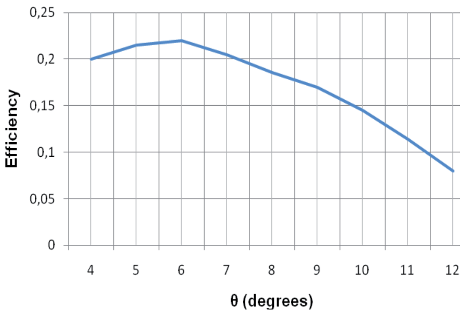

Fig. 18: Angle tolerances of the TE grating coupler.

The coupling length in the horizontal direction is varied in the range from 0 µm to 10 µm. The resulting plot is shown in Figure 19.

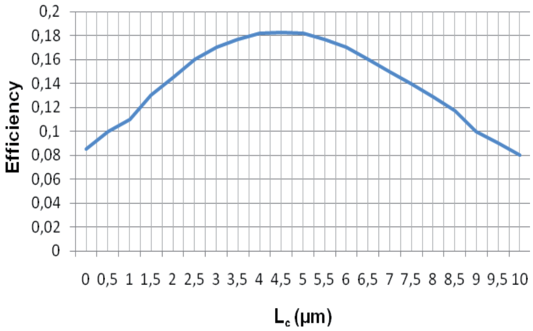

Fig. 19: Coupling length in the horizontal direction tolerances of the TE grating coupler.

The efficiency values in the whole simulated range stay bigger as half the maximal value. This optimal value was theoretically achieved for a length to the end of the grating of 3.68 µm. The efficiency stays more or less constant to coupling lengths up to 5 µm.
The vertical length to the coupler is also varied in the range 0.5 µm to 5 µm, as shown in Figure 20.

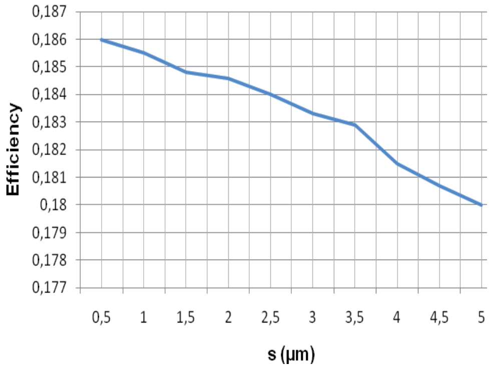

Fig.20: Coupling length in the vertical direction tolerances of the TE grating coupler.

The efficiency value does not significantly change in all the range, showing that the structure is robust to misalignments in the vertical direction.

6. CONCLUSION

In this article, single mode Silicon-on-Insulator nano waveguides and two mechanisms for their coupling to optical fiber have been presented, to be used as an optical interface in the Photonic Integrated Circuit System-in-Package technology.

Optical interconnects appear to be a good solution to overcome the limitations that electrical interconnects have. Optical nano waveguides show good theoretical performance, providing high miniaturization and strong confinement of light. Our simulations show that a single mode propagation region for both polarisations exists, for core widths of several hundred of nanometers, providing good propagation characteristics.

Two mechanisms to improve the coupling between the nano waveguides and single mode fibers have been presented: an inverted taper coupler and a grating coupler.

The inverted taper coupler presents low coupling losses and a broadband and polarisation insensitive behaviour, is quite robust to fabrication errors, but requires good alignment to the fiber and the reflections at the facets of the waveguide and the fiber have to be taken into account. Furthermore, this kind of structure can only perform the coupling at the end of the chip.

The grating coupler presents higher coupling losses, although several modifications can be made to improve its performance [10]. It is polarisation sensitive, since the design parameters are different for both polarisations, although this issue can be solved with 2D approaches [11]. It has smaller bandwidth than the taper coupler. It is relatively sensible to fabrication errors, but quite robust to misalignments of the fiber. The main advantage of this structure is that it can perform the coupling anywhere in the chip and the facet reflections are not so determinant.

ACKNOWLEDGMENT

The authors would like to thank José V. Galán for fruitful discussions and Arjen Bakker (PhoeniX Software, NL) for his kind support.

REFERENCES

[1] Gordon E. Moore, “Cramming More Components onto Integrated Circuits,” Electronics, pp. 114–117, April 19, 1965.

[2] Zhang, G.Q.; van Roosmalen, F.; Graef, M.; "The paradigm of "more than Moore" Electronic Packaging Technology", 2005 6th International Conference on 30 Aug.-2 Sept. 2005 Page(s):17 - 24

[3] W.Chen, W.R. Bottoms, K.Pressen, J.Wolf, “The next step in assembly and packaging: system level integration-SiP”, International Technology Roadmap for Semiconductors http://www.itrs.net/Links/2007ITRS/LinkedFiles/AP/AP_Paper.pdf, 2009.

[4] N.M. Jokerst, M.A. Brooke, Sang-Yeon Cho, S. Wilkinson, M. Vrazel, S. Fike, J. Tabler, Yoong Joon Joo, Sang-Woo Seo, D. Scott Wills, and A. Brown., “The Heterogeneous Integration of Optical Interconnections Into Integrated Microsystems*”, IEEE Journal of Selected Topics in Quantum Electronics*, vol.9, no.2, pp. 2003, 350-360.

[5] Rao R. Tummala, Vijay K. Madisetti,"System on chip or system on package?" IEEE Design & Test of computers, pp.48-56, April–June 1999

[6] T.Tekin, M.Töpper, H. Reichl., “PICSiP: New System-in-Package Technology Using A High Bandwidth Photonic Interconnection Layer For Converged Microsystems”, *Proc. SPIE*, 2009, Vol.7366, 736618.

[7] Wei Koh, “System-in-Package (SiP) Technology Applications”, *6th International Conference on Electronic Packaging Technology*, 2005, pp. 61-66.

[8] V.R. Almeida, R.R. Panepucci, M.Lipson, “Nanotaper for compact mode conversion”, *Optics Letters*, 2003, Vol. 28, no. 15, pp.1302-1304.

[9] J. V. Galán, "Addressing Fiber-to-Chip Coupling Issues in Silicon Photonics", *Universidad Politécnica de Valencia*, 2010, PhD Thesis.

[10] G. Roelkens, D. Vermeulen, S. Selvaraja, R. Halir, W. Bogaerts, and D. Van Thourhout, "Grating-Based Optical Fiber Interfaces for Silicon-on-Insulator Photonic Integrated Circuits", 2010, IEEE Journal of Selected Topics in Quantum Electronics 1

[11] D. Taillaert, " Grating couplers as Interface between Optical Fibres and Nanophotonic Waveguides", Ghent University, 2004, PhD Thesis.

"Optical Coupling of SOI Waveguides and INP based Photodetectors“

Ludwig Mörl, Wolfgang Passenberg, Margit Ferstl, Detlef Schmidt
Timo Aalto, Mikko Harjanne, Markku Kapulainen, Sami Ylinen
Dries Van Thourhout, Peter De Heyn, Fraunhofer HHI Berlin

Silicon photonic micro-cavities, Raman-amplifiers, and ultra-small electro-optic modulators

Meister, Stefan; Al-Saadi, Aws; Franke, A., Bülent; Mahdi, Shaimaa; Kupijai, Sebastian;
Woggon, Ulrike; Zimmermann, Lars; Hui, Tian; Richter, H., Harald; Stolarek, David;
and Eichler, J., Hans

Abstract—*We have designed, fabricated and investigated one-dimensional (1D) micro-cavities in Silicon-on-Insulator (SOI) waveguides. The single mode waveguides were fabricated in a 220 nm silicon device layer. The 1D micro-cavities in Fabry-Perot structure consist of Bragg-mirror regions formed by 1D photonic crystals or by sinusoidal modulation of the waveguide width. The SOI photonic structures are produced in a CMOS environment on 200 mm wafers using 248 nm DUV lithography. The 1D micro-cavities are the basic elements for the development of ultra-small electro-optic modulators, already designed in a new opto-electronic layout. Compared to modulators based on Mach-Zehnder interferometers or ring resonators, the footprint as well as power consumption can be strongly reduced. The critical temperature sensitivity of resonant structures is for 1D micro-resonators more than one order of magnitude lower than for ring resonators.*

Furthermore, Raman-amplification is shown in SOI waveguides with 220 nm thickness. In a new design the Raman-amplification in such small waveguides, also called nanowires, will be enhanced by a p-i-n diode, which reduces the nonlinear absorption. Another aim is to demonstrate for the first time Raman-lasing in such nanowires.

Index Terms—*CMOS, electro-optic modulator, micro-cavity, micro-resonator, Raman-amplifier, Raman-laser, Silicon photonics, SOI waveguide*

1. *INTRODUCTION*

Silicon photonics, especially based on silicon-on-insulator (SOI) were attracted great attention in the last years. With an intrinsic bandgap of 1.1 eV silicon is transparent at wavelengths typically used for optical communication transmission, i.e. 1270 nm – 1625 nm. In addition, the possibility to produce silicon photonics devices in a complementary metal oxide semiconductor (CMOS) environment offers an opportunity for very low-cost photonic solutions. Furthermore, the ability to integrate silicon photonic devices with electronic control functions opens a wide range of applications from telecommunications to chip-to-chip interconnects on-chip communication as well as possible applications in emerging areas such as optical sensing and biomedical devices. [1]

Ultra-small cavities play an important role in photonic integrated circuits (PIC) by controlling light for trapping and emission of photons, lasing, switching, and optical filtering. Most popular structures are ring resonators and photonic crystal micro-cavities. One-dimensional (1D) micro-cavities [2,3] have a very small footprint and are, therefore, well suited for highly dense packaging.

Electro-optic modulators are one of the key components for high speed optical interconnects. High performance electro-optic modulation in silicon has been demonstrated using Mach-Zehnder modulators [4]. Those modulator devices have lengths in the mm-range. For effective chip-scale integration, such electro-optic modulators are inappropriate. More recently, electro-optic modulators based on ring resonators were demonstrated [5]. The small modulators have ring diameters down to 12 µm and modulation frequencies of > 10 GHz. If the size of the rings is further reduced to < 10 µm, the guided mode is leaking out of the ring waveguide. Therefore, reduction of the footprint of the modulator is limited. Another problem is the high temperature sensitivity of the ring resonators of 1.3 nm/K [6]. With a bandwidth of less than 0.1 nm the requirement on the temperature stability is extremely high.

The footprint of electro-optic modulators can be further reduced by using 1D micro-resonators. Also the temperature sensitivity of such resonators is more than one order of magnitude smaller as for the ring resonators [3]. But up to now, only 250 MHz modulation frequency could be demonstrated [6]. Therefore, further investigations are required to increase the modulation speed.

In PIC an amplification of the optical data signal may be required. Raman-amplification could be a

---

Manuscript received March 31, 2011. This work was supported in part by the BMBF/VDI in the frame of project 13N9732 “SiliconLight”.

S. Meister, A. Al-Saadi, A.B. Franke, S. Mahdi, S. Kupijai, U. Woggon, and H. J. Eichler are with the Institut für Optik und Atomare Physik, TU- Berlin, Straße des 17. Juni 135 10623, Berlin, Germany. Contact person: S. Meister (e-mail: smeister@physik.tu-berlin.de)

L. Zimmermann, T. Hui, H. H Richter, D. Stolarek, are with Innovations for High Performance microelectronics (IHP) GmbH, Im Technologiepark 25, 15236 Frankfurt (Oder), Germany

solution to refresh an optical data signal guided in SOI waveguides. Furthermore, Raman-lasers based on SOI waveguides can be a very cost efficient solution for frequency conversion, e.g. for sensing applications.

2. FABRICATION OF SOI BASED PHOTONIC STRUCTURES

The SOI photonic structures were produced in a 0.13 µm SiGe BiCMOS environment at IHP GmbH, Frankfurt (Oder), Germany. The photonic devices were fabricated on 200 mm SOI wafers using 248 nm DUV lithography. Waveguides as well as the micro-cavities are designed using a single mask and fabricated in a shallow trench process. The waveguides and the micro-cavity related structures are etched completely down to the BOX layer, which has a thickness of 2 µm.

Physically, the waveguides were formed by inserting two parallel running grooves into the silicon surface, whose distance to each other defines the waveguide width. These lateral trenches are wide enough to prevent waveguide leakage into the surrounding intact top SOI areas.

For a well-defined filter performance, a single-mode behavior of the utilized strip waveguide is aimed. For the given waveguide height of h = 220 nm, a width of w = 500 nm is suited to assure singlemode transmission in the wavelength range around 1550 nm.

For optical testing requirements, the waveguides are extended on both sides of the photonic crystals by about 750 µm, and input and output ports are laterally displaced by ±50 µm in opposite directions via S-bends to prevent from light transmitted directly through the substrate [7]. The total waveguide length results then in about 1.5 mm, where the photonic crystal micro-cavity is located in the central singlemode waveguide section, which is only about 100 µm long. The waveguide is widened adiabatically to about 2 µm on both sides of the photonic crystal region, and the input and output ends are again widened to 5 µm in width in order to ease light coupling.

3. 1D MICRO-CAVITIES

In this paper, two different kinds of 1D micro-cavities are investigated. The micro-cavities are based on 1D photonic crystals as well as width modulated SOI waveguides. The micro-cavities act as band pass filters. The filter design parameters, e.g. number of holes, cavity length, number of cavities, etc., are systematically changed to investigate the potential of such 1D micro-cavities.

3.1 1D photonic crystal micro-cavities

The filters here are designed for the telecommunications wavelength range around 1550 nm (including C and L Band). The micro-cavities are formed by one-dimensional photonic crystals in Fabry-Perot structure directly written in rectangular waveguides. Fig. 1 shows the basic structure and parameters of the photonic crystal micro-cavities.

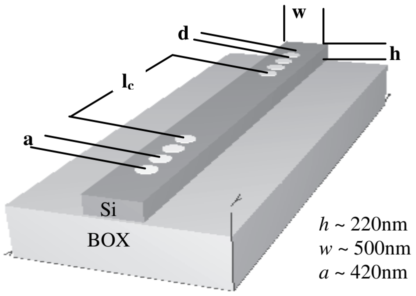

Fig. 1: Basic structure and parameters of the photonic crystal micro-cavities.

The lattice constant a and cavity length l_c are both measured from center to center between neighboring holes. The rectangular waveguides (nanowires) are fabricated in the 220 nm thick silicon device layer of the SOI substrate. Therefore, the waveguide height is fixed to h = 220 nm.

Different photonic crystal micro-cavities, e.g. single cavities of first and higher order as well as multi-cavity filters, were designed and investigated in order to achieve the desired spectral shape of the filter function for several applications. Furthermore, several design parameters were changed systematically to find out optimum settings. As a result, a large number of different photonic crystal micro-cavity structures have been implemented in our mask design.

The fixed lattice constants a = 420 nm have been chosen for all photonic crystal mirrors, see Fig. 1. Also the waveguide width was set to w = 500 nm in the design. Different hole diameters between d = 200 nm and d = 260 nm were realized in the mask design. The micro-cavities were designed with photonic crystal mirror pairs of 2 to 6 holes, e.g. 4+4 holes. For the first order cavity filters, six different cavity lengths l_c were introduced, ranging from l_c = 610 nm to 660 nm in steps of 10 nm. The higher order cavities were designed in a symmetric structure, e.g. 3+6+3 holes as shown in Fig. 2.

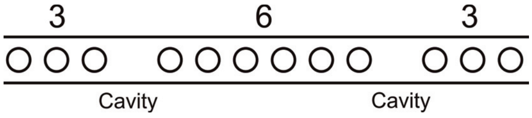

Fig. 2: Structure of a photonic crystal double cavity filter with 3+6+3 holes.

Fig. 3 shows a SEM image of a first order photonic crystal micro-cavity in a rectangular waveguide. Seen are the two etched tranches in the 220 nm Si top layer forming the waveguide. The holes are etched completely down to the SiO_2 BOX layer.

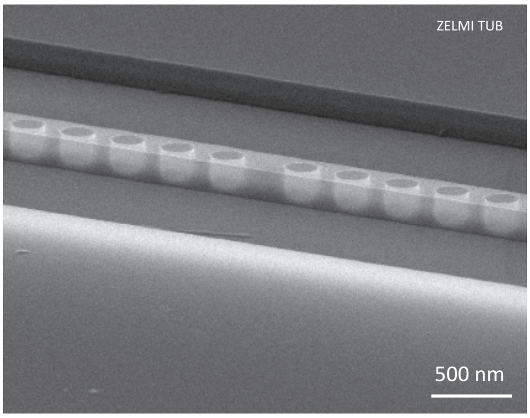

Fig. 3: SEM image of a first order photonic crystal micro-cavity in a SOI waveguide.

Fig. 4 shows the experimental setup for optical characterization of the 1D micro-cavities. The samples to be tested were fixed on a specially constructed vacuum chuck with integrated temperature control on top of a translation stage. Coupled SLEDs, providing a broad spectral range of 1200 nm – 1700 nm, serve as white light (WL) sources for transmission measurements. Alternatively, a tunable external cavity laser (ECL), with a wavelength ranged from 1520 to 1630 nm and a bandwidth of < 1 pm is used as light sources. The light was coupled to the SOI waveguides via tapered optical fibers with a focal diameter of 2.5 µm and a working distance of 14 µm.

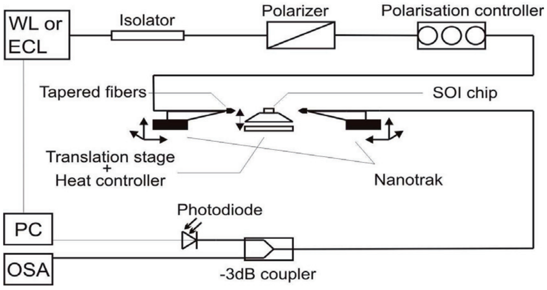

Fig. 4: Experimental setup for optical characterization of the micro-cavities.

TE polarization (E-field along the wider waveguide side) is necessary to excite the cavity modes. In order to achieve TE polarization at the waveguide input, a fiber optic polarizer followed by a polarization controller was inserted. The output light was measured by an Optical Spectrum Analyzer (OSA) or photodiode, respectively.

Fig. 5 shows the transmission band of a micro-cavity formed by two identical photonic crystal mirrors with 4+4 holes. The cavity is of the first order, which means the cavity length l_c has the shortest possible length for a certain transmission peak wavelength. In a classical Fabry-Perot, this would correspond to an optical spacer thickness of $\lambda/2$, if λ is the center wavelength at the transmission band of the micro-cavity. The diameter of the holes was d = 200 nm and the cavity length l_c = 630 nm.

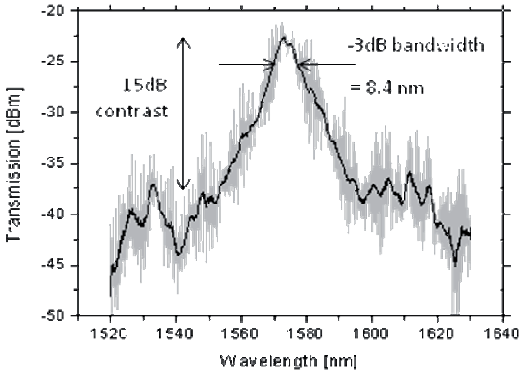

Fig. 5: Transmission peak of a first order photonic crystal micro-cavity with 4+4 holes.

The -3 dB bandwidth of the filter is 8.4 nm. The filter contrast is about 15 dB for wavelengths 30 nm off to the filter peak. In insertion loss of the filter is 2.7 dB.

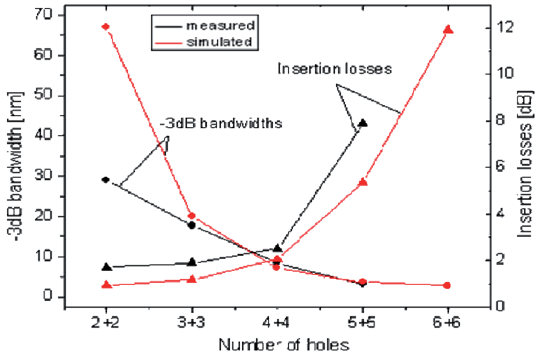

Fig. 6: Bandwidth and losses of first order micro-cavities depending on the number of holes.

Fig. 6 shows the -3 dB bandwidth as well as the insertion losses of micro-cavities depending on the numbers of holes. The -3 dB bandwidth of the filters is strongly decreasing with the number of holes. That is obvious, because the number of holes in the photonic crystal mirrors on both sides of the micro-cavity dictates the mirror reflectivity, which is responsible for cavity mode confinement. With an increasing number of holes in the mirrors, an increasing reflectivity results and, therefore, a higher filter finesse arises. On the other hand, the insertion loss of the filters grows with the number of holes, as seen in Fig. 6. Since these losses limit the mode confinement also the maximum filter finesse is limited. Therefore, the minimal bandwidth becomes saturated by further increasing the number of holes.

In order to decrease the bandwidth of the micro-cavities, the order of the cavity can be increased. The cavity length l_c of higher order filters can then be estimated by

$$l_{cH.O} = l_{c1.O} + (m - 1)\lambda/2n_{eff}.$$

$l_{c1.O}$ is the cavity length of the single order filter, here 630 nm, and n_{eff} = 2.40 is the effective refractive index of the SOI waveguide. The integer m gives the order number of the cavities.

Fig. 7 shows the -3 dB bandwidth of the filter peaks for 5 different cavity orders corresponding to different cavity lengths, respectively. All filters consist of 4+4 holes and have hole diameters of 200 nm. The bandwidths of the filters decrease with the cavity order and start to saturate for high order numbers. The simulated bandwidths are somewhat smaller but showing the same trend.

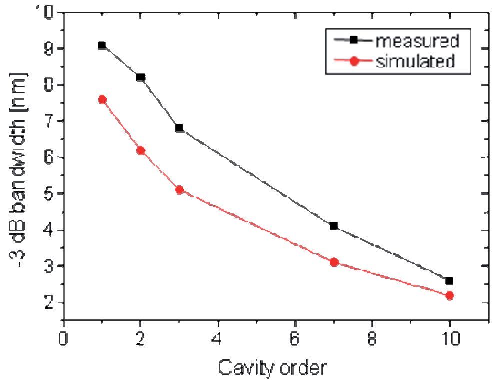

Fig. 7: Bandwidth of photonic crystal micro-cavities depending on the cavity order.

Fig. 8 shows the transmission spectrum of a 10th order single cavity filter with a cavity length of 3537 nm. The -3dB bandwidth of this filter is 2.4 nm. For a center-wavelength of 1580 nm this corresponds to a quality factor of Q = 660. The insertion loss of this filter is 4.7 dB.

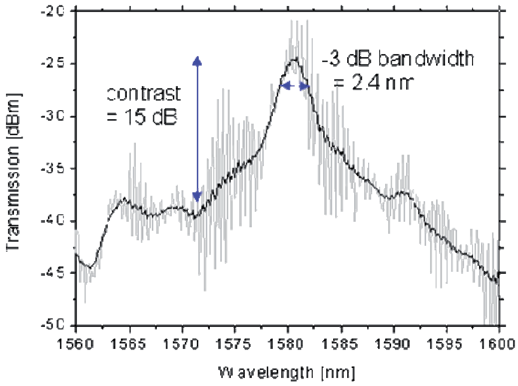

Fig. 8: Transmission spectrum of a 10th order single cavity filter.

Multi-cavity filters are useful to shape the transmission curve. Especially, the flat top shape and the strong decay in transmission at the edges of the filter curve make this kind of filter attractive for several applications, e.g. WDM.

Therefore, beside the single cavities, double and triple cavity filters are investigated in this work. Fig. 9 shows the measured and the simulated (inset) transmission band of a 3+6+6+3 multi-cavity filter. The cavity lengths of the filter are of first order and the outer mirrors consist of 3 holes. All holes have a diameter of 200 nm. The measured and simulated filter curves show very similar shape. The measured insertion loss of the filter was 3.5 dB.

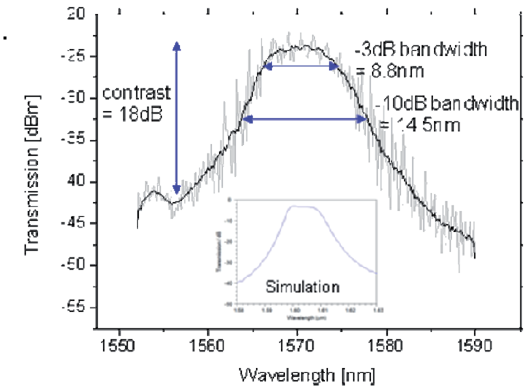

Fig. 9: Transmission spectrum of a first order triple-cavity filter with 3+6+6+3 holes.

The -3 dB bandwidth of the filters decrease with the number of cavities to about one half for the 3+6+6+3 filter compared to a single cavity 3+3 filter. A much stronger decay of about one fourth was observed for the -10dB bandwidths [3].

3.2 *Width modulated micro-cavities*

The 1D width modulated micro-cavities in Fabry-Perot structure consist of two Bragg-mirror regions separated by a sub-micron spacer. The two mirror regions are formed by modulation of the waveguide width. In the design, the mirror regions are defined by pairs of so called half-holes on both sides of the waveguide. The centers of the holes are placed on the edges of the waveguides. Fig. 10 shows the basic design structure and parameters of the width modulated micro-cavities.

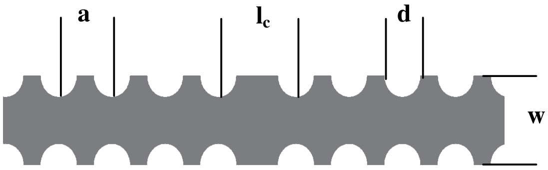

Fig. 10: Basic design structure and parameters of the width modulated micro-cavities.

The lattice constant *a* (fixed to 390 nm) and cavity length l_c are both measured from center to center between neighboring half-holes. The rectangular waveguides are similar as that in the previous section. Different half-hole diameters between *d* = 160 nm and *d* = 220 nm were realized in the mask design [8]. The micro-cavities were designed with two mirror regions of 10 or 20 half-holes pairs, e.g. 20+20 half-holes pairs. The half-hole diameter as well as the number of half-holes change the mirror reflectivity and therefore the filter bandwidth.

The SEM image in Fig. 11 shows a top view of a 1D micro-cavity. The two width modulated mirror regions were designed with 10 half-holes each. Between the mirror regions is seen the slightly wider spacer. Also seen are the two etched trenches forming the waveguide.

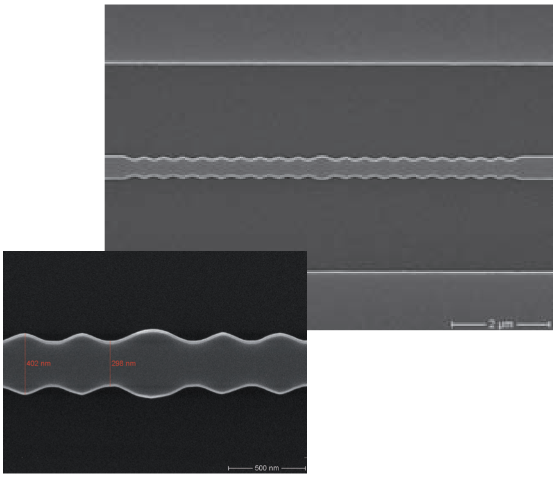

Fig. 11: SEM image of a 1D width modulated micro-cavity with 10 designed half-hole pairs in each of the two mirror regions (10+10) and a sub-micron spacer in the center of the cavity.

The higher magnification in Fig. 11 shows that the waveguide between the designed half-holes are rounded due to fabrication process leading to a sinusoidal modulation of the waveguide width. Also the sub-micron spacer in the center of the images is rounded.

Fig. 12 shows the transmission spectrum of a width modulated micro-cavity filter with 10+10 designed half-holes. The diameter of the designed half-holes was *d* = 180 nm and the cavity length l_c = 600 nm.

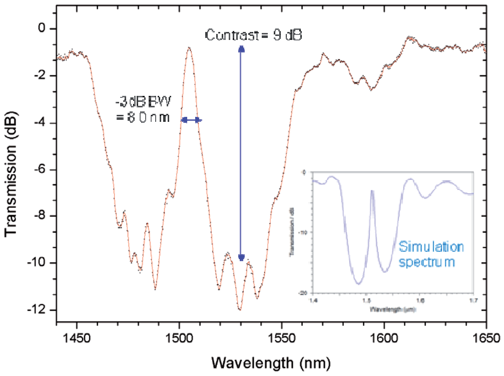

Fig. 12: Transmission band of a width modulated micro-cavity filter with 10+10 designed half-holes.

The transmission spectrum of the micro-cavity exhibits a stop band from 1460 nm to 1550 nm with low transmission. Due to the relative low index contrast in the mirror regions, the width of the low transmission range is relative narrow. The transmission peak of the filter is located in the center of the stop band. The -3 dB bandwidth of the transmission peak is 8.0 nm, which corresponds to a quality factor of Q = 188. The filter contrast is about 9 dB for wavelengths 10 nm off to the filter peak. The 0.8 dB insertion loss of the filter is very low. The insertion in Fig. 12 shows a simulated spectrum of this filter structure.

If the number of designed half-holes in the mirrors is increased to 20, the reflectivity of the Bragg mirrors will be higher. The transmission spectrum of a 20+20 width modulated micro-cavity is shown in Fig. 13. The diameter of the designed half-holes was *d* = 200 nm and the cavity length l_c = 570 nm.

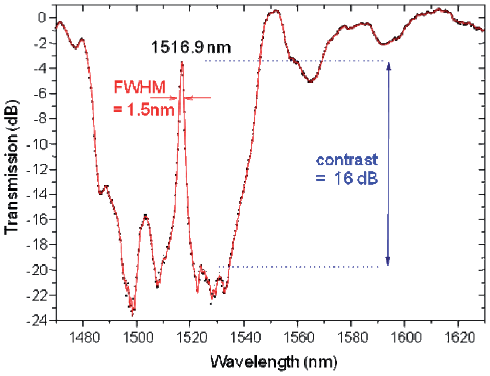

Fig. 12: Transmission band of a width modulated micro-cavity filter with 20+20 designed half-holes.

Due to the higher mirror reflectivity the -3 dB bandwidth of this filter is narrowed to 1.5 nm, which corresponds to a quality factor of Q = 1000. The filter contrast is increased to 13 dB for wavelengths 6 nm off the filter peak. The 1.9 dB insertion loss is low for such a filter.

4. *SOI-BASED RAMAN-AMPLIFIER*

Stimulated Raman amplification in silicon on insulator (SOI) waveguides is investigated. In silicon the strongest Stokes peak corresponds to first order Raman scattering from the three fold degenerate optical modes at the center of the Brillouin zone. It lies 15.6 THz away from the pump.

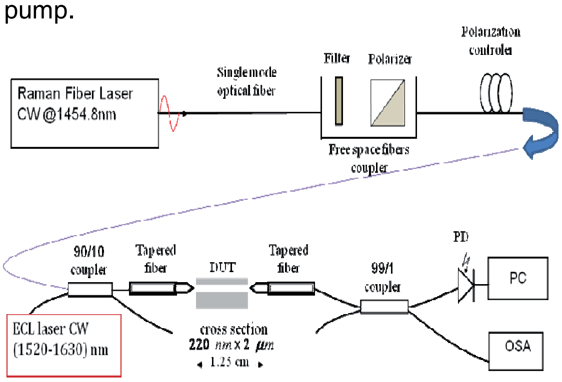

Fig. 13: Experimental setup for Stimulated Raman amplification measurements in SOI waveguides.

The experimental setup is shown in Fig. 13. A fiber coupled CW laser at 1454.8 nm with < 0.1 nm spectral width is used as pump source. An external cavity laser (ECL) with ~ 1 pm linewidth serves as probe source. A 90/10 coupler is used to couple the pump and probe together. A tapered fiber helps to couple the pump and probe into the silicon waveguide. The coupling efficiency is estimated to be around 10%.

The tested SOI waveguides had 2 µm width, 220 nm height, and 1.25 cm length. With 1454.8 nm pump, the first Stokes is measured at 1574.2 nm. We subtract the output power of the ECL without pump from the amplified signal around 1574 nm to obtain the amplification curve, shown in Fig. 14.

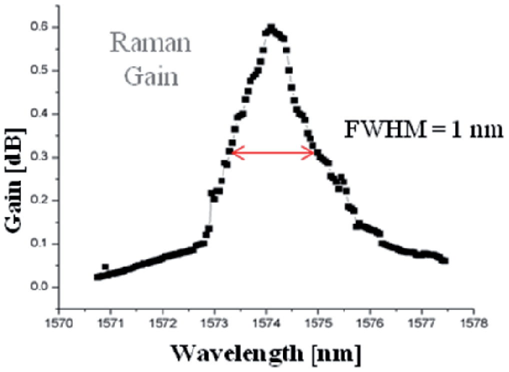

Fig. 14: Raman gain spectrum in a SOI waveguide with 1454.8 nm pump.

With 35 mW CW pump power inside the waveguide 0.6 dB gain (which corresponds to 15 %) has been determined, with both pump and probe being TE polarized. The bandwidth of the Raman gain is 1.5 nm. From the experimental data the stimulated Raman gain coefficient is estimated to 35 cm/GW.

5. OPTO-ELECTRONIC DEVICES

In this chapter, future prospects of our developments in the field of silicon photonic devices for communication and sensing applications will be given. A new layout with about 700 opto-electronic devices was designed at TU Berlin in cooperation with TFH Wildau, TU Hamburg Harburg, Hochschule für Telekommunikation, Leipzig, and IHP, Frankfurt (Oder). The active SOI photonic structures will be fabricated in the 0.13 µm SiGe BiCMOS production line at IHP GmbH, Frankfurt (Oder), Germany.

A main focus is the development of ultra-small electro-optic modulators and Raman-lasers and –amplifiers. The layout consist of 10 layer with photonic structures (waveguides including resonators), electro-optic structures (e.g. p-i-n diodes along the waveguides) as well as CMOS based electric contacts and passivation. The whole layout is shown in Fig. 15.

The basic structure of the ultra-small modulators is shown in Fig. 16. The modulators consist of a waveguide with a 1D photonic crystal resonator. The waveguide in the cavity is part of a p-i-n diode. By applying a voltage on the diode, free carriers are injected or depleted in or out of the cavity, respectively. The waveguide is not completely etched down to the BOX layer. A remaining slab of 50 nm allows the injection or depletion of free carrier. By the so call free carrier plasma dispersion effect the refractive index of the silicon in the waveguide will be changed. The change of refractive index in the cavity shifts the spectral position of the transmission peak, see Fig. 17, and therefore the intensity of the transmitted light can be modulated.

The modulators are only a few micrometers in length and because the current flow scales with the length of the p-i-n diode, such resonator structures can operate with very low power consumption.

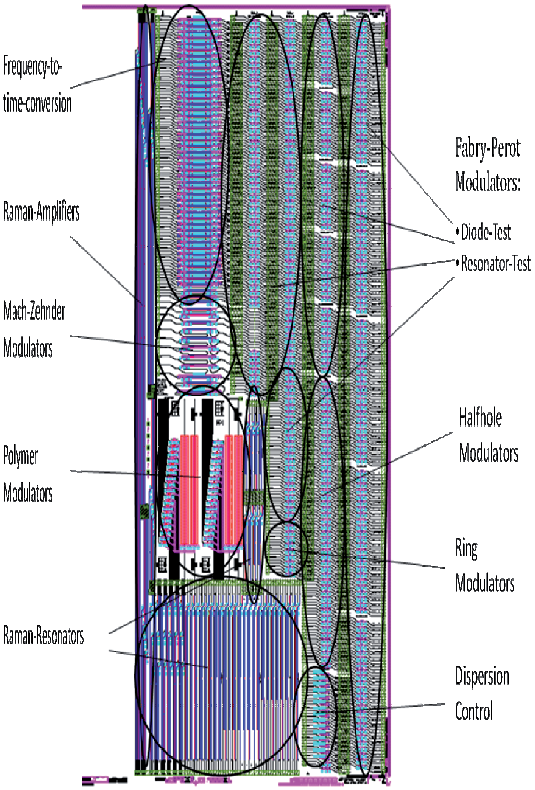

Fig. 15: Layout with about 700 opto-electronic structures.

In the layout, several design parameters are systematically iterated to optimize the modulators for modulation frequency, extinction ratio, etc. The aim is to achieve 10 GHz modulation frequency with a novel diode configuration [9], which reduces absorption and provides very low energy consumption per bit.

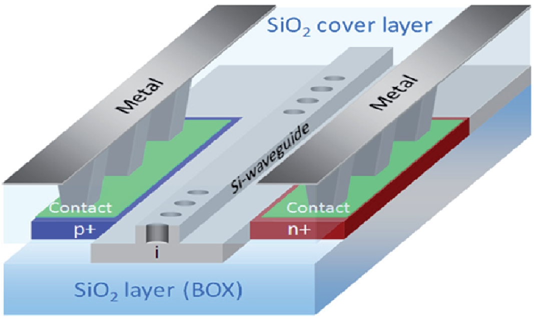

Fig. 16: Basic structure of ultra-small electro-optic modulators.

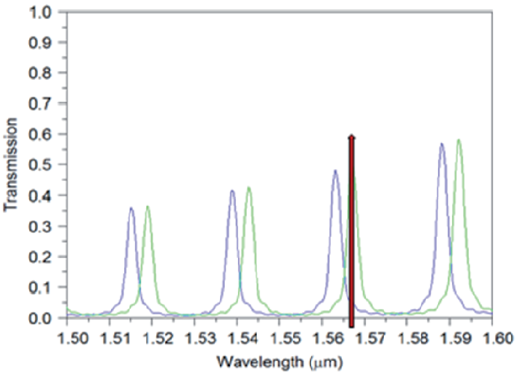

Fig. 17: The spectral change of the transmission peak can be used for intensity modulation of the transmitted light.

The very high Raman gain coefficient in silicon, given in section 4, makes this material very attractive for the development of Raman-laser and -amplifier. Also the strong mode confinement in SOI based waveguides support the nonlinear Raman-effect. But the small band gap of silicon (1.1 eV) and the use of communication wavelength around 1550 nm leads to strong two-photon absorption induced free carrier absorption.

If a reverse bias is applied to a p-i-n diode alongside the SOI waveguide, the free carriers can be removed out of the waveguide and therefore, the nonlinear absorption can be strongly reduced. In 1.5 µm x 1.5 µm rib waveguides highly efficient Raman-lasing are demonstrated [10]. Our aim is to demonstrate efficient Raman-lasers and -amplifiers in the ultrasmall 220 nm x 500 nm waveguides. In the layout, Fig. 15, p-i-n diodes along such waveguide are designed. Beside straight waveguides of different length for Raman-amplification, ring resonators with directional couplers are used as laser cavities, see Fig. 18.

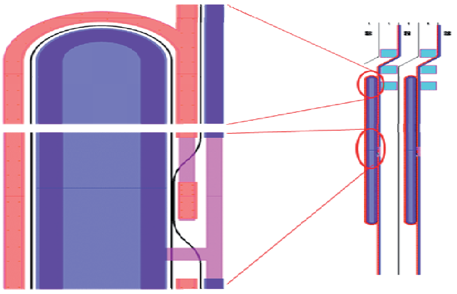

Fig. 18: Ring resonators with directional couplers as Raman-laser cavity.

Parameters like resonator length, coupling coefficients, etc. are iterated to optimize conversion efficiency.

6. CONCLUSION

Electro-optic modulators are key elements for photonic communication devices. We have investigated 1D micro-cavities in SOI waveguides fabricated in a CMOS environment. This passive structures act as band pass filters and has been chosen as basic elements for the development of ultra-small electro-optic modulators. Such modulators have the potential to overcome the drawbacks of size and power consumption of Mach-Zehnder modulators and of the critical temperature sensitivity of modulators based on ring resonators. Applications for those modulators are mass markets like short range fiber communication as well as chip-to-chip and on-chip communication.

Especially for optical sensing applications, effective frequency conversation using SRS effect has great potential. Raman-lasing in SOI nanowires would be a further step towards highly integrated and cost efficient solutions.

ACKNOWLEDGMENT

We like to thank Berndt Kuhlow and Christian Meuer, TU Berlin, for great support.

REFERENCES

[1] Izhaky, N., Morse, M. T., Koehl, S., Cohen, O., Rubin, D., Barkai, A., Sarid, G., Cohen, R., Paniccia, M. J., “Development of CMOS-Compatible integrated silicon photonics devices”, IEEE Journal of selected optics in quantum electronics, 2006, pp.1688.

[2] Foresi, J. S., Villeneuve, P. R., Ferrera, J.,Thoen, E. R., Steinmeyer, G. , Fan, S. , Joannopoulos, J. D. Kimerling, L. C., Smith, H. I., Ippen, E. P., "Photonic-bandgap micro-cavities in optical waveguides", Nature, 1997, pp. 143-135.

[3] Meister, S., Franke, B. A., Mahdi, S., Al-Saadi, A., Kuhlow, B., Voigt, K., Tillack, B., Richter, H. H., Zimmermann, L., Schrader, S., Ksianzou, V., Eichler, H. J., “Photonic crystal microcavities in SOI waveguides produced in a CMOS environment”, Proc. SPIE, 2010, pp. 7606-41.

[4] Green, W., et al., “Ultra-compact, low RF power, 10 Gbp/s silicon Mach-Zehnder modulator,” Optics Express, 2007, pp. 17106-17113.

[5] Xu, Q., Schmidt, B., Pradhan, S., Lipson, M., “Micrometre-scale silicon electro-optic modulator”, Nature, 2005, pp. 325-327.

[6] Schmidt, B., Xu, Q., Shakya, J., Manipatruni, S., Lipson, “Compact electro-optic modulator on silicon-on-insulator substrates using cavities with ultra-small modal volumes”, Optics Express, 2007, pp. 3140-3148.

[7] M., Kuhlow, B., Przyrembel, G., Schlüter, S., Fürst, W., Steingrüber, R., & Weimann, Ch., "Photonic Crystal Microcavities in SOI Photonic Wires for WDM Filter Applications", Journal of Lightwave Technology, 2007, pp. 421-431.

[8] B. A., Mahdi, S., Szczambura, M., Kuhlow, B., Woggon, U., Zimmermann, L., Richter, H. H., Stolarek, D., Schrader, S., Eichler, H. J., , “Micro-cavities based on width modulated SOI waveguides”, Proc. SPIE, 2011, pp. 7943-28.

[9] Meister, S., Al-Saadi, A., Eichler, H.J., Franke, B. A., Tillack, B., Zimmermann, L., „Elektrooptischer Modulator“, Deutsche Patentanmeldung, 2011, No. 10 2011 005 422.7

[10] Rong H., Xu, S., Cohen, O., Raday, O., Lee, M., Sih, V., Paniccia, M., “A cascaded silicon Raman laser“, Nature Photonics, 2008, pp. 170 – 174.

Stefan Meister received a Diploma degree in device engineering from Fachhochschule für Technik und Wirtschaft, Berlin, Germany, in 1995, a Diploma degree in physics from Technische Universität Berlin, in 2001 and a Ph.D. degree in Physics from the Technische Universität Berlin, in 2008. Since 2002, he has been with the Institut für Optik und Atomare Physik at TU Berlin. During his PhD studies, he was engaged in nonlinear phenomena in multimode optical fibers and functional optical coatings on fiber end-faces. Since 2008 he has been established silicon photonics research at the Institut für Optik und Atomare Physik, in cooperation with IHP GmbH, Frankfurt (Oder). His current research interests include light modulation and SRS in silicon as well as nonlinear effects in polymers.

Reconfigurable Spectral Phase Encoder in a Silicon Photonics Platform

Jamshidi, Kambiz; Meister, Stefan; Al-Saadi, Aws; and Schneider, Thomas

Abstract— ***We propose a reconfigurable spectral phase encoder in a silicon photonics platform. The proposed structure can be used to implement several functions in all optical signal processing like producing a tunable delay or adding variable dispersion to the incoming pulses. In our design we use cascaded ring resonators as dispersion modules for the functions require for frequency-to-time and time-to-frequency conversion. The parameters of the structure are optimized to maximize the dispersion produced by the resonators while satisfying the required bandwidth of the incoming signal. We show by simulation that the implementation of the proposed structure is possible in a CMOS environment.***

Index Terms— ***Integrated optic devices, ring resonators, all optical delay generation, frequency-to-time conversion.***

1. INTRODUCTION

ENCODING the spectrum of the optical signals has several applications in all optical signal processing. All optical delay generators and all optical dispersion producers are some of the subsystems which can be implemented by a spectral phase encoder [1]. Based on these subsystems several applications like optical code division multiple access (CDMA) systems, time resolved spectroscopy, nonlinear optics, optical coherence tomography, phased array antennas, and all optical buffering can be realized [2]. In this paper we propose an integrated solution based on silicon-on-insulator (SOI) technology to realize a reconfigurable spectral phase encoder via a simple configuration.

SOI based Silicon photonics attracted great attention in the last years [3]. Silicon can be used for optical communication transmission due to the fact that it is transparent at wavelengths used for that purpose, i.e. 1270 nm –1625 nm. Also, silicon photonics devices can be produced in a complementary metal oxide semiconductor (CMOS) environment. This offers an opportunity for very low-cost photonic solutions. Furthermore, the ability to integrate silicon photonic devices with electronic control functions opens a wide range of applications from telecommunications to chip-to-chip interconnects, and on-chip communication [4].

2. THEORY

A Scheme of the proposed method is shown in Fig. 1. The idea is to map the different spectral components of the incoming signal into different delays and manipulate the spectrum via a phase modulator (PM) [5, 6] due to the fact that manipulation of the spectral components can be done easier in the time domain. Mapping between spectrum and time can be realized simply by a dispersive media, since dispersion means that different spectral components of the incoming signal travel with different speed. This process is named frequency-to-time conversion (FTTC). If the dispersion of the dispersive media is composed of just second order dispersion, we can have a linear mapping between the frequency and time. After encoding the spectrum of the incoming signal, the spectral components should be overlapped to reconstruct the signal. Thus, another dispersive media with dispersion equal to the dispersion of the FTTC but with inverted sign is used. This process is named time-to-frequency conversion (TTFC). Therefore, the whole system can be viewed as a reconfigurable spectral phase encoder.

For the realization of each subsystem, a proper phase modulation should be used. For example an optical delay can be produced by using a saw-tooth signal as the input to the phase modulator [6]. The amount of the delay is proportional to the slope of this signal and the second order dispersion of the dispersive media used for FTTC. For the generation or compensation of a n-th order dispersion, a n-th order electrical signal should be used as the input to the phase modulator. Also, a proper sequence of 0 and π phase shifts should be used for the realization of a spectrally phase encoded CDMA system.

Manuscript received March 31, 2011. This work was supported in part by the German Research Foundation (reference number: SCHN 716/6-2) and BMBF/VDI in the frame of project 13N9732 "SiliconLight".

K. Jamshidi and T. Schneider are with the Deutsche Telekom Hochschule für Telekommunikation Leipzig , Gustav-Freytag Str. 43-45, 04277, Leipzig, Germany . (e-mail: jamshidi@hft-leipzig.de).

S. Meister and A. Al-Saadi, are with the Institut für Optik und Atomare Physik, TU- Berlin, Straße des 17. Juni 135 10623, Berlin, Germany.

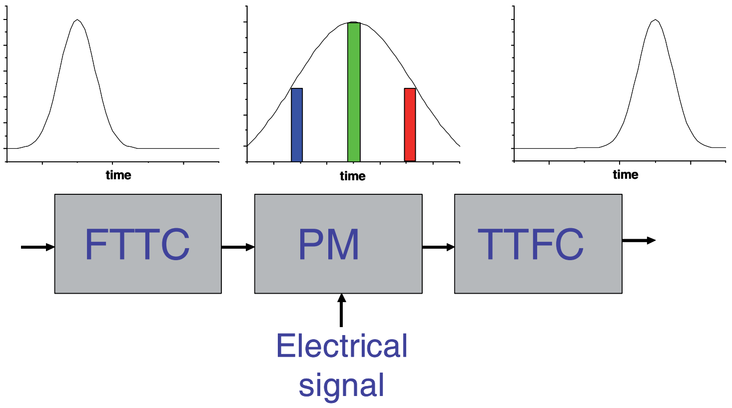

Fig. 1: Schematic diagram of the setup

3. IMPLEMENTATION

The Integration of an adjustable all optical delay generator into a silicon photonics platform is shown in Fig. 2. SOI based nano wires [7] are used in our design which allow very small bending radii. Integrated p-i-n junctions alongside the waveguides provide electro-optical functionalities by free carrier plasma dispersion effect. As can be seen in this figure we have used 2 pairs of ring resonators to produce the desired amount of dispersion for the TTFC and FTTC [8]. The phase modulator is implemented with a waveguide with p-i-n junction [9].

The group delay of the cascaded ring resonators can be written as [8]:

$$T_g = T\sum_{n=1}^{2} \exp(-j\varphi_n) \frac{k_n}{2-k_n-2\sqrt{1-k_n}\cos(\omega T-\varphi_n)} \tag{1}$$

where k_n is the power coupling ratio to the n-th resonator, T is the delay for one trip in the ring, and φ_n is the phase shift in the n-th resonator. First derivative of the group delay versus wavelength is the produced second order dispersion. The power coupling ratio and phase of each resonator should be optimized to produce high pure second order dispersion which is necessary to linearly map the different spectral components of the incoming signal into the time domain [5]. We could find a near flat second order dispersion in an acceptable frequency range for $k_1 = 88\%$, $k_2 = 96\%$, $\varphi_1 = \pi/2$, and $\varphi_2 = 84\pi/100$ by searching through the different values of parameters. The normalized dispersion produced by the cascaded ring resonators using these parameters is sketched in Fig. 3.

The normalized dispersion is defined as $D_n = -D\lambda^2/cT^2$, where D is the dispersion, λ is the wavelength of the incoming light, and c is the speed of light. The frequency axis is normalized to the free spectral range (FSR) which is the inverse of the round trip time in the resonator [T]. It can be seen that a flat second order dispersion can be obtained for 20 percent of the FSR around 0.22 X FSR. We have used the above mentioned results to choose the required parameters and finalized the design of the structure. Therefore, we have used resonators with a 200 µm length which has a FSR of 4.6 nm to support the linear dispersion for our input signal (A picosecond mode locked laser).

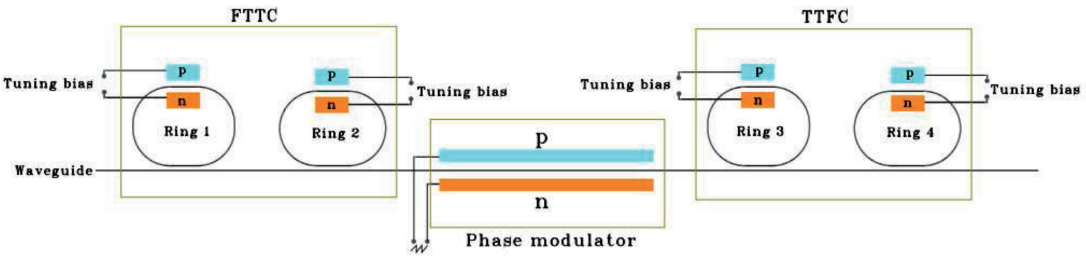

Fig. 2: Integration of the adjustable all optical delay generator into a silicon photonics platform

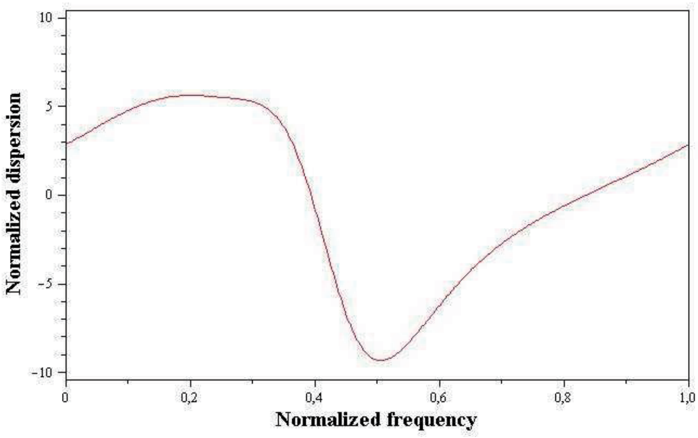

Fig. 3: Normalized dispersion vs. normalized frequency of the two cascaded ring resonators

We have simulated the coupling efficiency to the ring resonators using a FDTD method by RSOFT software. SiO_2 covered single mode waveguides with 220 nm x 450 nm dimensions were chosen for the full integration to the SOI platform which have a remaining Si slab of 50 nm for carrier injection. The gap for the waveguide coupler was set to 190 nm.

In Fig. 4 the coupling efficiency depending on the length of the waveguide coupler is shown. The bending radius is 12.5 µm to provide low bending losses. For the required coupling efficiencies of k_1=88 % and k_2=96 % the simulated coupler lengths are 7.8 µm and 9.3 µm, respectively. Simulation results (Fig. 4 inset) show that the technological requirements on the couplers are moderate and therefore such structures can be fabricated in a CMOS environment.

CONCLUSION

We have designed a reconfigurable spectral phase encoder by the idea of frequency-to-time conversion in a silicon photonics platform. The setup can produce variable delays and dispersions which can be used for several applications in all optical signal processing. We have shown by simulation that the setup can be fabricated in a CMOS environment.

ACKNOWLEDGMENT

The authors would like to thank H.J. Eichler from TU-Berlin, C. A. Bunge, S. Preußler, A. Wiatrek from Hochschule für Telekommunikation in Leipzig and G. Leuchs, G. Onishchukov from Max Planck institute in Erlangen and J. Reif from Brandenburg technical university in Cottbus for the fruitful discussions.

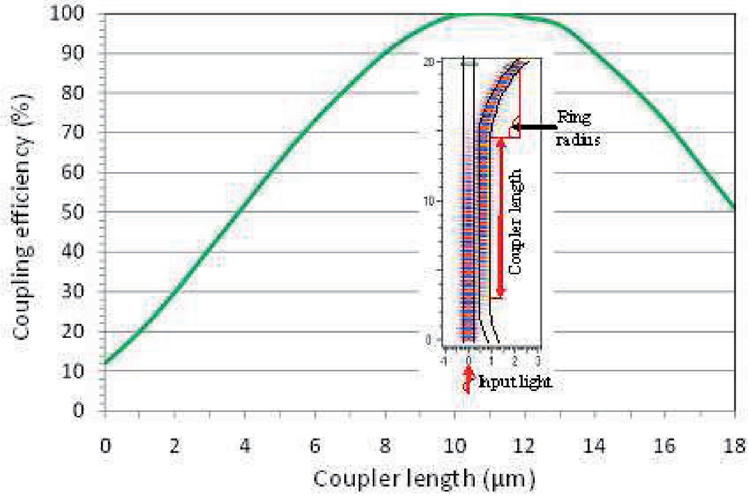

Fig. 4: Coupling efficiency versus the straight length of the waveguide coupler

REFERENCES

[1] Khaan, M. H., Shen, H., Xuan, Y., Zhao, L., Xiao, S., Leaird, D. E., and Weiner, A. M. “Ultrabroad-bandwidth arbitrary radiofrequency waveform generation with a silicon photonic chip-based spectral shaper”, Nature Photonics, 2010, pp. 117-122.

[2] Khurgin, J. B. “Optical buffers based on slow light in electromagnetically induced transparent media and coupled resonator structures: comparative analysis,” JOSA. B, 2005, pp. 1062-1074.

[3] Almeida, V. R. “All-optical control of light on a silicon chip,” Nature, 2004, pp. 1081-1084.

[4] Izhaky, N., et al, “Development of CMOS-Compatible integrated silicon photonics devices”, IEEE JSTQE, 2006, pp. 1688-1698.

[5] Jamshidi, K., et al., “A widely tunable optical delay generator,” OL, 2010, pp. 3592-3594.

[6] Jamshidi, K., et al, “Very large, tunable, positive and negative group delay for high-bandwidth signals,” in European Conference on Communication (ECOC), Turin, Italy, 2010, Th.9.C.5.

[7] Meister, S., et al., “Photonic crystal microcavities in SOI waveguides produced in a CMOS environment,” Proc. SPIE, 2010, pp. 7606-7641.

[8] Madsen, C. K., et al, “Multistage dispersion compensator using ring resonators,” Optics Letters, 1999, pp. 1555-1557.

[9] Green, W., et al., “Ultra-compact, low RF power, 10 Gbp/s silicon Mach-Zehnder modulator,” Optics Express, 2007, pp. 17106-17113.

Kambiz Jamshidi received the PhD degree in electrical engineering from Sharif University of Technology (SUT.), Tehran, Iran in 2006. He was with the high frequency technology (HFT) institute in Technical University of Berlin for 6 months during his PhD studies. He was with Advanced Communication Research Institute (ACRI) of SUT as a researcher from 2006 to 2009. Since May 2009, he has been a senior researcher with HFT institute at the Deutsche Telekom University of Applied Sciences in Leipzig. His research interests include nonlinear effects in optical fiber, optical signal processing, and optical CDMA. He is a member of IEEE and optical society of America (OSA).

Stefan Meister received a Diploma degree in device engineering from Fachhochschule für Technik und Wirtschaft, Berlin, Germany, in 1995, a Diploma degree in physics from Technische Universität Berlin, in 2001 and a Ph.D. degree in Physics from the Technische Universität Berlin, in 2008. Since 2002, he has been with the Institut für Optik und Atomare Physik at TU Berlin. During his PhD studies, he was engaged in nonlinear phenomena in multimode optical fibers and functional optical coatings on fiber end-faces. Since 2008 he has been established silicon photonics research at the Institut für Optik und Atomare Physik, in cooperation with IHP GmbH, Frankfurt (Oder). His current research interests include light modulation and SRS in silicon as well as nonlinear effects in polymers.

Thomas Schneider received the Diploma degree in electrical engineering from the Humboldt Universität zu Berlin, Germany, in 1995, and the Ph.D. degree in Physics from the Brandenburgische Technische Universität Cottbus, Germany in 2000. Since 2000, he has been with the Deutsche Telekom Hochschule für Telekommunikation (HfT) in Leipzig, Germany. Since 2006 he has been the head of the Institut für Hochfrequenztechnik at the HfT. During his doctoral studies, he was engaged in the investigation of nonlinear phenomena induced by an ultrafast refractive index grating. His current research interests include nonlinear optical effects in telcommunication systems, slow- and fast light, high resolution spectroscopy and the generation of millimeter and THz waves.

Invited Talk*: „Foundry-Prozesse für die Siliziumphotonik“*
Lars Zimmermann, TU Berlin

CMOS-Compatible Fabrication of Integrated Silicon Photonic Systems

Baus, M.; Wahlbrink, T.; Bolten, J.; Prinzen, A.; Manecke, C.; Kleinjans, H.; Porschatis, C.;
Lerch, H.; Waldow, M.; Merget, F.; Karl, M.; Kurz, H.

Abstract—*Silicon photonics is a maturing technology for compact, inexpensive integrated photonic circuits. Here, the development of reliable process modules based on complementary metal oxide semiconductor (CMOS) technology to implement optical and electro optical devices in silicon is reported. With these process modules both, passive and active circuitries, in silicon-on-insulator technology have been fabricated in a reproducible manner.*

Index Terms—*CMOS technology, silicon photonics, silicon-on-insulator, micro-heater, micro-ring, modulator*

1. *INTRODUCTION*

SILICON photonics is a maturing technology for compact, inexpensive integrated photonic circuits evolving for more than 25 years now [1]. Based on silicon-on-insulator (SOI) technology light is guided in submicron wide silicon waveguides strongly confined owing to the high refractive index contrast between silicon and silica. Due to this fact bend radii in the order of few microns can be realized without significant penalty, thus, giving photonic designers a versatile concept for a scalable, ultra-compact photonic platform at hand. Furthermore, electro-optical functionalities have been integrated and proved by adapting mature CMOS processes such as ion implantation and electric wiring capabilities. This set of process technologies opens the door for a boundless amount of integrated photonic components, while most significant building blocks comprise silicon based modulators [2] and detectors [3].

The most important CMOS compatible process steps have been developed to a complete set of capabilities for application in integrated silicon photonics.

2. *PHOTONIC SOI LAYER*

2.1 Basic Fabrication Process

Commonly used silicon waveguides for single-mode operation rely on cross-sections with a silicon core of about 450x220nm² and an oxide cladding for wavelengths in the C-band. Beside simple waveguides this cross-section can be used as well for further passive photonic elements like Y-splitters and ring resonators. Integrated micro ring resonator devices consist of a circular waveguide and two straight waveguides as shown in the scanning electron microscopy (SEM) picture Fig. 1. The adjacent waveguides serve as evanescent input and output couplers to the micro ring. Usually these waveguides are named as bus waveguides. The separation between the bus waveguides and the ring is between 100 nm and 500nm. For silicon photonic application typical radii of the rings are in the range of 5 µm to 50 µm. Passive micro ring resonator devices are used for all optical wavelength switching and routing. While active ring resonator structures allow high speed operation of silicon electro-optical modulators.

Figure 1: SEM image of a ring resonator with adjacent waveguides.

For the realization of such silicon photonic components in SOI substrate a dedicated lithography process has been developed based on electron beam lithography and a reactive ion

---

Manuscript received March 31, 2011. This work has been partly funded within the German project “INNOTRANS” by Bundesministerium für Bildung und Forschung under support code FKZ 13N10591. M.W. and F.M. are with University Aachen (RWTH), Institute for Semiconductor Technology (IHT), Sommerfeldstr. 24, 52074 Aachen, Germany. All other authors are with AMO GmbH, Otto-Blumenthal Str. 25, 52074 Aachen, Germany.

Any correspondence should be addressed to M.K. (karl@amo.de) or M.B. (baus@amo.de).

etching process: In a first step an electron beam sensitive resist with a negative tone (hydrogen silsesquioxane) is coated and exposed at 100kV and developed using highly concentrated tetramethyl ammonium hydroxide [4]. Afterwards the resist is used as a direct mask for a dry-etching process using an inductively-coupled plasma reactive ion etching tool (ICP-RIE) with HBr/O_2 chemistry resulting in pattern transfer into the SOI. The etching parameters have been optimized to minimize surface roughness. To demonstrate the smooth and steep surface of the fabricated silicon waveguides a close-up of the coupling region of an integrated ring resonator device is shown in Fig 2.

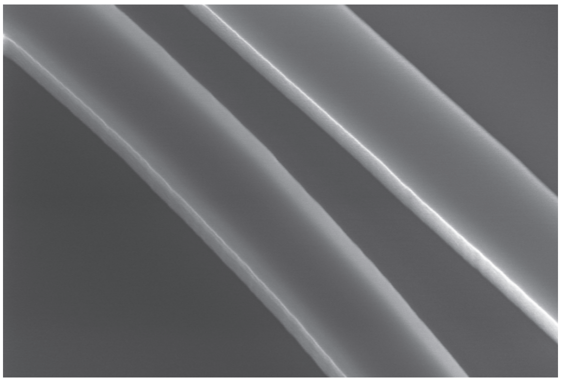

Figure 2: Close-up SEM view of the coupling region between a ring resonator and an adjacent waveguide (waveguide width 450nm).

High fabrication quality for optical micro-cavities has already been demonstrated by reaching quality factors of 140,000 for ring resonators [5]. These high quality factors have been achieved without applying any additional post processing fabrication steps.

For the use of integrated circuitry on a system level optical losses are most important [6]. One crucial figure of merit is the specific loss in a straight waveguide for single-mode operation. A reproducible value within 1.5 to 2dB/cm can be attributed to the described fabrication process; this is within state-of-the-art.

2.2 Fabrication Tolerances

For a reliable fabrication process an accurate control of the lateral dimension of the photonic structure is mandatory. To estimate the fabrication tolerances a suitable test design containing several ring resonator devices with adjacent bus waveguides and isolated straight waveguides has been realized with the basic fabrication process described above. The waveguide width has been determined by automated SEM inspection at about 80 positions on a chip. E-beam dose has been selected to generate a correct waveguide width in the HSQ resist of 450 nm for all structures. In this case no proximity effect corrections (PEC) were applied. The width was found to be accurate within the error of the SEM measurement (± 5nm). After structure transfer of the resist mask into the substrate material via ICP-RIE the fabricated chips have again been inspected with an SEM. The waveguide width has been measured for different types of structures (waveguide bus, coupling sections, ring sections) and in different areas of the chip. The result of this analysis for two chips, labeled chip01 and chip04, is presented in Fig. 3.

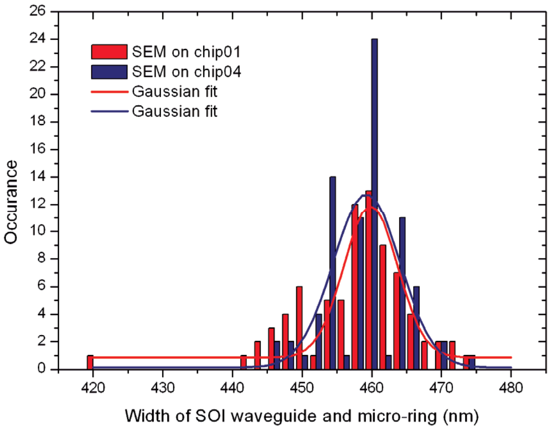

Figure 3: Final waveguide widths measured by SEM in realized circuitries at various positions (waveguide bus, coupling sections, ring sections). The fit to a Gaussian distribution shows a standard deviation of only 1% (5nm).

The number of waveguide structures which have been measured with a certain width is plotted versus this width. For both chips a Gaussian fit has been applied to this waveguide width distribution data. For both chips the maximum of this distribution is observed at a width of 460nm, with a full width at half maximum (FWHM) of ~10nm. The slight increase of the waveguide width measured after the etching compared to the width measured after EBL processing (450nm) demonstrates both the good critical-dimension control and the excellent steepness of the resulting etch profile. The FWHM value of about 10nm obtained from this analysis is already pleasing taking into account the fact that different type of waveguides – straight waveguide, coupling sections and ring sections – have been analyzed and compared and that the measurement accuracy of the SEM inspection is in the range of ±5nm.

The mentioned deviation in waveguide width has an impact on the resonance frequency in ring resonators since it changes the effective refractive index inside the waveguide structure. This results in a deviation of the resonances in the range of ±1nm within one chip, i.e., less than 0.1% of the absolute wavelength in near-infrared. Furthermore, there is a way to have absolute wavelength accuracy. This can be realized by placing heating elements on top of the rings, see section electrical functionality. For such structures a tuning range of more than 3nm with respect to the resonance wavelength can easily be achieved, see Fig. 4, so any fabrication tolerances can be overcompensated by far.

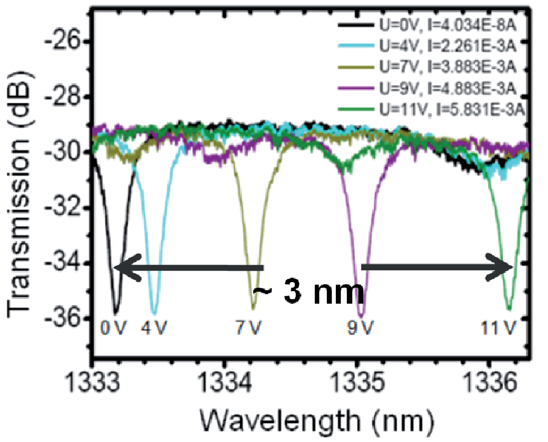

Figure 4: Tuning range of a resonance of a ring resonator with an integrated micro-heater.

2.3 Integrated Diodes

For most electro-optical applications in photonics ion implantation is required to build integrated lateral diode structures or at least a conductive top silicon region. We have developed processes to build lateral p-i-n diodes where the intrinsic region consists of the photonic waveguide, see Fig. 5. This allows for carrier injection into the waveguide, which causes carrier dispersion and therefore changes the effective refractive index of the waveguide. Dopants used are boron and arsenic for p- and n-type doping, respectively. Based on similar technology modulators for date rates exceeding 10Gbit/s have been demonstrated [7]. Furthermore, implantation parameters have been optimized with respect to low contact resistances to the electrical wiring stacked on top.

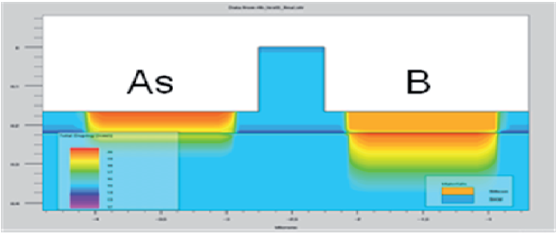

Figure 5: Simulated doping profile for a lateral p-i-n diode across a photonic waveguide.

3. ELECTRICAL FUNCTIONALITY

As discussed before the SOI layer hosts the photonics since the light is confined and guided therein. Building up integrated circuitries with added functionalities like micro heaters and integrated diode structures demands an electrical functionality on top. We have developed process modules containing four different layers: a first oxide layer to plane the photonic topography and to achieve an optical and electrical isolation; a first metal layer with titanium where heating elements can be implemented; a second oxide layer again for electrical and thermal isolation and a second metal layer with aluminum for electrical wiring with high electrical conductivity and capable to form transmission lines for high frequencies. The resulting layer stack is shown schematically in Fig. 6.

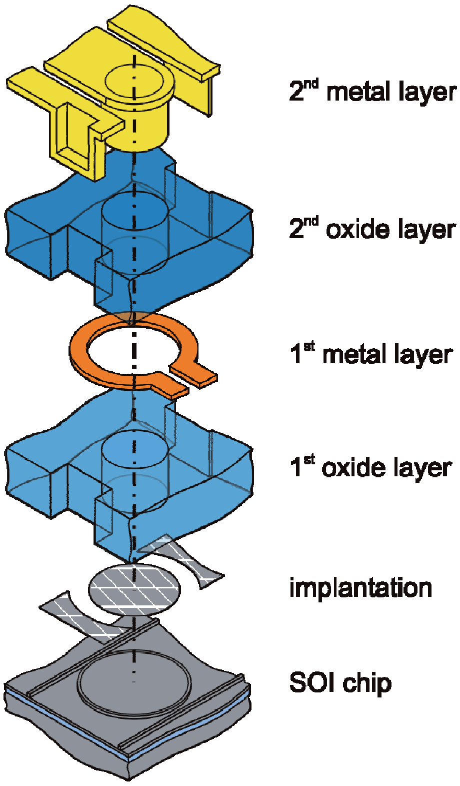

Figure 6: Exploded drawing of a modulator based on a ring resonator showing the layer stack of a final device.

Taking all these process modules for a modulator as shown in Fig. 6 it sums up to at least eight different and sequentially processed lithography steps which have to be aligned accordingly. The microscopic view of Fig. 7 shows a realized modulator device based on the carrier dispersion effect in injection-type configuration. Preliminary results are in good agreement with state-of-the-art achievements for such type of modulator scheme.

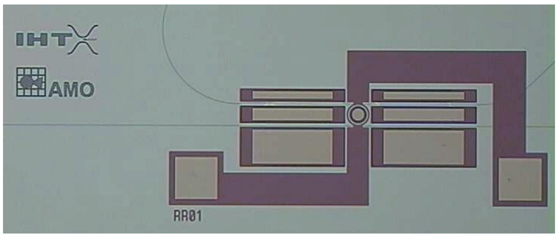

Figure 7: Microscopic image of a realized modulator device with integrated micro-heaters.

4. CONCLUSION

With the example of an integrated modulator based on ring resonators and carrier injection a complete set of CMOS-compatible process modules has been demonstrated to realize a silicon photonic circuitry. CMOS technology has a high level of maturity, thus, when limiting to CMOS-compatible processes for the realization of integrated silicon photonics inexpensive fabrication facilities for large scale production is available. The latter is an essential condition to make silicon photonics an overall success with manifold applications in everyday life.

REFERENCES

[1] Soref, R. A. and Lorenzo, J. P., IEEE Journal of Quantum Electronics vol. 22, pp 873 (1986).

[2] Reed, G. T. et al., “Silicon optical modulators,” Nat. Photonics 2010, vol 4, pp. 518-526.

[3] Casalino, M. et al., “Near-Infrared Sub-Bandgap All-Silicon Photodetectors: State of the Art and Perspectives,” Sensors 2010, vol. 10, pp. 10571-10600.

[4] Bolten, J. et al., “CMOS compatible cost-efficient fabrication of SOI grating couplers,“ Microelectronic Engineering, vol. 86, pp. 1114–1116, April 2009.

[5] Niehusmann, J. et al., “Ultrahigh-quality-factor silicon-on-insulator microring resonator,“ Optics Lett., vol. 29, pp 2861–2863, December 2004.

[6] Petracca, et al. "Photonic NoCs:System-Level Design Exploration," IEEE Micro, August 2009.

[7] Xu, Q. et al. “12.5 Gbit/s carrier-injection-based silicon micro-ring modulators,” Opt. Ex. vol. 17, pp 430-436 January 2007.

Tunable Finite Impulse Response Filter for Dispersion Compensation using Multi-Arm MZIs in SOI Technology

S. Schwarz, A. Rahim, J. Bruns, C. G. Schäffer, and K. Petermann

Abstract—*We present a planar serial-parallel filter architecture for the application as a dispersion equalizer in WDM systems and show that the use of several heating elements allows for a flexible tuning in the dispersion characteristic. The presented filter is designed in SOI platform for a channel spacing of 100 GHz. Comparison for simulated and measured transfer function for different tuning cases of a single stage of the filter shows a good agreement.*

Index Terms—dispersion compensation, optical filter, phase tuning, signal processing, silicon-on-insulator

1. *INTRODUCTION*

THE increasing demand and implementation of different services in the communication field such as IP-TV require a steady progress in extending today's transmission systems to supply higher data rates and multiple access to a rising number of customers. With the development and improvement of optical buried, rib or strip-loaded waveguide structures smaller, faster and more complex components could be realized to fulfill this need. These planar lightwave circuits (PLC) are mostly made of Si, SiO_2, InP, etc. and therefore can be integrated in today's CMOS technology. An example for an integration of optical communications functionality into a CMOS platform is demonstrated in [1]. Furthermore, many PLC devices, such as Multi/Demultiplexer [2], Add/Drop Switches [3], Mo/Demodulator [4], Microring Resonators [5] and Compensating Filter [6], have been presented so far. However, there are two reasons to implement some tuning possibility in the designed device architecture. On the one hand, manufacturing tolerances and mounting inaccuracies entail a reduction in quality of the designed function. On the other hand, the constantly changing requirements of today's transmission systems ask for flexibility. An example of this variation is the fluctuation of accumulated dispersion along a fiber link due to temperature changes. In addition, decaying performances of individual components lead to undesirable effects. For this reason, further treatment on device tuning is needed to achieve the best performance possible.

In this paper, we describe a tunable multistage filter in SOI technology which is able, as an example of a signal processing device, to compensate for dispersion. The flexible character is based on the ability to influence the filter architecture at closely positioned points on the chip without the drawback of tuning restrictions resulting from crosstalk between adjacent phase controllers. The operation, design and experimental results for a single stage are presented for this approach.

2. *DEVICE OPERATION*

2.1. General Schematic

Fig. 1 shows the general schematic of a serial-parallel FIR filter approach with *N* stages. It consists of *M* × *M* MMIs, delay lines of lengths 0*T*, 1*T*, …, (*M*-1)•*T* and phase controllers φ_{ij}. The time delay *T* defines the free spectral range (*FSR*), which relates to the spacing of filter response repetition on the frequency axis. The Filter in Fig. 1 has an order of *N*•(*M*-1) and one can either adjust the number of stages or the number of MMI ports to design a filter with certain order.

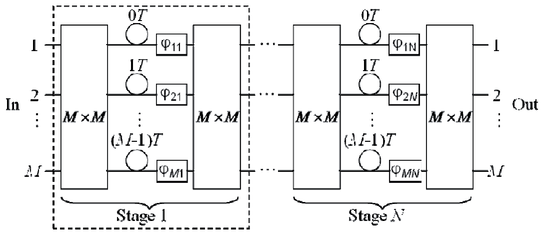

Fig. 1. General *N* stage serial-parallel filter. The dotted region denotes the building block.

Based on the filter description in the z-domain, each element's behavior can be written in matrix notation with wavelength independent parameters:

$$\underline{H}_{coupler}=\begin{bmatrix} \underline{s}_{11} & \cdots & \underline{s}_{M1} \\ \vdots & \ddots & \vdots \\ \underline{s}_{1M} & \cdots & \underline{s}_{MM} \end{bmatrix}, \text{with } \underline{s}_{ij}=\left|\underline{s}_{ij}\right|\cdot\exp(j\phi_{ij}) \quad (1)$$

Manuscript received March 31, 2011. This work was supported by the German Research Foundation (DFG).

S. Schwarz and C. G. Schaeffer are with the Department of High-Frequency Engineering and Optoelectronics, University of Armed Forces, Germany (E-mail: Stefan.Schwarz@hsu-hh.de).

A. Rahim, J. Bruns and K. Petermann are with the Institute of High Frequency Engineering, Berlin University of Technology, Germany.

$$\underline{H}_{\text{delay}} = \begin{bmatrix} z^{-0} & 0 & \cdots & \cdots & 0 \\ 0 & z^{-1} & 0 & \cdots & 0 \\ \vdots & 0 & \ddots & \ddots & 0 \\ \vdots & \vdots & \ddots & \ddots & 0 \\ 0 & 0 & 0 & 0 & z^{-(M-1)} \end{bmatrix} \qquad (2)$$

$$\underline{H}_{\text{phase, k}} = \begin{bmatrix} \exp(j\varphi_{1k}) & 0 & \cdots\cdots & & 0 \\ 0 & \exp(j\varphi_{2k}) & 0 & \cdots & 0 \\ \vdots & 0 & \ddots & \ddots & 0 \\ \vdots & \vdots & \ddots & \ddots & 0 \\ 0 & 0 & 0 & 0 & \exp(j\varphi_{Mk}) \end{bmatrix} . \qquad (3)$$

Experimental results have shown that this assumption is a good approximation for a wavelength span of over 15 nm. Finally, the multiplication of all blocks results in the filter transfer function of this architecture:

$$\underline{H}_{\text{filter}} = \underline{H}_{\text{coupler}} \cdot \underline{H}_{\text{phase, N}} \cdot \underline{H}_{\text{delay}} \cdot \underline{H}_{\text{coupler}} \cdot \ \ldots \ \cdot \underline{H}_{\text{coupler}} \cdot \qquad (4)$$

It should be taken into account that this notation of transfer function has to be extended to two contributions in case of a polarization dependent device.

2.2. Appl. Example: Dispersion Compensator

One application using this filter architecture is as an equalizing device for data transmission, which compensates for accumulated dispersion along a fiber link. In the upcoming transmission systems with symbol rates up to 50 Gbit/s and above as well as channel spacing of 100 GHz, the compensation of dispersion is essential. An easy solution to this problem could be the addition of a dispersion compensating fiber (DCF). However, it causes additional loss in signal strength because of its length and is fixed in its equalizing behavior. As consequence of a varying requirement in the amount of dispersion, due to changes in temperature or modification in network topology, an adaptive device has to be implemented.

The presented filter architecture of the order of $N \bullet (M\text{-}1)$ can perform this function. Each filter zero

$$\underline{z}_{0i} = \rho_{0i} \cdot \exp(j\vartheta_{0i}) \quad , \text{with } i = 1 \ldots (M\text{-}1) \cdot N \qquad (5)$$

gives an independent contribution to the overall filter response [7] whose shape and position on the frequency axis depends on the magnitude and phase of each zero, respectively. The complex values of these zeros, on the other hand, are affected by the coupling coefficients of the MMI couplers and phase relations between different propagating paths. With the help of phase controllers on the delay lines one is able to tune the filter and change its dispersion characteristic.

Fig. 2 and Fig. 3 show the group delay and dispersion contribution of one zero depending on its magnitude ρ. The *FSR* in this example is set to 100 GHz (0.8 nm) and has an inverse quadratic influence on the amount of dispersion.

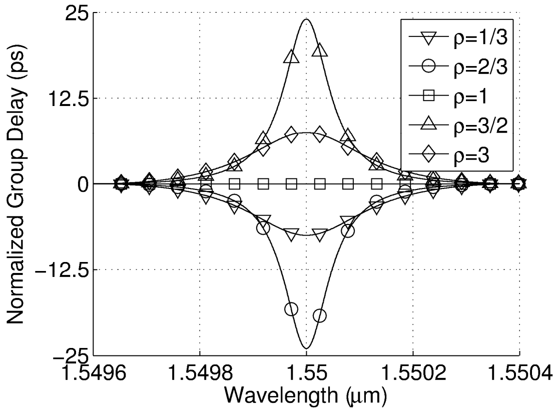

Fig. 2. Group Delay dependency on magnitude ρ of one zero.

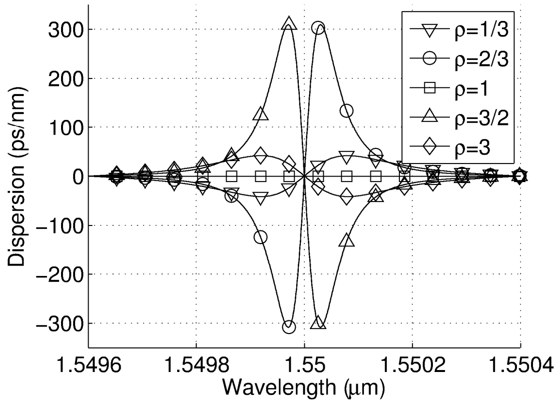

Fig. 3. Dispersion dependency on magnitude ρ of one zero.

As an example, a superposition of 6 zeros to achieve a nearly linear group delay slope and thus a constant dispersion response of approximately 250 ps/nm over 50% of the FSR is shown in Fig. 4 and Fig. 5. The maximum group delay ripple inside this relative bandwidth usable (*RBWU*) does not exceed 1.15 ps. Compared to the symbol duration, which is 25 ps at a symbol rate of 40 Gbit/s, this satisfying value demonstrates the potential of achieving flat dispersion curves with even a low number of zeros. It is therefore important to use a flexible architecture to get the maximum performance out of this low order filter device.

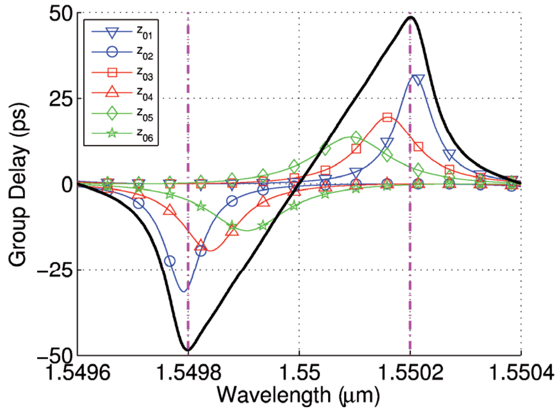

Fig. 4. Superposition of six zeros to form a nearly linear group delay slope. The relative bandwidth usable (*RBWU*) of 0.5 is marked between the vertical lines.

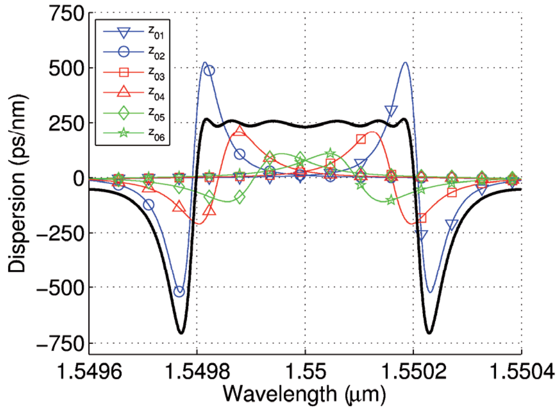

Fig. 5. Superposition of six zeros to form a nearly constant dispersion value.

The general filter architecture, shown in Fig. 1, can be used to design a 6th order filter. We choose two stages with 4 × 4 MMIs for this purpose. The middle MMI combining the two stages is replaced by a pair of 4 × 4 MMI couplers with additional heaters acting as a tunable power splitter, see Fig. 6. We use port 1 as the input port and select port 1 as the output port. Although limited in the degree of freedom, this filter can generate different states for dispersion compensation by a suitable choice of the tuning parameters for the phases on the delay lines. Fig. 7 illustrates 9 different cases for linear group delay slopes (-172 ps, -130 ps, -99 ps, -50 ps, 0 ps, 50 ps, 98 ps, 130 ps, 161 ps) over 66% of the FSR. Within this region the group delay ripples are below 2.5 ps.

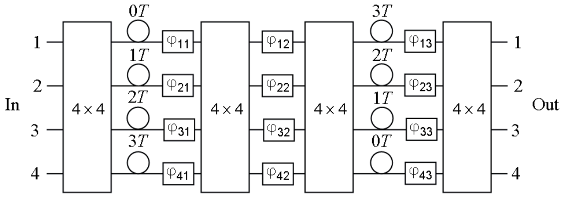

Fig. 6. Example for 2-stage serial-parallel filter with intermediate tunable coupler and switched 2nd stage.

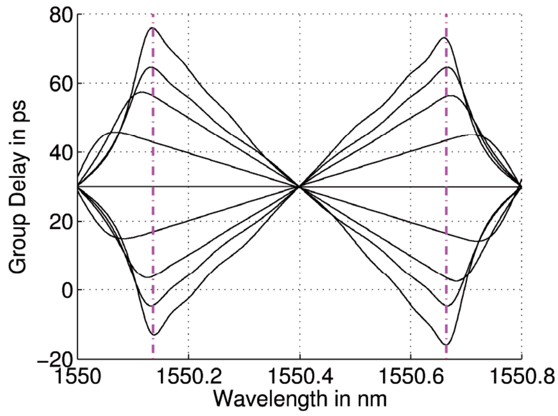

Fig. 7. Example for 9 different Group Delay Slope cases, Usable Bandwidth is 66% of FSR, Group Delay Ripple are below 2.5 ps within this range.

3. REALIZATION OF SINGLE STAGE SERIAL-PARALLEL FILTER

3.1. Device Layout and Fabrication

We have fabricated a single-stage of the serial-parallel filter with 4 × 4 MMIs on SOI wafer with 4 µm top silicon and 1 µm buried oxid, see Fig. 8. It must be kept in mind that one stage is not sufficient to compensate dispersion due to the limited filter order. However, it is useful for the proof of concept. The device has a size of 2.5 cm x 3 cm. Single mode waveguides with a width of 3.5 µm and an etch depth of 1.8 µm are implemented in the bended structure. Their relative difference in length is approximately 860 µm for a desired *FSR* of 100 GHz. Additionally, titanium heaters with a thickness of 100 nm are placed next to them to allow for phase tuning. To prevent crosstalk between applied phase shifts on adjacent delay lines, 10 µm deep trenches have been etched using Inductively Coupled Plasma (ICP) etching. As already been demonstrated in [8], 4 × 4 MMI coupler with less than 5° phase error and less than 0.5 dB imbalances between the coupling coefficients have been realized using this SOI platform.

The ideal coupling matrix for the implemented MMI devices is

$$\left|\underline{H}_{coupler}\right| = \begin{bmatrix} 0.5 & 0.5 & 0.5 & 0.5 \\ 0.5 & 0.5 & 0.5 & 0.5 \\ 0.5 & 0.5 & 0.5 & 0.5 \\ 0.5 & 0.5 & 0.5 & 0.5 \end{bmatrix} \qquad (6)$$

$$\Phi(\underline{H}_{coupler}) = \begin{bmatrix} 0 & {}^{3}\!/_{4} & -{}^{1}\!/_{4} & 0 \\ {}^{3}\!/_{4} & 0 & 0 & -{}^{1}\!/_{4} \\ -{}^{1}\!/_{4} & 0 & 0 & {}^{3}\!/_{4} \\ 0 & -{}^{1}\!/_{4} & {}^{3}\!/_{4} & 0 \end{bmatrix} \cdot \pi \quad . \qquad (7)$$

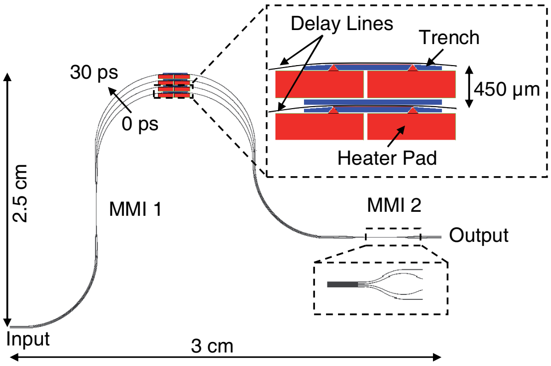

Fig. 8. Layout of the realized first stage. Zoomed layout of the delay lines with heaters, trenches and MMI coupler are shown.

3.2. Comparison of Simulation Model and Measurement

Without applying power to the heaters, we have first measured the transfer function and group delay response for input port 1 and output port 1 by using the modulation phase shift (MPS) technique. Since birefringence tuning has not been carried out while designing this device, we've measured the filter response for one polarization only. This birefringence, caused by the difference in the modal index for TE and TM polarization, can be reduced by using the technique mentioned in [4]. The comparison between measured and simulated responses for transmission and group delay can be seen in Fig. 9 and Fig. 10. By estimating the initial value of the phase shifters, changing the simulated *FSR* to a slightly smaller value of 96.6 GHz and taking low imbalances in the intensity and errors in the phase relations at the output of the MMI couplers and delay lines into account, one is able to get a good matching. Due to limited sensitivity of the measurement system, the phase information in the regions of minimum transmission is not completely extracted. As a consequence, the group delay peaks are decreased in quality.

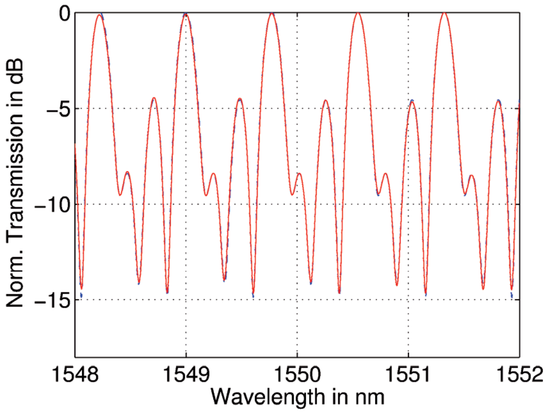

Fig. 9. Comparison between measured (solid curve) and simulated (dashed curve) transfer function. Curves are nearly identical.

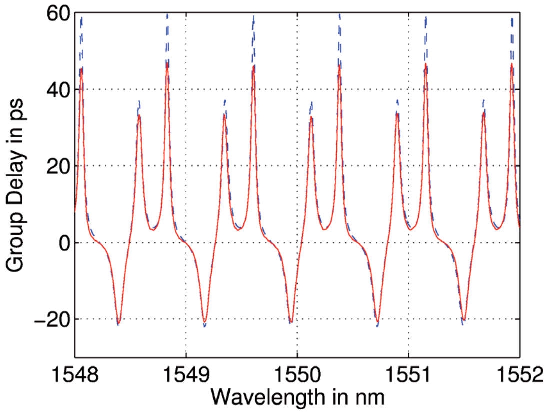

Fig. 10. Comparison between measured (solid curve) and simulated (dashed curve) group delay function. Curves are nearly identical.

3.3. Filter Tuning

By applying electrical power only to the heater pad next to the longest delay line, we change the phase of the light passing this part of the filter and observe the change in transmission and group delay. Likewise, we simulate a phase change on delay line $3T$ in our simulation model. The comparison between measured and simulated response to this tuning is shown in Fig. 11 and Fig. 12. The relationship between applied power and the estimated phase shift is summarized in Fig. 13. Except for the mentioned problem in determining the group delay value at wavelengths of minimum transmission, the comparison in transmission as well as in group delay response shows a good agreement. This emphasizes the low crosstalk between the controlled delay line and the adjacent waveguide. This fact proofs that the phase on the delay lines can be controlled independently with negligible crosstalk. This characteristic allows us to set phase relations as desired to tune the serial-parallel filter to different dispersion compensating states.

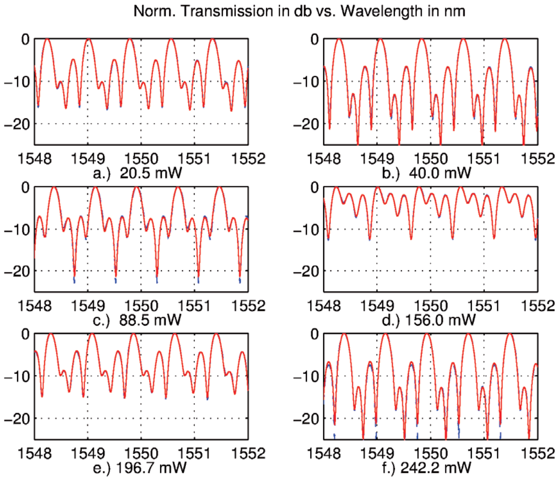

Fig. 11. Comparison between measured (solid) and simulated (dashed) transmission response for different applied phase shifts on longest delay line.

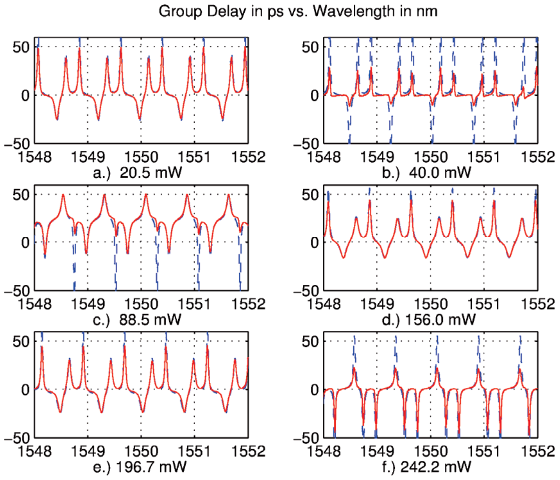

Fig. 12. Comparison between measured (solid) and simulated (dashed) group delay for different applied phase shifts on longest delay line.

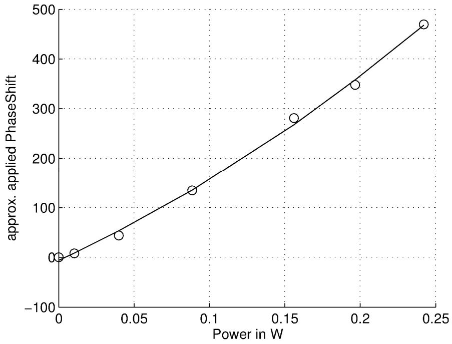

Fig. 13. Approx. Phase Shift on longest delay line vs. Power applied to the heater.

4. CONCLUSION

A compact and flexible serial-parallel delay line filter consisting of 4 × 4 MMI couplers and phase tuning elements has been presented. We have shown that the proposed flexible architecture has the potential to be used as an equalizer for compensating residual dispersion in WDM systems with symbol rates up to 50 Gbit/s and above.

First realizations in silicon photonics are carried out. The good agreement between the simulated and measured filter response for different tuning cases shows the flexible tuning ability in the presented planar technology.

ACKNOWLEDGMENT

The financial support of German Research Foundation (DFG) in the frame of this project is gratefully acknowledged. The authors thank Mrs. E. Brose, Mrs. B. Kranzusch and M. Gruse for sample preparations.

REFERENCES

[1] C. Gunn, "CMOS Photonics^{TM} – SOI Learns a New Trick," IEEE International SOI Conference, 2005, pp. 7-9.

[2] K. Maru, T. Mizumoto, and H. Uetsuka, "Demonstration of Flat-Passband Multi/Demultiplexer Using Multi-Input Arrayed Waveguide Grating Combined With Cascaded Mach–Zehnder Interferometers," Journal of Lightwave Technology, 2007, pp. 2187-2197.

[3] K. Hattori, M. Fukui, M. Jinno, M. Oguma, and K. Oguchi, "PLL-Based Optical Add/Drop Switch with Automatic Level Control," Journal of Lightwave Technology, 1999, pp. 2562-2571.

[4] K. Voigt, L. Zimmermann, G. Winzer, T. Mitze, J. Bruns, K. Petermann, B. Hüttl, and Colja Schubert, "Performance of 40-Gb/s DPSK Demodulator in SOI-Technology," IEEE Photonics Technology Letters, 2008, pp. 614-616.

[5] J. Niehusmann, A. Voerckel, and P. H. Bolivar, "Ultrahigh-quality-factor silicon-on-insulator microring resonator," Optics Letters, 2004, 2861-2863.

[6] D. M. Marom, C. R. Doerr, M. A. Cappuzzo, E. Y. Chen, A. Wong-Foy, L. T. Gomez, and S. Chandrasekhar, "Compact Colorless Tunable Dispersion Compensator With 1000-ps/nm Tuning Range for 40-Gb/s Data Rates," Journal of Lightwave Technology, 2006, pp. 237-241.

[7] N. Neumann, T. Duthel, M. Haas, and C. G. Schäffer, "General Design Rules fort he Synthesis of Dispersion and Dispersion Slope Compensation FIR and IIR Filters With Reduced Complexity," Journal of Lightwave Technology, 2007, pp. 3555-3562.

[8] K. Voigt, L. Zimmermann, G. Winzer, and K. Petermann, "SOI based 2×2 and 4×4 waveguide couplers – Evolution from DPSK to DQPSK," Proc. Group IV Photonics, 2008, pp. 209-211.

Stefan Schwarz received the Dipl.-Ing. degree in electrical engineering from Hamburg University of Technology, Germany, in 2009. He is currently working towards the Ph.D. degree at the Department of High-Frequency Engineering and Optoelectronics at the University of Armed Forces, Germany.

His current research interests include dispersion compensation and photonic lightwave circuits.

Abdul Rahim received his bachelor's degree in Electrical Engineering from University of Engineering and Technology, Lahore (Pakistan) in 2002. From 2003 to 2006, He was working on the development of Optical Telemetry Systems with Marine Services Limited, Islamabad. In 2006, he got Erasmus Mundus Scholarship from European Union to complete his masters in Photonics from Royal Institute of Technology (KTH) Sweden and University of Gent (Belgium). Since 2009, he is working towards the Ph.D. degree from Institute of High Frequency Technology at University of Technology in Berlin.

Jürgen Bruns (M'04) received the Dipl.-Ing. and Dr.-Ing. degrees from the Technische Universität Berlin, Germany, in 1988 and 1992, respectively, both in electrical engineering.

From 1989 to 1993, he was a Research Associate at the Institut für Werkstoffe der Elektrotechnik, Technische Universität Berlin, where he was engaged in research on solar cells based on amorphous silicon. From 1994 to 1999, he was at the Hahn-Meitner-Institut, Berlin, developing a manufacturing technology for thin-film solar cells. From 1999 to 2000, he was a Senior Research Scientist with Energy Photovoltaics, Inc., Princeton, NJ. Since 2000, he has been the Head of Technology, Faculty of Electrical Engineering, Technische Universität Berlin. His current research interests include silicon-based integrated optics and thin-film solar cells.

Christian G. Schäffer (M'88) received the Dipl.-Ing. and Dr.-Ing. degrees from the Technical University of Berlin, Germany, in 1984 and 1989, respectively.

From 1988 to 1992, he was with the R&D Center, Department of Telecommunication, DASA, where he conducted research in coherent optical generation of microwave signals and optical interconnects for phased array antennas. In 1992, he joined the Fachhochschule Lübeck, Germany, as a Professor in electrical engineering. From 1999 to 2009, he was a Full Professor of radio frequency and photonics with the Communications Laboratory, Department of Electrical Engineering, Dresden University of Technology, Germany.

He joined the Department of High-Frequency Engineering and Optoelectronics at the University of Armed Forces, Germany, in 2009, where he is at present an Institute Professor His current research interests include microwave photonics, optical frequency synthesis, fiber Bragg gratings, dispersion compensation, performance monitoring and wavelength-division-multiplexing networks.

Klaus Petermann received the Dipl.-Ing. and Dr.-Ing. degrees from the Technische Universität Braunschweig, Germany, in 1974 and 1976, respectively, both in electrical engineering.

From 1974 to 1976, he was a Research Associate at the Institut für Hochfrequenztechnik, Technische Universität Braunschweig, where he was engaged in research on optical waveguide theory. From 1977 to 1983, he was with AEG Telefunken, Forschungsinstitut Ulm, Germany, where he was engaged in research on semiconductor lasers, optical fibers, and optical fiber sensors. From 1983 to 2004, he was a Full Professor at the Technische Universität Berlin, Germany, where, since 2004, he has been a Vice-President for Research. His current research interests include optical fiber communications and integrated optics.

Dr. Petermann is a member of the Senate of the Deutsche Forschungsgemeinschaft and of the Berlin–Brandenburg Academy of Science. He was a Member of the Board of the Verein Deutscher Elektrotechniker from 1996 to 2004. He has served as an Associate Editor of the IEEE PHOTONICS TECHNOLOGY LETTERS during 1999–2004. He was the recipient of the 1993 Leibniz Award from the "Deutsche Forschungsgemeinschaft" and the 1999/2000 "Distinguished Lecturer" Award from the IEEE Lasers and Electro-Optics Society.

Integration of novel lattice-matched Ga(NAsP) laser material on (001) Si for optoelectronic and photonic applications

Bernardette Kunert*, Kerstin Volz** & Wolfgang Stolz**

**) NAsP III/V GmbH, Am Knechtacker 19, 35041 Marburg, Germany,*
***) Material Sciences Center and Faculty of Physics, Philipps-University Marburg,*
Hans-Meerwein-Strasse, 35032 Marburg, Germany

The enormous development of Silicon (Si) based micro- and nano-electronic integrated circuits (ICs) is based on the downscaling of electronic semiconductor devices. This driving force, however, is approaching fundamental limitations and therefore new technologies are necessary to guarantee future progress in IC functionalities. Hence, the integration of III/V on Si microelectronics and ICs has moved back into focus of research activities, because the combination of the advantageous material properties of both semiconductor classes will open up completely new device architectures and functionalities. In particular, the optoelectronic properties of III/V materials are very important in the field of Si-Photonics. A sophisticated III/V-laser source integrated on Si microelectronics allows for chip-to-chip or even on-chip optical data transfer with all of the advantages of high bandwidth optical data communications, leading to a new IC technology. In this communication, we introduce the novel Ga(NAsP)/GaP-based laser material, which can be monolithically integrated lattice-matched on (001) Si-substrate, and present and discuss its application potential for the monolithic integrated lasers in the data com wavelength range around 850 nm to 960 nm.

The monolithic integration of well established III/V laser materials such as alloys of GaAs and InP is accomplished by the formation of a high density of threading dislocations in the III/V layers, which hinders the realization of highly reliable and long lifetime laser devices. This presence of threading dislocations is due to the differences in lattice spacing of GaAs and InP in comparison to Silicon. Although GaP is an indirect semiconductor underlying the same optoelectronic limitations as Si, the lattice-matched condition to Si brings in significant advantages. For example, the monolithic nucleation of III/V materials on Si substrate is much easier for GaP due to the absence of misfit and threading dislocations in thin layers. In addition, the GaP based dilute nitride Ga(NAsP) material system has been specifically developed for the lattice-matched integration of a direct band gap material. This novel materials system allows for the deposition of complete III/V laser diode lattice-matched to Si (001) substrate.

After an introduction to the active material system Ga(NAsP) the focus of this presentation is the monolithic integration scenario of Ga(NAsP) based laser diode on exactly oriented (001) Si substrate applying metal organic vapor phase epitaxy (MOVPE). Growth conditions will be discussed in line with structural as well as optical properties of deposited multi-quantum-well heterostructures and laser structures. Laser operation at low temperatures of these III/V devices grown lattice matched to Si substrate has been demonstrated for the first time. Whereas these first device structures have been growth on 2” Si (001) wafer in a horizontal MOVPE reactor, the current research activities concentrate on the process transfer to 300 mm Si wafers in epitaxy production machine. The challenges and opportunities of growing GaP based materials on 300 mm substrates in a Close-Couple-Showerhead cluster tool will be discussed in particular in view of optimal CMOS process compatibility.

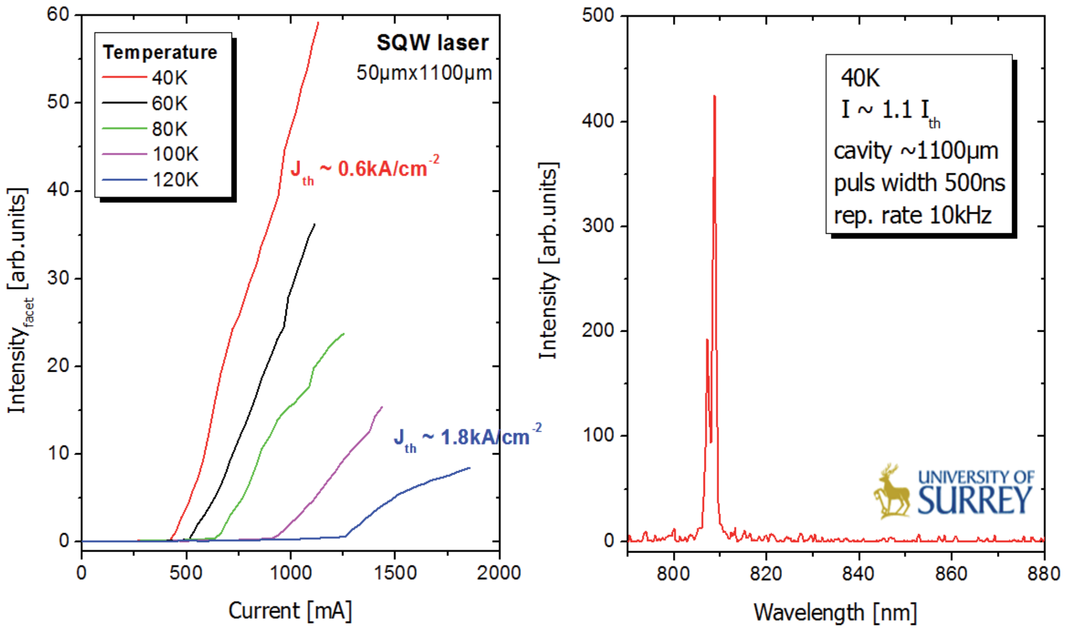

Figure 1: Facet intensity versus current of a Ga(NAsP) single quantum well laser grown on Si substrate (right). Corresponding laser spectrum above threshold (left). The laser diodes have been grown in Marburg whereas the measurement has been carried out at the University of Surrey (Nadir Hossain, Stephen J. Sweeney).

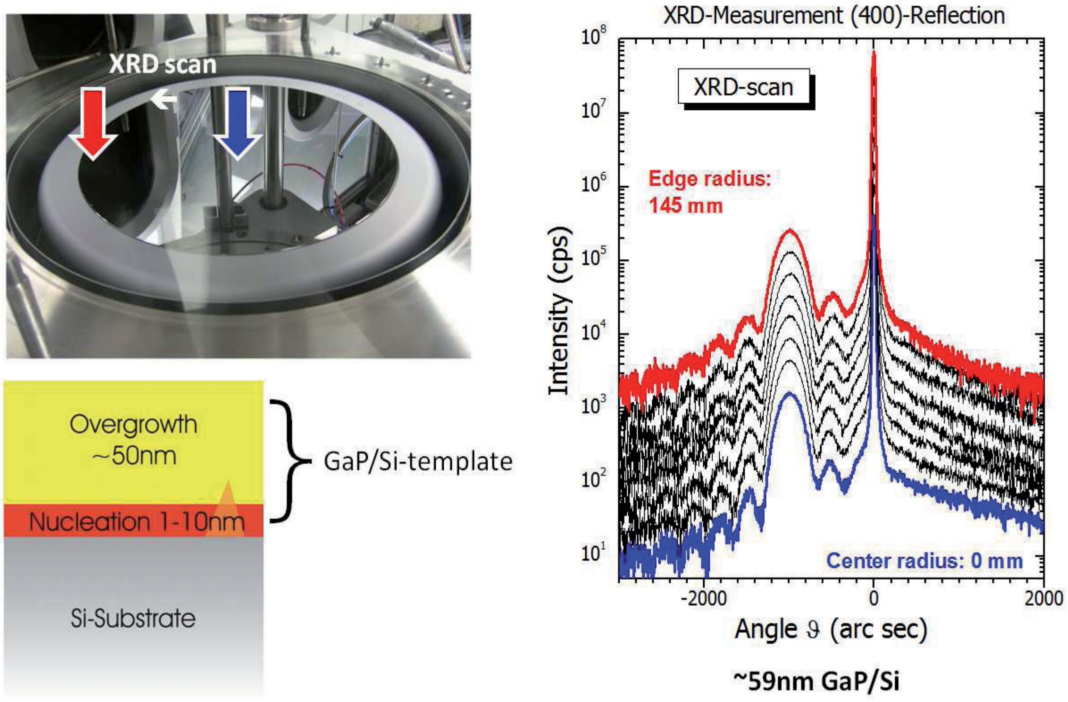

Figure 2: 60 nm GaP grown on 300 mm Silicon wafer in a Close-Coupled Shower head reactor. Picture of the susceptor with a 300 mm Si wafer (top). Sketch of the GaP/Si-template (bottom). XRD scans from wafer center (blue) to the edge (red)(right).

Silicon photonic components for a novel interferometric biosensor array concept

Muellner, P.; Bruck, R.; Hainberger, R.; Karl M.; Baus, M.; and Wahlbrink, T.

Abstract—In this work, we present a novel wavelength multiplexing concept for an integrated sensor array employing SOI photonic Mach-Zehnder interferometers as sensing element. The characteristics of the entire device are discussed and the design performed with FEM and 3D-FDTD as well as the measurements of the nanophotonic key components – micro ring resonators and photonic wire Bragg gratings – are presented.

Index Terms—*silicon photonics, SOI, sensor array, bragg grating, micro ring resonator*

1. *Introduction*

The advances in the field of integrated photonic devices during the past decades have been primarily spurred by telecom needs. Recently, also other applications, *e.g.* in the field of life sciences, have become driving factors.

In particular integrated silicon photonic Mach-Zehnder evanescent wave sensors (MZI) for the detection of biomolecules have attracted attention due to their potential for a high level of integration [1]. In an integrated MZI the light is split into two waveguiding arms - a reference and a measurement arm. The evanescent field of the guided mode in the measurement arm is influenced by refractive index changes induced for example by selective biochemical binding events on the functionalized surface. Consequently, at the MZI output, where the sensing and the reference arm are recombined, interference occurs due to the relative phase shift caused by the refractive index change. The interference translates this phase shift into a modulation of the optical power. The high sensitivity of such devices arises from the large ratio between waveguide length (~1 cm) and wavelength (~1.3~1.5 µm).

The integration of an MZI sensor array for multi-parameter analysis on a single chip necessitates an effortless way for coupling light into and out of the sensor device and for distributing it to the individual MZIs.

2. *Concept*

One option to realize an effortless access to an integrated sensor array is to use wavelength multiplexing. TM polarized light of a wavelength tunable laser source is coupled into a single bus waveguide by means of a grating coupler. Efficient silicon-on-insulator (SOI) grating couplers can be realized with < 1 dB wavelength dependent excess loss over a wavelength range of 35 nm [2]. The grating coupler is followed by a taper, which reduces the waveguide width gradually from approximately 10 µm of the grating to the width of the single mode waveguide with w=500 nm.

Micro ring resonators act as wavelength routing elements that guide the light to the individual sensing elements. The radii of the ring resonators differ slightly to obtain resonance wavelengths that are allocated equally within the free spectral range. In order to recombine the different wavelength channels after passing through the sensing elements the multiplexing components should have the identical spectral characteristic as the demultiplexing components. In particular for micro ring resonators, this represents a challenging task because even very small deviations in the fabrication process easily result in a wavelength shift of the order of the resonance width.

In order to overcome this problem, we propose the use of photonic wire Bragg gratings to reflect the light back to the same micro ring resonator that dropped the light from the input waveguide. This approach completely eliminates the risk of a wavelength mismatch between drop and add port and offers also the advantage that the light can be coupled into and out of the chip via the same grating, which reduces the alignment effort. A fiber optic circulator put between laser source and grating coupler separates input and output light paths. By terminating each arm of the MZI separately with a Bragg reflector (see Fig. 1a)) the light path through the MZI and thus the sensor response are doubled.

Manuscript received March 31, 2011.

This work was supported by the Austrian NANO Initiative under the grant PLATON Si-N (project no. 819655).

The authors P. Muellner, R. Bruck and R. Hainberger are with the Health & Environment department, business unit Nano Systems of the Austrian Institute of Technology GmbH, Donaucitystr. 1, 1220 Vienna, Austria.

The authors M. Karl, M. Baus and T. Wahlbrink are with the AMO GmbH, Aachen, Germany.

email: paul.muellner@ait.ac.at

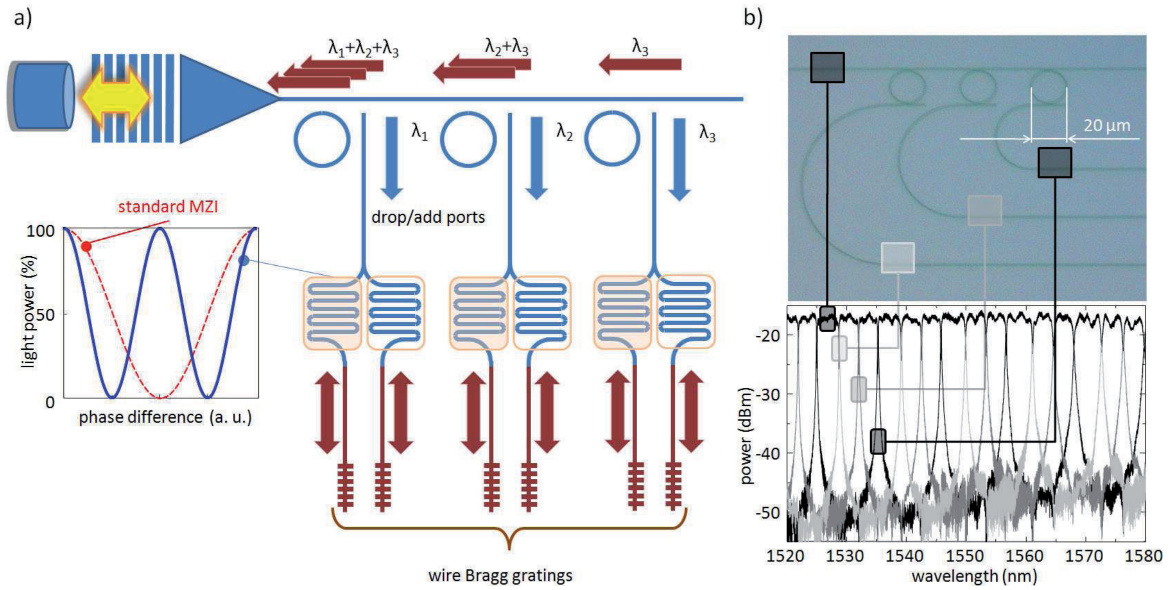

Figure 1: a) Wavelength multiplexing concept with one ring resonator per channel employing wire Bragg grating reflectors; b) LM-micrograph and transmission spectra of a multiplexing array with three ring resonators designed for propagation losses in the ring of 6 dB/cm.

3. DESIGN AND EXPERIMENTAL RESULTS OF THE PHOTONICS KEY COMPONENTS

This concept requires the careful design of two key components: 1) the micro ring resonators and 2) the wire Bragg gratings. In the following, the design and the experimental verification of these structures will be discussed. For both cases, the cross section of the wire waveguides was set to a width of w=500 nm and a height of h=220 nm.

3.1 Micro ring resonators

In order to obtain micro ring resonators with resonance wavelengths equally allocated within the free spectral range, the proper radii have to be determined. For this purpose, first the effective index of the ring was calculated using a 2D full vectorial FEM eigenmode solver [3]. Starting with a ring radius of 10 µm and requiring an equally spaced allocation of the resonance wavelengths of the three resonators within the free spectral range of ~10 nm, the resulting difference in the radii of the other rings amount to Δr=45 nm, which can be calculated from the length of the ring and its effective index.

Next, the spacing between the rings and the bus waveguide was determined by calculating the coupling coefficient from the electrical field distribution [4] employing FEM. The coupling coefficient has to be matched to the losses which occur during propagation in the ring. Three different loss values, 3, 6 and 15 dB/cm were assumed for the propagation in the ring. The corresponding optimum separations between the bus waveguide and the ring of 1220, 1160 and 1055 nm were determined.

On the basis of this design, samples were realized. The photonic structures were written into e-beam resist covering the 220 nm thick silicon device layer of SOI wafers with a buried oxide thickness of 3 µm using a Leica EBPG 5000 e-beam lithography system. After e-beam exposure and resist development the samples were reactive ion etched (RIE) with bromine based chemistry. Finally, an SU-8 cladding was spin-coated on the sample and UV cured.

The optical characterization of the three ring resonators was performed in a fiber end-face coupling configuration employing a tunable laser source. The top LM-micrograph in Fig. 1 b) shows three ring resonators supplied by a single bus waveguide. The transmission spectrum of the bus

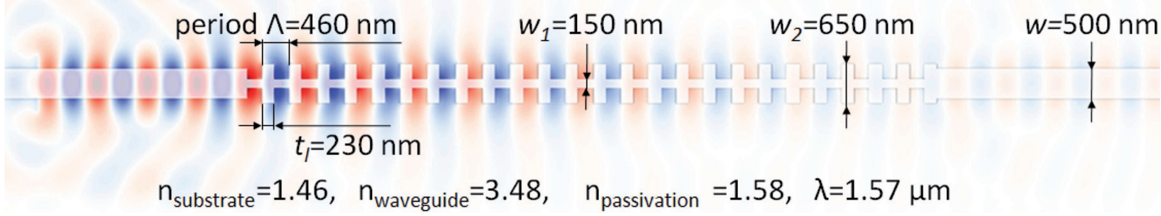

Figure 2: 3D FDTD simulation result of a 220 nm thick photonic wire Bragg grating with quasi-TM polarized CW excitation at λ=1.57µm. The transversal electric field component is shown and all important geometry parameter are introduced.

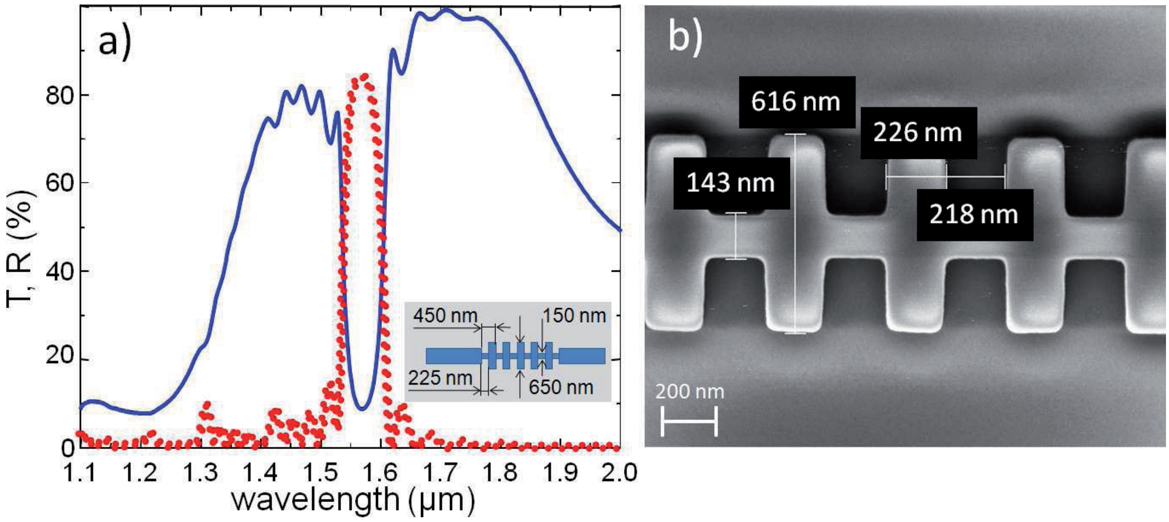

Figure 3: a) 3D FDTD simulation results of the wire Bragg grating geometry depicted in Fig. 2. For this structure a reflectivity of more than 80% is achieved while the transmissivity amounts to ~10%. b) SEM picture of the wire Bragg grating with measured geometry parameters.

and the three drop ports was measured and as the bottom graph in Fig. 1 b) shows, the desired equally spaced wavelength allocation within the free spectral range was obtained. Moreover, the small differences between drop port peaks and the bus waveguide transmission level indicate that the losses caused by the multiplexing were low for the micro ring resonators designed for losses in the ring of 6 and 15 dB/cm.

3.2 Wire Bragg grating

The second key element is the photonic wire Bragg grating. Photonic wire Bragg gratings are highly attractive because they can act as compact integrated reflectors (length ~10 μm) in a waveguide circuit. In-depth studies by Gnan *et al.* [5], [6] demonstrated that for the quasi-TE polarization photonic wire Bragg gratings can fulfill the requirement of a band gap over a wavelength range of several tens of nanometers. However, for applications such as evanescent field sensing employing, *e.g.* integrated interferometers or micro-ring resonators the quasi-TM mode of a silicon photonic wire shows an approximately twice as high sensitivity as the quasi-TE mode [7, 8]. Therefore, wire Bragg gratings have to be optimized with respect to their reflection characteristic for the quasi-TM polarization.

3.3.1 Simulation

The design of 3D waveguide structures with analytical and 2D numerical approximations allows only for a qualitative layout. In order to obtain more reliable results, rigorous 3D FDTD simulations are indispensible. We performed simulations for different sets of geometry parameters (w_1, w_2 and Λ, see Fig. 2) using the GNU package MEEP [9]. The thickness of the silicon photonic wire was set to 220 nm, which is the standard device layer thickness of commercially available SOI wafers for photonic applications.

Apart from the geometry, Fig. 2 also shows the transversal electric field component for CW excitation with quasi-TM polarized light at a wavelength of 1.57 μm for a structure with an outer Bragg grating width of w_2=650 nm. The low field amplitude at the output on the right hand side indicates the existence of a band gap. Due to the comparatively wide wavelength range that has to be considered, material dispersion has to be taken into account. The refractive index values of silicon and silica were taken from Palik [10] and that of SU-8 from Borreman *et al.* [11]. Our studies revealed that the structure shown in Fig. 2 with a width of w_2=650 nm in the grating region exceeding the width of the wire of w=500 nm shows a peak reflectivity of 85% and a transmissivity of about 10% (see Fig. 3a). Scattering losses amount to about 5%. The reflectivity exceeds 70% over a wavelength range of 50 nm.

3.3.2 Fabrication & Characterization

According samples were again realized by means of e-beam lithography and reactive ion etching (RIE) with bromine based chemistry. All wire Bragg gratings were covered with SU-8. Scanning electron microscope (SEM) pictures of an uncoated sample (see Fig. 2b) confirm the high quality of the fabricated wire Bragg grating structures. Except for the outer width w_2 of the fabricated structure, which differs by 34 nm, the deviations of the fabricated structure from the design parameters is comparatively low.

For the optical characterization a tunable laser source covering the wavelength range from 1460 nm to 1640 nm was used. The laser light was coupled into the waveguide via end face coupling using a polarization maintaining tapered fiber. At the output of the device the light was coupled into a tapered single mode fiber and guided to an optical power meter. In order to avoid strong back

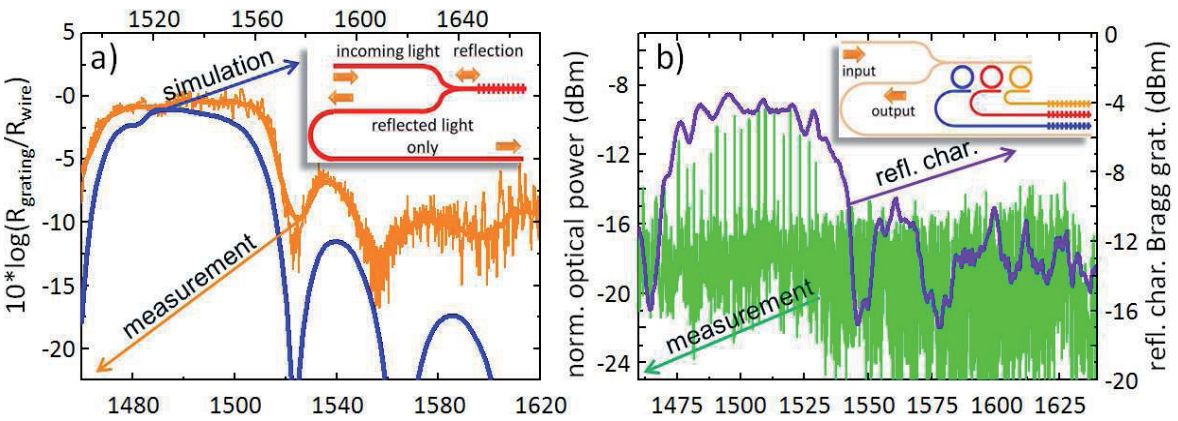

Figure 4: a) Comparison of the simulation results with the corresponding reflection measurement for the structure shown in Fig. 3b). The Y-branch shown in the inset separates the outgoing from the incoming light. b) Transmission characteristic of a ring resonator based device as shown in the inset and reflection characteristic of the wire Bragg grating. At the output, resonances of the resonances are only observed in the wavelength range where the wire Bragg grating is highly reflective.

reflections arising from the input fiber/air and air/waveguide interfaces, the back reflected light from the Bragg grating was separated from the incoming light on-chip using a reversed Y-branch (see the inset of Fig. 4a)). Since the light passed through the Y-branch twice it suffered 6 dB loss.

Figure 4b) plots the measurement result of the reflectivity. In order to enable a direct comparison with the 3D FDTD simulations the transmission of a straight wire waveguide without a grating was used as reference to normalize the output power of the experiments. Furthermore, the 6 dB losses due to the Y-Branch were added to the measured power values. The grating shows a peak/dip of approximately 10 dB suggesting that the grating operates as predicted by our numerical results. Moreover, the shape of the measured reflection spectrum is in good agreement with the simulation. Nevertheless, from Fig. 4a) it becomes apparent that the measured reflection spectrum shows a blue-shift with respect to the simulated spectrum. This difference can most likely be attributed to the deviations of the fabricated structure from the design (including the side wall angle) as well as to the refractive index value and its wavelength dependence of the SU-8, which may not be identical to the assumed values in the design process.

However, the performance of the wire Bragg grating was sufficient to for preliminary tests of an on-chip wavelength multiplexing scheme for refractometric sensor arrays, which combines Bragg reflectors with ring resonators. Figure 4b) shows a set of three ring resonator with different radii of 10.00 µm, 10.045 µm and 10.09 µm in order to obtain again equally spaced resonances as described in section 3.1. A wire Bragg grating with the design of Fig. 3b) was implemented in the drop port of each ring resonator as shown in the inset of Fig. 4b). The reflected light passes the ring resonator a second time and is separated from the incoming light again via a reversed Y-branch. The transmission characteristic of the device shows the expected behavior (see Fig. 4b). At the output port of the device, the resonances of the ring resonators can only be observed within the wavelength range where the wire Bragg grating is highly reflective. This is confirmed by comparison with the Bragg grating reflection characteristic (purple line in Fig. 4b).

4. CONCLUSION

In this work, a wire Bragg grating structure covered with SU-8 and operated with quasi-TM polarized light was designed with respect to maximum reflectivity employing rigorous 3D FDTD simulations at a wavelength of 1550 nm. The numerical results demonstrated that a reflectivity of more than 80% is feasible for a structure, where the outer width of the grating modulation exceeds the width of the waveguide.

Samples were fabricated with e-beam lithography and characterized employing an on-chip Y-branch configuration to separate the reflected and the incoming light. The optical characterization revealed a good agreement of simulated and measured reflectivity spectra demonstrating the high quality of the design and fabrication process. By combining this wire Bragg grating with ring resonators, we practically demonstrate the applicability of such structure as integrated reflector in waveguide circuits.

From these experimental results it can be concluded that the proposed concept is feasible in practice.

REFERENCES

[1] Fan, X., White, I., Shopova S., Zhu, H., Suter, J., Sun, Y., “Sensitive optical biosensors for unlabeled targets: A review,” *Elsevier*, Analytica Chimica Acta, 2008, pp. 8-26.

[2] Taillaert, D., Bienstman, P., Beats, R., „Compact efficient broadband grating coupler for silicon-on-insulator,“ *The Optical Society*, Optics Letters, 2004, pp. 2749-2751.

[3] Femlab 3.1.0.163, *Comsol*, Berliner Str. 4, 37073 Goettingen, Germany.

[4] Snyder, A. W., Ankiewicz, A., Altintas A., „Fundamental error of recent coupled mode formulations,“ *IEEE*, Electronics Letters, 1987, pp. 1097-1098.

[5] Gnan, M., Bellanca G., Chong, H. M. H., Bassi, P., Rue, R. M. D. L., "Modelling of photonic wire bragg gratings," *Springer*, Optical and Quantum Electronics 2006, pp. 133-148.

[6] Gnan, M., Hopman, C. L., Bellanca, G., Ridder, R. M. D., Rue, R. M. D. L., Bassi, P., *The Optical Society*, Optics Express, "Closure of the stop-band in photonic wire bragg gratings," 2009, pp.8830-8842.

[7] Densmore A., Vachon, M., Xu, D. X., Janz, S., Ma, R., Li, Y. H., Lopinski, G., Delage, A., Lapoint J., Luebbert, C. C., Liu, Q. Y., Cheben P., Schmid H. J., "Silicon photonic wire biosensor array for multiplexed real-time and label-free molecular detection," *The Optical Society*, Optics Letters, 2009, pp. 3598-3600.

[8] Muellner, P., Bruck, R., Hainberger, R., Karl, M., Baus, M., Wahlbrink, T., „Silicon nanophotonic components for an integrated refractometric sensor array," *Elsevier*, Eurosensors XXIV, 2010, pp. 1300-1303.

[9] Oskooi, A. F., Roundy D., Ibanescu M., Bermel, P. Joannopoulos J., Johnson S. G., "MEEP: A flexible free-software package for electromagnetic simulations by the FDTD method," *Elsevier*, Computer Physics Communications, 2010, pp. 687-702.

[10] Palik, E. D., ed., "Handbook of optical constants of solids", *Academic Press*, 1985.

[11] Borreman, A., Musa, S., Kok, A., Diemeer, M. B. J., Driessen, A., „Fabrication of polymeric multi-mode waveguides and devices in SU-8 photoresist using selective polymerization," *IEEE*, LEOS Benelux, 2002, pp.83-86.

Integrated Bragg Gratings on SOI Rib Waveguides for Dispersion Compensation

Giuntoni, Ivano; Gajda, Andrzej; Krause, Michael; Stolarek, David; Steingrüber, Ralf;
Bruns, Jürgen; Zimmermann, Lars; Brinkmeyer, Ernst; Tillack, Bernd and Petermann, Klaus.

Abstract—*We present the design, fabrication and characterization of Bragg gratings on silicon-on-insulator rib waveguides. Using a rigorous bidirectional eigenmode expansion numerical simulations were performed to define a set of geometrical parameters which fulfil the requirements of high reflectivity, narrow bandwidth and low loss. The designed devices were subsequently fabricated with a double lithographic process. A first prototyping was performed combining electron-beam lithography and photolithography, afterwards the fabrication was repeated with a state of the art BiCMOS technology based on Deep-UV (DUV) lithography, which would allow an easier integration in standard fabrication processes. Bragg gratings exhibiting a reflectivity larger than 80% over a bandwidth of 0.8 nm and an insertion loss of 0.5 dB are shown. The possibility to apply a chirp to the gratings via waveguide tapering is also presented, proving that a dispersion of 250 ps/nm can be compensated*

Index Terms—*Bragg scattering, gratings, rib waveguides, silicon-on-insulator technology, dispersion compensation.*

1. *INTRODUCTION*

BRAGG ratings established in the last years as an important waveguide component for achieving wavelength selective filter functions. Fiber based Bragg grating structures can be considered state of the art for applications in the optical communications and for sensing. The reliable integration of such a component on the silicon-on-insulator (SOI) platform is hence an important step for the further development of silicon-based integrated systems for wavelength selection and dispersion compensation. However, the transition from silica based Bragg gratings to silicon waveguide gratings is less obvious than it seems.

Different approaches were presented for the realization of Bragg gratings on waveguides. The modulation of the core refractive index was achieved with ion implantation [1] or with a periodic corrugation of the waveguide, either on the waveguide sidewalls [2] or on the top surface [3-6]. Both approaches lead to comparable results, even though the latter alternative can be implemented with a less expensive and simpler technology.

In this paper we present a robust integration of Bragg gratings comprising top corrugated SOI rib waveguides. A reliable modeling method for numerical simulations was used to provide a design rule, while two different fabrication processes were optimized to deliver usable devices. Finally a proper chirp was applied to the designed gratings to be able to compensate the chromatic dispersion.

We make use of rib waveguides with a rib height of $t = 1.5\,\mu m$. They exhibit lower propagation losses and easier fabrication processes compared to photonic wires, and still permit a relatively high integration level.

2. *PRINCIPLE AND DESIGN*

A useful wavelength-selective reflector which should act as a filter is expected to fulfill the following requirements. First, at a desired wavelength the largest possible amount of optical power should be back-reflected. At the same time, every wave propagating at a different wavelength should be transmitted with the lowest possible loss. Furthermore, the reflectivity bandwidth should be kept as narrow as possible, corresponding to a high selectivity.

The numerical description of waveguide Bragg gratings is not a trivial task due to the involvement of higher order modes in both propagation directions. We chose a bidirectional mode expansion (BEP) which combines a high reliability with a relatively low computation complexity if a sufficient number of modes is considered [7].

Two-dimensional simulations of Bragg gratings were performed, i.e. the grating was assumed to be on top of a laterally infinite slab waveguide instead of the laterally finite rib waveguide shown in Fig. 1. We systematically analyzed how the geometrical parameters of the grating influence the fulfillment of the cited conditions [8].

Manuscript received April 6, 2011.

This work was financially supported by the German Research Foundation (DFG) in the frame of grant FOR653.

I. Giuntoni, A. Gajda, J. Bruns, L. Zimmermann, B. Tillack and K. Petermann are with the Technische Universität Berlin, Fachgebiet Hochfrequenztechnik (HFT 4), 10587 Berlin, Germany, e-mail: ivano.giuntoni@tu-berlin.de.

M. Krause and E. Brinkmeyer are with the Technische Universität Hamburg-Harburg, Optische Kommunikationstechnik (OKT), 21073 Hamburg, Germany.

D. Stolarek, L. Zimmermann and B. Tillack are with IHP GmbH, 15236 Frankfurt (Oder), Germany.

R. Steingrüber is with Fraunhofer-Institut für Nachrichtentechnik, Heinrich-Hertz-Institut, 10587 Berlin, Germany).

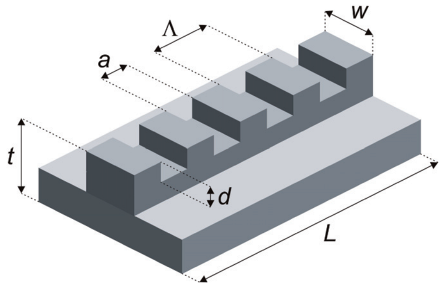

Fig. 1. Geometrical parameters of a silicon-on-insulator rib waveguide Bragg grating: *L* overall length, *d* grating depth, *a* grating trench, Λ grating period, *w* waveguide width, *t* rib height, *h* rib etching depth.

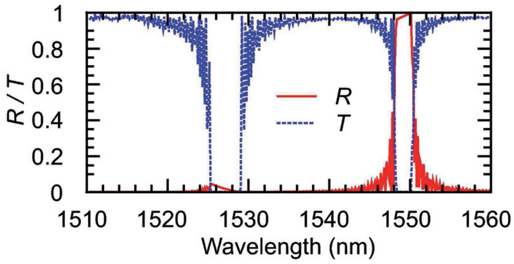

Fig. 2. Calculated reflectivity *R* and transmissivity *T* spectra of a Bragg reflector with $d = 150$ nm, $D = 0.3$ and $L = 800$ µm. The grating period is $\Lambda = 225$ nm.

This was accomplished associating the fundamental mode of the slab waveguide with the guided mode of the rib waveguide. All the energy which is coupled (reflected or transmitted) into other modes in the slab-waveguide grating was then considered as loss in the rib-waveguide structure.

It was observed [8] that the best performances can be achieved with gratings exhibiting narrow and shallow etched trenches, i.e. with $d < 150$ nm and $0.1 < D < 0.4$. Fig. 2 shows the simulated spectra of a Bragg reflector in a SOI waveguide that is 800 µm long, 150 nm deep and has a duty cycle of 0.3. At the wavelength 1550 nm a reflectivity of more than 99% is expected, the losses are kept under 0.15 dB outside the reflection bandwidth, which is 2.1 nm broad. At shorter wavelengths around $\lambda = 1525$ nm a sudden drop in the transmission curve occurs, this corresponds to a strong coupling to a backward higher order mode.

3. *FABRICATION*

A double lithographic process was used for the device fabrication. A first lithography for the patterning of the gratings on the plain SOI wafer and a second one afterwards for the definition of the waveguides.

Two different kind of lithographic techniques were tested for the grating realization. A first prototyping was performed combining electron-beam (EB) lithography for the grating patterning and photolithography for the waveguides [6]. This method allows a high flexibility and the opportunity of testing different geometries, because of its high resolution, which is however limited within a writing field (usually less than 1 mm^2). Writing fields can be stitched together to achieve larger structures, but only at the price of additional stitching errors. The speed of high precision EB writing also renders the technique incompatible with wafer level processing. Therefore the optimal geometry was realized in a second step using Deep-UV 248 nm lithography (DUV) [9]. DUV lithography is a planar technology and is of widespread use in modern microelectronics fabrication. Hence, our approach warrants the possibility for high throughput and thus low-cost fabrication of silicon waveguide Bragg gratings.

All fabricated waveguides exhibit an overall height of $t = 1.5$ µm, an etching depth of $h = 0.5$ µm and widths *w* varying between 1.0 and 2.2 µm. The gratings have a period of 226 nm to provide a reflection around $\lambda = 1550$ nm, an overall length of $L = 800$ µm and duty cycle of $D = 0.3$.

Fig. 3 shows an example of the fabricated gratings.

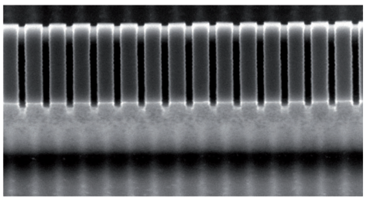

Fig. 3. SEM micrograph with a tilted top view of the fabricated Bragg reflector with an etching depth of 80 nm on a 1.6 µm wide rib waveguide.

4. *CHARACTERIZATION*

The fabricated samples were experimentally characterized measuring their reflection and transmission spectra. The measurement setup used for the characterization consists on a transmission measurement setup, where the single pass transmission through the silicon waveguide is measured. The analysis of the spectral behavior of the gratings was performed with a tunable laser source while a polarization controller allowed setting the polarization of the propagating light. An efficient in- and out-coupling was achieved using lensed fibers, and facets were covered with an antireflection coating to avoid undesired resonances. The grating transmissivity was calculated as the ratio between the power transmitted by a waveguide with grating, and the one measured from a common waveguide, isolating the grating performance from the waveguide characteristics [6].

In Fig. 4 the measured spectra for Bragg reflectors patterned with EB lithography are shown. It can be observed that a low loss is introduced, in the order of 0.5 dB. At the Bragg wavelength a reflectivity of 80% is achieved over a narrow bandwidth of 0.8 nm for the TE polarization, corresponding to an extinction ratio of 15 dB in the transmission.

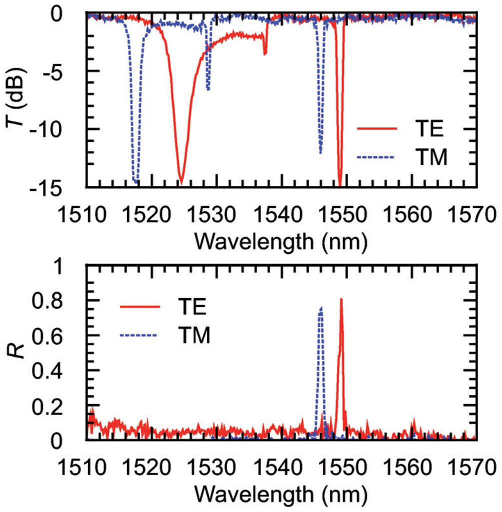

Fig. 4. Transmission and reflection spectra for Bragg reflectors fabricated on a 1.6 _m wide rib waveguide. The grating depth is 80 nm, the period 226 nm and the overall length 800 _m.

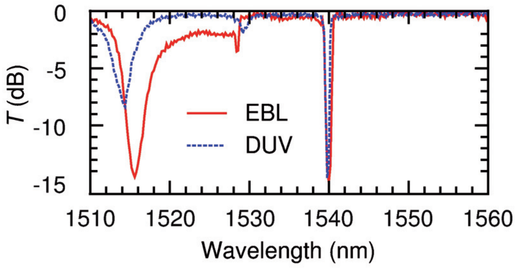

Fig. 5. Transmission spectra of two Bragg gratings on SOI rib waveguides patterned with DUV and EB lithography respectively. Both devices exhibit an overall length of 800 µm. TE polarization was considered.

At shorter wavelengths, around 1525 nm, a broad drop in the transmission spectrum is present, corresponding to a coupling to backward higher order modes, as already observed in the simulations (see Fig. 2). Since they cannot be guided in a single-mode rib waveguide, they are not back reflected and leak out. This is confirmed by the absence of any reflected signal at these wavelengths.

The reflected wavelength for the TM mode is shifted by 3 nm towards shorter wavelengths in respect to the TE reflection peak, indicating a waveguide birefringence of 7 x 10^{-3}. Furthermore a lower reflectivity and extinction ratio are observed. This would suggest that the interaction between the TM optical field and the grating etched on the top of the waveguide rib is relatively weak compared to the TE polarization.

Fig. 5 shows the measured transmission curves (TE polarization) for two gratings patterned with the presented DUV technology and with EB lithography respectively. One can easily observe that the two curves are in good agreement with each other, exhibiting a strong dip around $\lambda = 1550$ nm over a bandwidth of 0.7 nm. At other wavelengths the loss introduced from the gratings is around 0.3 dB.

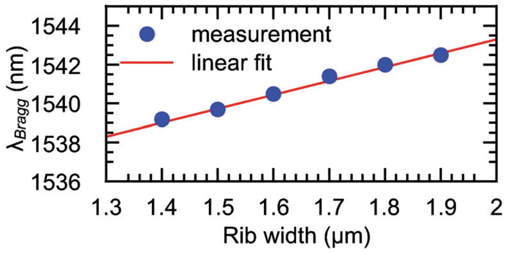

Fig. 6. Dependence between the peak reflected wavelength and the width of the waveguide.

On Fig. 6 the influence of the waveguide geometry is considered. The measured Bragg wavelength for the TE polarization is depicted as function of the rib width. It can be observed that equal Bragg reflectors fabricated on smaller waveguides exhibit reflection at shorter wavelengths because of the lower effective refractive index.

5. CHIRPED GRATINGS

Bragg gratings can be employed for the compensation of the chromatic dispersion introducing a proper chirp. The position of the reflected wavelengths is varied along the device, introducing the desired delay [10]. This is normally achieved varying the grating period; however the linear dependence of the reflected wavelength on the rib width previously shown on Fig. 6 suggested another way to produce the chirp: it is possible to keep the period constant and taper the waveguide width (see Fig. 7). It was observed that the period variation has an effect on the position of the reflected wavelength three orders of magnitude larger than a variation of the waveguide width [11]. Hence to achieve a chirped grating with a bandwidth of 1 nm a period variation of $\Delta\lambda = 0.15$ nm or a width variation of $\Delta w = 150$ nm are required.

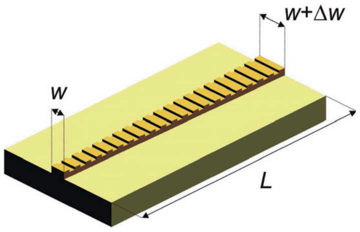

Fig. 7. Uniform Bragg grating on a tapered rib waveguide to achieve a chirp.

The compensation of a dispersion of some hundreds of ps/nm requires grating lengths in silicon of some millimeters. Hence a fabrication process based on DUV lithography was chosen for the device realization because of the absence of the limitation given by the stitching errors.

In Fig. 8 the measured spectra of different tapered gratings with variation of the end width is shown. It can be observed that increasing the end width of the taper a broadening of the grating

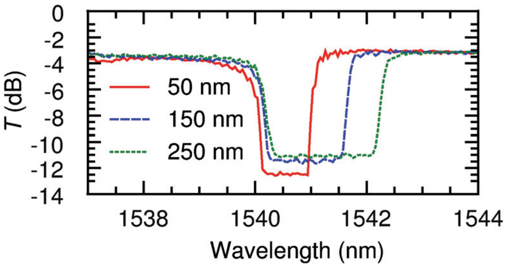

Fig. 8. Transmission curves of different chirped gratings with variation of the taper width _*w*. The grating period is 225 nm and the overall length *L* = 1 cm. TE polarization is considered.

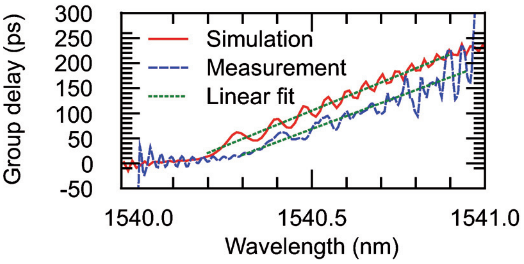

Fig. 9. Group delay of a grating with Δ*w* =150 nm. The grating length is *L* =1 cm.

bandwidth occurs. In particular, the short wavelength limit remains constant, since it is defined by the start waveguide width (1.5 µm in all cases), while the end wavelength varies linearly increasing the taper width. This effect would prove the presence of a chirp. Tuning the taper width is hence possible to precisely tune the grating bandwidth; the target bandwidth of 1 nm is achieved with a width variation Δ*w* around 100 nm. All gratings introduce a loss around 3 dB, which can be attributed to a scattering effects due to the surface modulation over the grating length of 1 cm.

The introduced group delay was measured as well, using a modulation phase shift method. In Fig. 9 the obtained results are presented and compared to a numerical simulation. A dispersion of 250 ps/nm over a bandwidth of 1 nm was observed, in good agreement with the theoretical predictions. A visible ripple is present on the curve, mostly due to the absence of a grating apodization.

6. CONCLUSION

We reported the realization and characterization of Bragg reflectors on silicon-on-insulator rib waveguides. We optimized the design of the device to achieve a high reflectivity on a narrow bandwidth and low insertion losses. The fabrication was performed with a simple two level lithographic process, which allows to easily integrate the Bragg gratings with other devices and can be CMOS compatible.

The measured transmission and reflection spectra of the obtained Bragg reflectors showed that a selective reflection larger than 80% on a bandwidth of 0.8 nm can be achieved, while for other wavelengths the device is transparent, introducing a loss of only 0.5 dB. The narrow bandwidth combined with the possibility to tune the reflection wavelength with the waveguide geometry, makes the device interesting for WDM applications.

Furthermore the integration of chirped gratings on SOI rib waveguide via tapering the waveguide width was presented. The concept permits to compensate the chromatic dispersion over narrow bandwidths keeping the requirements for the fabrication tolerances acceptable.

Measurements showed that a dispersion of 250 ps/nm over a bandwidth of 1 nm can be compensated with a 1 cm long grating.

REFERENCES

[1] M. P. Bulk, et al., “Optical Filters Utilizing Ion Implanted Bragg Gratings in SOI Waveguides”, *Adv. Opt. Technol.*, 276165, 2008.

[2] J. T. Hastings, M. H. Lim, J. G. Goodberlet, H. I. Smith, “Optical waveguides with apodized sidewall gratings via spatial-phase-locked electron-beam lithography”, *J. Vac. Sci. Technol. B*, vol. 20, pp. 2753–2757, 2002.

[3] D. Wiesmann, C. David, R. Germann, D. Emi, G. L. Bona, “Apodized Surface-Corrugated Gratings With Varying Duty Cycles”, *IEEE Photon. Technol. Lett.*, vol. 12, pp. 639–641, 2000.

[4] T. E. Murphy, J. T. Hastings, H. I. Smith, “Fabrication and characterization of narrowband Bragg reflection filters in silicon-on-insulator ridge waveguides”, *J. Lightwave Technol.*, vol. 19, pp. 1938–1942, 2001.

[5] S. Honda, Z. Wu, J. Matsui, K. Utaka, T. Edura, M. Tokuda, K. Tsutsui, Y. Wada, “Largely-tunable wideband Bragg gratings fabricated on SOI rib waveguides employed by deep-RIE”, *Electron. Lett.*, vol. 43, pp. 630–631, 2007.

[6] I. Giuntoni, A. Gajda, M. Krause, R. Steingrüber, J. Bruns, K. Petermann, “Tunable Bragg reflectors on silicon-on-insulator rib waveguides”, *Opt. Express*, vol. 17, pp. 18518–18524, 2009.

[7] J. Čtyroký et al., “Bragg waveguide grating as a 1D photonic band gap structure: COST 268 modelling task”, *Opt. Quantum Electron.*, vol. 34, pp. 455-470, 2002.

[8] I. Giuntoni, M. Krause, H. Renner, J. Bruns, A. Gajda, E. Brinkmeyer, K. Petermann, “Numerical Survey on Bragg Reflectors in Silicon-on-Insulator Waveguides”, *IEEE/LEOS Group IV Photonics Conf.* (GFP2008), Sorrento, Italy, September 2008, pp. 285–287.

[9] I. Giuntoni et al., “Deep-UV Technology for the Fabrication of Bragg Gratings on SOI Rib Waveguides”, *IEEE Phot. Technol. Lett.*, vol. 21, pp. 1894 1896, 2009.

[10] F. Ouellette, “Dispersion cancellation using linearly chirped Bragg grating filters in optical waveguides”, *Opt. Lett.*, vol. 12, pp. 847849, 1987.

[11] I. Giuntoni et al., “Chirped Gratings on Tapered SOI Rib Waveguides For Dispersion Compensation”, *Advanced Photonics and Renewable Energy OSA Optics & Photonics Congresses*, Karlsruhe, Germany, June 2010, BMB4.